

AFGEHANDELD

Prepared for:

Dutch Ministry of Transport, Public Works and  
Water Management, Tidal Waters Division

## The importance of internal waves for mixing in a stratified estuarine tidal flow

Part one: text and appendix

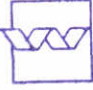

November 1993

**delft hydraulics**

Z 0694-1

R000 2251

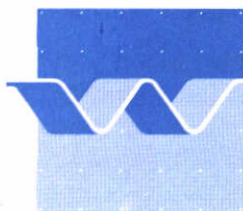


	bibliotheek postbus 177-2600 MH Delft waterloopkundig laboratorium/WL
<b>BB</b>	63680
<b>WL</b>	Z 0 694
<b>EXPL</b>	 40002252

## The importance of internal waves for mixing in a stratified estuarine tidal flow

Part one: text and appendix

R.E. Uittenbogaard  
J. Imberger



**delft hydraulics**

$L_E$  (3.81)  
 $L_c$  (3.107)

# Contents

## List of Symbols

<b>Summary and conclusions</b> . . . . .	<b>S — 1</b>
<b>1 General introduction and problem definition</b> . . . . .	<b>1 — 1</b>
1.1 General introduction . . . . .	1 — 1
1.2 Stratification and internal gravity waves . . . . .	1 — 3
1.3 Solutions of the ensemble-averaged momentum and mass transport equations . . . . .	1 — 4
1.4 Coarse numerical solutions of the momentum and mass transport equations . . . . .	1 — 4
1.5 Waves are not turbulence . . . . .	1 — 5
1.6 Turbulence modelling . . . . .	1 — 7
1.7 Restrictions and compromises for feasible computations . . . . .	1 — 8
<b>2 Some properties of turbulence, of hydrodynamic     instabilities and of internal waves</b> . . . . .	<b>2 — 1</b>
2.1 Introduction . . . . .	2 — 1
2.2 Some properties of turbulence . . . . .	2 — 2
2.3 The problem of turbulence in stably stratified flows . . . . .	2 — 7
2.4 Nonturbulent fluctuations in stably stratified flows . . . . .	2 — 8
2.5 Description of nonturbulent fluctuations in stably stratified flows as slowly varying internal waves . . . . .	2 — 16
2.6 Instabilities of internal waves . . . . .	2 — 23
2.7 Waves with large amplitude and wave-wave interactions . . . . .	2 — 28
2.8 Review of observations of internal waves . . . . .	2 — 38



<b>3</b>	<b>Some turbulence and internal wave estimators related to observations</b>	<b>3 — 1</b>
3.1	Introduction	3 — 1
3.2	IWE estimators	3 — 2
3.3	Upper limits for spectra of dense internal wave fields	3 — 5
3.4	Bandwidth of inertia-dominated turbulent motions	3 — 9
3.5	Some existing dimensionless numbers	3 — 13
3.6	Rate of energy dissipation and eddy diffusivity	3 — 14
3.7	A new dimensionless number: wave-detectability parameter	3 — 15
3.8	Energy flux of internal waves breaking in a shear flow	3 — 17
<b>4</b>	<b>Analysis of the observations</b>	<b>4 — 1</b>
4.1	Reference time, data, sites and measurement procedures	4 — 1
4.2	Microstructure density profiles combined with vertical finescale stability numbers	4 — 2
4.3	Centred displacement scale, Ellison scale and macrostructure observations	4 — 3
4.4	Dimensionless numbers	4 — 8
4.5	Energy dissipation rate and eddy diffusivity derived from microstructure	4 — 9
4.6	Indications of the performance of the $q^2$ - $\epsilon$ turbulence model	4 — 10
4.7	Discussion on two model coefficients in the $q^2$ - $\epsilon$ turbulence model	4 — 13
4.8	Transfer of wave energy to turbulence by wave breaking	4 — 16
4.9	Echosoundings	4 — 17
4.10	Inspection of time series of mesostructure observations	4 — 18
4.11	Analysis of short groups of internal waves	4 — 19
4.12	Spectra derived from time series observations	4 — 20

## References

## Appendix A Some details concerning limits of energy spectra



## List of symbols

$\langle \dots \rangle$	ensemble averaged variable
$\dots'$	fluctuations with zero mean
$\dots_w$	wave-induced fluctuations with zero mean
$\dots_t$	turbulence-induced fluctuations with zero mean
$\dots^{cc}$	complex conjugate
$\dots^+$	complex conjugate
$\dots_+$	upper limit taken
$\text{Im}(\dots)$	imaginary value taken
$\text{Re}(\dots)$	real value taken
$ \dots $	real-valued magnitude taken
$\dots_h$	horizontal vector component taken
$\dots_m$	complex-valued magnitude
$\vec{\nabla}$	$\mathbf{e}_i \partial / \partial x_i$ ; gradient operator
$\arg(\dots)$	phase taken
$A$	wave action
$b_z$	ratio between largest and smallest vertical wavelength
$B$	buoyancy flux
$B_\epsilon$	buoyancy flux term in $\epsilon$ equation
$Br$	energy released by wave breaking during shear time $\gamma_{\text{shear}}$
$c$	complex-valued phase velocity or constant in vertical wavenumber spectrum of wave-induced vertical displacements.
$c_r$	real part of phase velocity $c$
$c_i$	imaginary part of phase velocity $c$
$c_\mu$	parameter in $q^2-\epsilon$ turbulence model
$c_{1\epsilon}$	parameter in $q^2-\epsilon$ turbulence model
$c_{2\epsilon}$	parameter in $q^2-\epsilon$ turbulence model
$c_{3\epsilon}$	parameter in $q^2-\epsilon$ turbulence model
$c_{gz}$	vertical group velocity of internal wave energy
$C_{xy}$	coincidence spectrum of variables "x" and "y"
$C_{\partial p \partial u}^{(f)}$	temporal coherence spectrum for streamwise Stokes drift induced by waves in shear flow
$D$	diffusion of the kinetic energy stored in fluctuating motions or water depth
$D_{ij}$	components of the mean rate-of-deformation-tensor
$\underline{d}$	fluctuating rate-of-deformation-tensor with zero mean
$\underline{D}$	mean rate-of-deformation-tensor
$\mathbf{e}_i$	unit vector in direction "i" of Cartesian coordinate axis
$E$	1D spectral energy density or energy in a monochromatic wave
$E^{br}$	average of energy released per incident of wave breaking
$E_t$	magnitude of absolute quadrature vector
$E_u$	1D spectral energy density of kinetic energy
$E_z$	1D spectral energy density of vertical displacement of fluid parcel
$F$	amplitude function of vertical velocity component

$Fr$	internal Froude number
$Fr_\gamma$	small-scale Froude number also called strain-rate Froude number
$Fr_T$	turbulence internal Froude number also called activity parameter
$F_z$	Fourier-Stieltjes coefficient or temporal Fourier coefficient
$g$	gravitational acceleration
$G_{xy}$	cross spectrum between variables "x" and "y"
$G_{\partial u \partial u}^{(f)}$	temporal power spectrum of streamwise velocity fluctuations induced by the mean shear rate
$H$	thickness of stratified layer
$i$	as subscript ( $i=1,2,3$ or $x,y,z$ ), else $i=(-1)^{1/2}$ .
$I_{xy}^{(f)}$	single temporal quadrature spectrum between variables "x" and "y"
$\underline{k}$	wavenumber (vector)
$k$	streamwise wavenumber component
$K$	wavenumber magnitude with sign of k-component
$\ell$	transverse wavenumber component
$L$	unspecified length scale
$L_C$	centred displacement scale
$L_E$	Ellison length scale
$L_K$	Kolmogorov length scale
$L_{mix}$	turbulence mixing length
$L_O$	Ozmidov length scale
$m$	vertical wavenumber component
$M$	lower limit of vertical wavenumber component
$N$	buoyancy frequency
$P$	turbulence production or pseudo-momentum
$P_\epsilon$	production of $\epsilon$ i.e. of small-scale enstrophy
$p$	fluid pressure
$q^2$	turbulent kinetic energy
$Q$	source/sink of scalar
$Q(z)$	function in Taylor-Goldstein equation
$Q_{xy}$	quadrature spectrum of variables "x" and "y"
$ Q _{xy}$	spatial absolute quadrature spectrum for variables "x" and "y"
$ Q _{xy}^{(f)}$	temporal absolute quadrature spectrum for variables "x" and "y"
$Re$	Reynolds number
$Re_T$	turbulence Reynolds number
$Rf$	flux Richardson number
$Ri$	gradient Richardson number
$St$	ratio between coherence spectrum based on $\rho$ and $u$ and the spectrum for the mean-shear-wave induced Stokes drift.
$\underline{R}$	Reynolds stress tensor
$\underline{T}$	force due to the averaged unbalance of fluctuating momentum fluxes
$T$	upper limit of integration time
$T_{i-t}^\gamma$	transfer of wave energy to turbulence by wave-induced strain rate
$T_{i-t}^{br}$	transfer of wave energy to turbulence by wave breaking
$U$	typical streamwise velocity



$\underline{u}$	velocity vector
$u$	streamwise velocity component
$v$	transverse velocity component
$w$	vertical velocity component
$\underline{X}$	Lagrangian displacement of a fluid parcel
$Z$	vertical displacement of a fluid parcel
$z$	vertical coordinate (opposite to gravity)
$z_c$	level of critical layer
$\alpha$	rms of relative slope fluctuations of density isolines
$\beta$	damping rate or growth rate
$\gamma$	function related to the temporal and the vertical changes of IWE or the rms of strain rate
$\gamma_{xy}^2$	coherence function between variables "x" and "y"
$\gamma_{\text{shear}}$	inverse of mean shear rate $(dU/dz)^{-1}$
$\Gamma_T$	eddy diffusivity
$\delta$	signature of the influence of the vertical curvature of mean streamwise velocity on the dispersion relation for a solitary linear internal wave or the temporal phase function for phase locking in wave-wave interaction theory
$\Delta X$	increment of any variable X
$\Delta_\theta$	ratio between time to form a critical layer versus shear time $\gamma_{\text{shear}}$
$\epsilon$	rate of dissipation of turbulent kinetic energy
$\epsilon_c$	rate of dissipation of $\epsilon$ i.e. of small-scale enstrophy
$\zeta$	complex-valued function in wave-wave interaction theory
$\eta^2$	enstrophy
$\theta$	angle between wavenumber vector and horizontal plane
$\kappa$	Von Kármán constant
$\lambda$	wavelength
$\mu$	combined temporal and spatial variability of IWE or measure of wave-induced density slope perturbations
$\mu_K$	proportionality factor between Kolmogorov length scale and smallest turbulence length scale
$\mu_O$	proportionality factor between Ozmidov length scales and the largest turbulence length scale
$\mu_0$	detuning parameter in wave-wave interaction theory
$\nu$	kinematic viscosity
$\nu_a$	artificial diffusivity added to diffusion terms in 1DV $q^2$ - $\epsilon$ turbulence model
$\nu_T$	eddy viscosity
$\Pi_Z$	3D energy density spectrum of vertical fluid parcel displacement
$\rho$	fluid density
$\rho_0$	constant reference fluid density
$\sigma_a^{bc}$	interaction coefficient for wave mode "a" interacting with modes "b" and "c"
$\sigma_{\text{eff}}$	Prandtl/Schmidt number corrected for internal wave straining
$\sigma_p$	turbulent Prandtl/Schmidt number for diffusion of quantities $p = \epsilon, \rho$ or $q^2$
$\sigma_T$	turbulent Prandtl/Schmidt number
$\tau_L$	Lagrangian integral time scale
$\phi$	scalar quantity or phase function
$\phi_{xy}$	phase function between variables "x" and "y"

---

$\chi$	conversion parameter between quad-spectra and internal wave energy
$\psi$	stream function
$\omega_i$	vorticity components ( $i=x,y,z$ )
$\underline{\omega}$	vorticity vector
$\omega$	angular frequency
$\Omega$	intrinsic angular frequency of a solitary wave or the sum of three intrinsic angular frequencies
$\Omega'$	measure of detuning: $\Omega$ by normalized $2\mu_0$ .
$\Omega_p$	intrinsic angular frequency of wave component $p=a,b,c$ .



## Summary and conclusions

The combination of vertical microstructure profiling while observing the horizontal fluctuations of velocity and density in a stratified tidal channel presents an excellent methodology to study internal waves and turbulence. Although our observations were restricted to two sites in the Rotterdam Waterway Estuary during one afternoon and one morning they provide an extensive data set to diagnose the stratified tidal flow at scales between 1 mm and 100 m.

In the stratified tidal flow of the Rotterdam Waterway we observed at gradient Richardson numbers ranging between 0.4 and 3.0 only signatures of three-dimensional turbulence below length scales of several centimetres. Despite the strong tidal flow with a velocity of about 500 mm/s the vertical eddy diffusivity was reduced to about 10 to 30 mm<sup>2</sup>/s instead of 1000 to 2000 mm<sup>2</sup>/s at levels of nearly unstratified flow. Nevertheless the energy dissipation and consequently the rate of destruction of mean momentum, the flow resistance, in the stratified layer was rather strong ( $\epsilon = 10^{-5}$  m<sup>2</sup>/s<sup>3</sup>) as if the flow was unstratified. Hence, the well-known large ratio between power consumption and conversion into mean potential energy by vertical mixing of mass in stably stratified flows was confirmed.

At lower dissipation and mixing rates, we derived similar results from our observations in the adjacent Caland channel at larger gradient Richardson numbers between 2 and 10 and at lower velocities of about 200 mm/s.

The relatively strong energy dissipation cannot be explained by turbulence production through the shear rate of the mean flow alone. In this respect the  $q^2$ - $\epsilon$  turbulence confirmed this notion as it underestimated the mixing length and rate of energy dissipation  $\epsilon$  by at least a factor of 100.

Instead, we conclude that the continuous generation of random internal gravity waves as well as breaking of these waves explain the relatively large power consumption and equivalently the flow resistance. The waves can be generated within the water body by the vertical differences in streamwise velocity along the water depth similar to turbulence generation. The velocity differences deform the internal waves into so-called critical layers and wave breaking occurs. This reduces the wave height by an amount which we can observe from finescale measurements and thus we can estimate the release of wave energy into turbulence.

To support this theory we designed and applied a series of detection criteria that all point to the existence of random internal gravity waves with streamwise wavelengths exceeding about 5 m. Indeed the breaking of these waves can account for the observed energy consumption of the flow. If we consider the typical deformation time  $\tau_{\text{shear}}$  of a fluid parcel as the inverse shear rate  $(dU/dz)^{-1}$  then marginal wave breaking at intervals of 20 to 70  $\tau_{\text{shear}}$  is sufficient to produce the observed level of turbulence.

Hence, we conclude that turbulence models with a transport equation for turbulent kinetic energy should be extended with the turbulence production by computationally unresolved internal waves.

Analysis of the observed wave-induced vertical displacement and cast into a typical vertical wavenumber spectrum shows that occasionally overturning may occur i.e. gravitational instability of the density profile. This supports the assumed turbulence production by internal wave breaking.

The observed fluctuations of the transverse and vertical velocity at streamwise wavelength exceeding about 30 m can be well explained as induced by linear random internal waves.

However, about 50% of the energy in the streamwise velocity fluctuations are not accounted for by our estimator for internal wave energy. The unaccounted part of the streamwise velocity fluctuations may be induced by assumed vertical steplike structures of the streamwise velocity but apart from similarly observed vertical density structures we could not verify this assertion.



# 1 General introduction and problem definition

## 1.1 General introduction

This report consists of two parts: part one for the text and references and part two contains the tables and the figures. This report contains the analysis of data obtained in a field campaign on random internal gravity waves and turbulence in the Rotterdam Waterway Estuary which is located in the Netherlands. This report is one of the last reports in the context of the fulfilment of the long term research plan on turbulence and on mixing in stratified flows (Uittenbogaard, 1986). Moreover, this long term research plan is embedded in the one on inhomogeneous flows (Abraham and Spanhoff, 1988), commissioned by the Tidal Waters Division of the Netherlands Ministry of Transport and Public Works and Water Management (in Dutch: Dienst Getijdewateren, Rijkswaterstaat). It aims at the improvement of the three dimensional description, based on knowledge of physical processes, of mass transport in shallow, free-surface flows with stable density stratification. The state-of-the-art of our point of view at the start of this research can be found in (Abraham, 1988).

In this report we analyze the results of two days of measurements made in the salt stratified Rotterdam Waterway Estuary. The main objectives of these measurements and this study were to assess the contribution of random internal gravity waves to vertical transport of mass and of momentum.

This field campaign was executed jointly with the Centre for Water Research at the University of Western Australia and in collaboration with several departments of the Netherlands Ministry of Transport and Public Works, in the following abbreviated as "the Ministry".

During preceding studies the support, guidance and patience of prof. Nieuwstadt of Delft University, The Netherlands, stimulated the first author in his research on internal waves and turbulence of which a part is presented in this report.

In this report we will apply knowledge of the following disciplines: (i) turbulence in stratified fluids (ii) internal gravity waves (iii) hydrodynamic instabilities (iv) instrumentation and methodology of field measurements in the field and (v) processing of random data. Therefore this report is more or less self-contained and thus it will inevitably repeat published information as shown by the rather extensive reference list. However, the purpose of this report, written for the Ministry, is to summarize existing as well as to transfer new knowledge, the latter mainly obtained in the aforementioned long term research plan.

In this campaign three groups of instruments covered the following three intervals of spatial and of temporal bandwidth in a tidal flow.

### *Microprofiles*

Vertical profiles of temperature and of salinity were obtained with the microstructure profiler at a resolution of approx. 1 mm. The probe descended at a speed of approx. 100 mm/s and its output, including pressure, was sampled at 100 Hz. At moderate or low vertical gradients of horizontal velocity the probe moves horizontally along with the fluid (Lagrangian) while passing through the vertical structure of that fluid volume. The total record per drop was divided into stationary records usually of the order of 100-1000 mm length along the vertical.



Hence, CWR's microstructure profiler measures fluctuations at the smallest observable scales which can be related to small-scale turbulence and it covers the complete spatial range where temperature fluctuations dissipate.

The first analysis of data obtained with this instrument has been reported in (Malatt, 1992). In the following we will call these measurements "vertical microstructure recordings" and usually omit the adjective "vertical". To shorten the terminology for this report only, we will define the microstructure as the small-scale fluctuations observed by CWR's profiler.

### *Finescale timeseries*

In addition, the report (Uittenbogaard, 1993) describes the first indicative analysis of measurements recorded with instruments and with data-acquisition hardware of DELFT HYDRAULICS and of the Directorate Noord-Holland. These instruments, measuring the three velocity components, salinity and temperature, were installed on a submersible platform of the Directorate Noord-Holland. This platform was suspended from the crane of the anchored vessel "Pavo". This vessel is one of the Ministry's survey vessels of the Directorate Zuid-Holland. Apart from three accelerometers also the heave, pitch and roll of the platform itself were recorded. The velocity and density recordings were corrected for spurious platform motions using transfer functions so that these corrected flow signals are linearly independent of the platform motions, the correction procedure assumes no interaction between the fluid motion and the motion of the platform.

Within the two days 13 sets of measurements were made with the platform consisting of 12 channels of information. The acquisition rate was 20 Hz during 30 min. With this set-up the smallest observable wavelengths were approx. 100 mm. Typical horizontal wavelengths between 0.1 and 100 m were recorded with typical frequencies of around 0.05 Hz. Compared with the previously described CWR's vertical microstructure recordings we will describe the platform measurements as "horizontal finescale time series recordings" and we will usually omit the adjective "horizontal". To shorten the terminology for this report only, we will define the finescale time series as the horizontally rather than vertically observed finescales using the instruments on the platform.

### *Vertical finescale*

Similarly, the report (Uittenbogaard, 1993) describes the preliminary analysis and testing of data collected with the Elmar which is a standard instrument of the "Pavo". The Elmar measures the horizontal velocity magnitude, its direction, the water temperature and the conductivity. For a particular depth the Elmar output was averaged over 1 min and recordings were obtained at 1 m and occasionally 0.5 m intervals. At these intervals vertical profiles of the horizontal velocity vector and of the density near the anchored vessel "Pavo" were obtained with a vertical spatial resolution of 2 m and temporal resolution of 30 min. We define recordings with the Elmar as "vertical finescale recordings". To shorten the terminology for this report only, we will define the vertical finescale as the observed density and horizontal velocity vector as recorded by the Elmar at vertical intervals coarse compared with the microstructure observations.



### *Essential points of view taken in this study*

The spatial and temporal resolution of the Elmar's recordings are of the order of feasible hydrodynamic computations; in this report we replace such computations with the Elmar recordings in order to extract model predictions of dissipation.

However, a point of concern may be the neglect of the contribution of advection to the state of turbulence at the sites.

A tedious alternative would have been to extend the measurements by simultaneous measurements of appropriate boundary conditions far upstream and far downstream from the sites. These boundary conditions would facilitate simulations of the stratified tidal flow using, for instance, the three-dimensional code TRISULA of DELFT HYDRAULICS with turbulence models (Uittenbogaard et al., 1992).

However, the scale of the finescale motions was such that three-dimensional measurement programme would have had to be very extensive. Since the aim was to show the existence of internal waves it was felt this would be done with single station profiling.

### *Contents*

This report was compiled at the end of a long term research programme aimed at mixing in stratified flows and hopefully it will also be read by those not familiar with this research. Therefore, the rather lengthy Chapter 1 presents our point of view taken in the research. In addition, it will provide an introduction to the different ways of interpreting the data and to simulate the flow either as ensemble averaged flow or as a so called large eddy simulation.

Chapter 2 presents an introduction to the motivation of this field campaign: the ambiguity between turbulence and random internal gravity waves in stratified flows and the physical mechanisms that contribute to transport of matter and of momentum.

Chapter 3 provides references and some background on observable microstructure parameters, scaling ideas and on estimators of turbulence and random internal gravity waves. Chapter 4 summarizes the results using the theory and the estimators and assesses the importance of random internal waves to the state of 3D-turbulence and of vertical mixing.

Appendix A provides some information on the analysis of Gibson to estimate saturation of internal wave spectra and the transition wavelength between turbulence and internal waves.

The other, accompanying part of this report contains the tables and figures of the microstructure and finescale observations.

## **1.2 Stratification and internal gravity waves**

If the density of the fluid increases in the direction of gravitational acceleration the fluid is said to be statically stable. Whether the flow of such a fluid is dynamically stable is another question.

Many examples exist where a stable stratification prevails; the nocturnal boundary layer, thermal stratification in lakes and the ocean, salinity stratification in estuaries and discharge of heated water.



In industrial flows, temperature differences are induced by heat transfer from or to solid walls, for instance in cooling circuits of power plants and in chemical reactors.

If a fluid parcel in a stably stratified environment is displaced vertically so that its potential energy differs from the surrounding fluid then it will fall back exchanging potential for kinetic energy. The transfer process is facilitated through pressure fluctuations. Such motions are called internal gravity waves or just "internal waves".

To argue that the net effect of internal waves on the flow require modelling we must first introduce the current strategies of solving large scale flows.

### **1.3 Solutions of the ensemble-averaged momentum and mass transport equations**

The basic momentum and mass transport equations are ensemble averaged. Here ensemble averaging can be imagined as averaging, of fixed points and at fixed reference times, over many repetitions of mutually independent flow realisations. Each realisation is accomplished by mutually independent replications of the experiment. The resulting partial differential equations for the ensemble-averaged flow variables are called Reynolds-averaged equations. The Reynolds-averaged equations contain unknown second-order correlations of fluxes related to fluctuations of momentum and/or mass. The equations now describe the spatial and temporal evolution of the ensemble-averaged velocity and mass concentration. The solution of these Reynolds-averaged partial differential equations provides an estimate of the ensemble average of the flow field in time as well as in space. Additional estimation of, for instance, the variances of the fluctuations of velocity and concentration provide information on the probability with which the actual flow deviates from the predicted ensemble.

### **1.4 Coarse numerical solutions of the momentum and mass transport equations**

In order to numerically solve the ensemble equations the flow variables are defined at discrete spatial points at discrete time intervals. The arrangement of spatial points is called a mesh and the distances between adjacent mesh points are called mesh sizes. Given this mesh and the set of flow variables for each mesh point at discrete time levels, the original partial differential equations for momentum and mass may be properly discretized. The resulting set of equations for the discretized flow variables are called finite difference equations.

Consistency with the original set of equations requires that for vanishing mesh size and vanishing time intervals the finite difference equations yield the solution to the original partial differential equations. Numerical finite difference or numerical finite element models are employed for large scale natural flows in seas, estuaries etc.; they are limited by their spatial and temporal resolution. Actually, in most cases in civil engineering the horizontal dimensions of the flow domain largely exceed the vertical scales such as the waterdepth. Moreover, in three-dimensional numerical computations of these so-called shallow-water flows the vertical mesh size  $\Delta z$  is a fraction of the waterdepth whereas the horizontal mesh size  $\Delta x$  may be much larger than the waterdepth. This large anisotropy in mesh size, in combination with the numerical solution technique, implies a dominant low-pass spatial filter along horizontal planes.



This filter reduces the original continuum fluctuations with horizontal length scales smaller than about ten times  $\Delta x$ . The suppressed motions are defined as "subgrid fluctuations". The horizontal low-pass filter averages subgrid fluctuations along horizontal cross sections of the fluid domain. Consequently, in the low-pass filtered nonlinear differential equations for momentum and mass there appear second order correlations which are fluxes of 3D-subgrid momentum and of mass respectively. These fluxes form new unknowns and require additional equations to close the problem. We define the computation of the coarsely discretized momentum and mass transport equations as Large Eddy Simulation (LES).

Models for correlations of the suppressed fluctuations are called subgrid models. For large ratios of  $(\Delta x/H)$  the low-pass filter averages over  $O((\Delta x/H)^2)$  mutual independent samples of 3D-subgrid fluctuations. Thus the low-pass filter approximates the ensemble average of 3D-subgrid fluctuations with an error of  $O(H/\Delta x)$ . There is a formal difference between spatially low-pass filtered and ensemble-averaged fluxes because the former includes also mean variations related to the subgrid geometry of the fluid boundaries. However, this differences vanishes if in models for the ensemble-averaged fluxes the net effect of the small scale boundary variations are represented by an appropriately defined "roughness length". Actually, the roughness length in ensemble-averaged models formally follows from the application of a spatial low-pass filter on the ensemble-averaged fluxes.

Similarly, the solution of the ensemble-averaged partial differential equations can be approximated on a mesh and at discrete time levels using finite difference methods. Consequently, low-pass filtering of the ensemble-averaged nonlinear partial differential equations occurs. In addition, this low-pass filtering of the ensemble-averaged equations will introduce unresolved fluxes related to nonlinear subgrid variations of ensemble-averaged flow variables. Thus, apart from the resolved ensemble averaged fluxes, new additional fluxes appear. However, the general point of view is that the temporal and spatial variations of the ensemble-averaged flow field are so slow that with a fair choice of mesh size and time step and suitable roughness length the low-pass filter would not produce significant additional fluxes or truncation errors. Hence, in this context the subgrid fluxes of 3D-fluctuations approximate the ensemble-averaged fluxes related to 3D-fluctuations.

Thus, in terms of fluxes of momentum, of mass and of heat, the net effect of the unresolved products of fluctuations with respect to the low-pass filtered or to the ensemble-averaged flow variables require additional modelling. As argued above, we consider numerical modelling of shallow flows with horizontal mesh sizes that usually exceed the waterdepth. Then the low-pass filtered products of 3D-subgrid fluctuations can be modelled as if they were the ensemble-averages of similar products.

Presently, such modelling concerns only the so-called turbulent motions and Abraham (1988) reviewed the turbulence models feasible for stratified flows in civil engineering practice. However, in view of the subject of this report a clear distinction between turbulence and internal waves is essential.

## 1.5 Waves are not turbulence

A definition of turbulence may be given by a description of its basic mechanism which is "mixing". This mixing is caused by random motions with a large range of scales and which possess vorticity.



Turbulence causes mixing by its action of stretching mass and momentum gradients so intensifying the molecular transport. Turbulence also causes dispersion by its ability to rapidly distribute momentum and mass over space.

In turbulence the random rotations of fluid volumes may be idealized by spatially localised "eddies".

Fluctuations which are induced by only waves of infinitesimal amplitudes, for instance surface or internal waves, do not possess the same dispersion and mixing properties. The motion tends to organise fluid parcels in orbital motions that are capable of transporting kinetic energy and momentum. Further, since waves have discrete large length scales their energy dissipation is small in strong contrast with turbulence.

Thus, waves are not considered to be turbulence because the kinetic energy of the fluctuations is exchanged by potential energy related to the fluctuations and vice versa. In absence of turbulence and of molecular diffusion the process of particle displacement by waves is reversible: the original particle arrangement, before the waves perturbed it, can be recovered. This is an essential difference with turbulence where mixing implies irreversibility: only with a negligible probability the same particle arrangement can be restored.

The sum of many temporally and spatially regular waves may create random wave patterns, however, if summation is applicable, no mixing of mass occurs. The net effect of waves is a so-called drift (velocity) of the fluid and thus a transport of momentum and of scalar quantities.

Especially, the distinction between modelling subgrid waves of which their induced motions do not directly induce mixing of mass and modelling turbulence, which always mixes is the subject of this report. Further, waves always transport momentum and kinetic energy but not mass.

However, matters become more complicated if nonlinearities such as mutual interactions between waves or between turbulence and waves are considered. For instance, waves may excite turbulence and thus create mixing by a transfer of the energy, related to the wave-induced motions, to turbulence. In addition, the summation of series of regular waves, the validity of summation was assumed above, is a simplification. A regular wave may interact with waves at different wavelengths in a nonlinear fashion. Occasionally these so-called wave-wave interactions may create steep gradients and also create hydrodynamic instabilities such as wave breaking and consequently create turbulence and thus mixing.

Thus the point of view argued here reads: in stably stratified flows both turbulence as well as internal gravity waves contribute directly or indirectly to the fluxes of momentum and to the fluxes and variances of mass and heat. Consequently, if subgrid or ensemble-averaged internal waves with their energy content, their instabilities, their balance in wave forces and their wave-induced drift are not considered various sources of turbulence of mixing and of transport are neglected.

Because turbulence extracts energy from the mean flow which is characteristically different to how internal waves interact with the mean flow turbulence models inadequately represent the physics of internal waves. In order to improve the numerical prediction of stably stratified flows we propose here to model the net effect of internal gravity waves, either as low-pass filter subgrid fluxes or as ensemble-averaged fluxes, on the transport of mass and momentum separated from, but interacting with, turbulence. In the following part of this chapter we will not make a distinction between low-pass filtering and ensemble-averaging any more.



## 1.6 Turbulence modelling

In homogeneous fluids the state of turbulence depends on the spatial and temporal variations of the large scale flow.

Statistically, turbulent motions may be described by the joint probability distribution of their variables.

However, frequently the state of turbulence is approximated in models by a limited set of second and third order moments which we will call here "state parameters of second or third order". For instance, the state parameters of second order may involve the variance of velocity components or of scalar quantities, the cross correlation between velocity components or between velocity components and a scalar quantity or between pressure and velocity components, the variance of vorticity etc.. In addition, some of the triple correlations, based on combinations of velocity components, scalar quantities and pressure, are considered as well.

Those turbulence models which are based on the transport of the second order moments as turbulence state parameters, potentially have the required adaptability to compute turbulence fluxes subjected to the spatial and temporal variations of the ensemble-averaged flow. The preceding statement is mainly based on experiences with the computation of industrial flows which are confined in vessels, pipes etc.. Unfortunately, due to the large extend of the flow domain and due to the instrumentation and recording problems, a similar experience is not yet obtained, and will be much more difficult to obtain, in civil engineering applications. However, from the limited point of view of three-dimensional turbulence and its generation, many similarities between civil engineering and industrial flows exist.

The adaptability of turbulence to ensemble-averaged spatial and temporal variations is usually achieved with one or more so-called transport equations with sources and sinks for, and diffusion of the turbulence state parameter considered. These transport equations for turbulence parameters resemble the equations for mass transport. The simplest turbulence models use one transport equation, or sometimes only the analytical expression based on equilibrium of turbulence generation and dissipation.

Turbulence models based on one transport equation usually consider half of the sum of the variances of each of the velocity components as the transported turbulence state parameter. This sum equals the so-called turbulent kinetic energy  $\text{m}^2/\text{s}^2$  for which we write the symbol  $q^2$ . In literature, frequently  $k$  instead of  $q^2$  is used; we will reserve the symbol  $k$  for wavenumber magnitude. Actually, a more precise name for  $q^2$  is "turbulent kinetic energy density" meaning  $q$  equals the turbulent kinetic energy per unit mass. If a second transport equation is used this equation frequently concerns the transport of a state parameter that equals, or is directly related to, the rate of dissipation  $\epsilon \text{ m}^2/\text{s}^3$  of  $q^2$ . The dissipation  $\epsilon$  of  $q^2$  appears as a sink in the transport equation for  $q^2$  and among other terms this appearance creates a coupled set of equations. A prominent two-equation model is the  $k$ - $\epsilon$  or  $q^2$ - $\epsilon$  turbulence model (Launder and Spalding, 1974).

The combination of  $q^2$  and  $\epsilon$ , or instead of  $\epsilon$  another parameter replacing  $\epsilon$ , allows for the definition of flow dependent time and length scale of the turbulent motions. Moreover, these scales provide the turbulent analogue of molecular diffusion and molecular viscosity called eddy diffusivity and eddy viscosity respectively. Taylor (1914) and Prandtl (1925) assumed the eddy diffusivity and eddy viscosity were proportional to a length scale of the most energetic eddies and the rms value of the turbulent velocity fluctuations.



However, the eddy-diffusivity tensor can be derived more rigorously. The eddy viscosity and eddy diffusivity are added to their molecular counterparts in the respective momentum and transport equations for the computation of ensemble-averaged flows.

Finally, the most complicated turbulence models, called Reynolds Stress Models (RSM), see e.g. (Launder, 1984), consider the transport of the energy dissipation  $\epsilon$  and all relevant variances and cross correlations between velocity components and/or scalar quantities. However, RSM's applied to three-dimensional flows require at least seven mutually coupled transport equations (Launder et al., 1975).

Reynolds Stress Models use a transport equation for energy dissipation  $\epsilon$  and instead of one transport equation for kinetic energy  $q^2$  now six transport equations for each Reynolds stress components are added. This amounts to seven mutually coupled transport equations which avoid the introduction of the concept of eddy viscosity. In addition, the modelling of turbulent mixing of each scalar quantity requires four equations: three transport equations for the components of the turbulent flux vector and a fourth one for transport of the variance of scalar concentration. These four transport equations are necessary to avoid the concept of eddy diffusivity. For instance, in a flow where both temperature and salinity determine the fluid density through a state equation a total of 15 mutually coupled transport equations are required.

The RSM's do not require the assumption of an eddy viscosity and diffusivity and are conceptually more accurate than the one-equation or two-equation turbulence models; closure is corrodent at higher orders.

However, none of the shore models explicitly account for the presence of internal waves. In principal the action of internal waves could be included, but this would require a resolution matching the wavelength of the spectrum of internal waves present in the flow. At present such high resolution is not possible for geophysical or hydraulic prototype situations.

## 1.7 Restrictions and compromises for feasible computations

For the currently available computers, the computational effort and the requirements of computer memory are still severe for the three-dimensional calculation of flows. Especially in civil engineering practice with computations over many tidal cycles to obtain a quasi-steady state and with complex geometries such as estuaries with islands, dredged channels, harbours etc.. Fig. 1.1 shows the computational grid recently developed (Kernkamp and Van der Kaaij, 1993) to compute the tidal and stratified flows in the Rotterdam harbour area and in a part of the North Sea coast. For such computations the addition of a turbulence model with two or three transport equations is currently regarded as the maximum of a realisable extension from the point of view of computational effort involved.

Most of the free-surface flows in civil engineering are driven by large scale forces such as tidally induced surface elevations at open boundaries, forcing of the free surface by wind-shear stresses and horizontal density gradients. Experience shows that provided the depth-averaged energy dissipation is modelled well, the particular choice of the turbulence model hardly appears to influence the velocity field and surface elevations in non-stratified flows. Thus a simple turbulence model that produces the correct depth-averaged energy dissipation may be a good compromise between accuracy and computational effort (Davies and Gerritsen, 1994).



However, in stratified flows the vertical distribution of the vertical fluxes of mass and of momentum require more careful considerations. These vertical fluxes determine the vertical density and vertical profiles of the horizontal velocity vector at each vertical section and consequently the horizontal density gradients. These horizontal density gradients may drive the flow, for example tidal flows and flows with discharges of water with a density that differs from the density of the receiving water. Consequently, the detailed vertical distribution of forces induced by turbulence and by internal waves and mixing by turbulence should be predicted more accurately than in the non-stratified case.



Fig. 1.1 Example of a complex grid to compute the stratified flow in the Rotterdam harbour area and a part of the North Sea (Kernkamp and Van der Kaaij, 1993).

The model for transport of Internal Wave Energy (IWE-model) proposed by (Uittenbogaard and Baron, 1989) may in principle be added to any turbulence model based on transport equations for the mean turbulence properties, especially the  $q^2$ - $\epsilon$  turbulence model and the RSM. In comparison with the more elaborate RSM, the  $q^2$ - $\epsilon$  model is presently assessed to be a good compromise between the accuracy of turbulence description and the computational effort. For the purpose of practical applications it is better to limit the computation to one additional transport equation for the energy stored in internal gravity waves. In this way the computational effort remains acceptable.



## 2 Some properties of turbulence, of hydrodynamic instabilities and of internal waves

### 2.1 Introduction

In Chapter 1 we explained that this report is intended to be fairly well self-contained. Hence, we aimed at a compromise between only referring to the extensive literature or to compose a book on internal waves in conjunction with turbulence. In particular, in this chapter we briefly repeat well-known classical turbulence properties in a manner that demonstrates the differences and the similarities between turbulence and internal waves. In addition, we present new analytical properties of infinitesimal internal waves in a shear flow. Therefore, this chapter summarizes the conceptual basis with which we interpret the field observations in Chapter 4.

Another important point for the entire report is that we will exploit linear wave theory as much as possible. However, we will verify our assumptions against the observations in the field and use criteria on the importance of nonlinearity in terms of wave amplitude as well as wave-wave interactions.

As discussed in Chapter 1, we are concerned with ensemble-averaged fluxes and their spatial derivatives, of momentum and of mass induced by turbulent fluctuations and by internal waves. Hence, we would like to introduce a comprehensive overview of properties of turbulence and of initially nonturbulent fluctuations and their contribution to fluxes of mass and of momentum.

First, in Section 2.2 we introduce some of the well-known properties of turbulence, in particular those connecting momentum fluxes with mass fluxes. We have limited this overview to only the basic properties of turbulence that lead to the proposition that mixing of mass are closely connected to the transfer of momentum by turbulence. In this section no extensive references will be made to the currently applied turbulence models.

Second, in Section 2.3 we state the central problem of this report, namely that a stable stratification reduces the vertical mass fluxes in comparison with vertical fluxes of horizontal momentum. These findings appear to contradict the results of Section 2.2.

Third, in Section 2.4 we introduce and summarize the point of view taken in this report to account for these observations. Following Taylor (1931) we will introduce the notion of initially nonturbulent modes. The physical processes related to these modes provide a conceptual model to interpret the observations in stably stratified flows.

Similar to Section 2.2 we attempt to restrict the contents of Section 2.4 to only the essential aspects of the relevant hydrodynamic instabilities in stratified flows and to the relevant properties of internal waves with small amplitudes. In Section 2.4 we have made a compromise such as to present these properties from one second order differential equation, namely the Taylor-Goldstein equation, and not to aim at completeness nor to present the most general formulation of these properties.

## 2.2 Some properties of turbulence

In this section we will introduce the concepts of eddy viscosity and of eddy diffusivity as the turbulent counterparts to the molecular parameters. Some definitions and some properties are given which will help us to introduce the actions of turbulence leading to fluxes of momentum and mass by turbulence. This will yield a basis, provided in Section 2.3, for the problem dealt with in this report.

By considering an energy balance between production and viscous dissipation of turbulent kinetic energy Osborne Reynolds (1894) obtained a criterion for the growth of turbulent kinetic energy. Define the variable  $q$  by:

$$q^2 = \frac{1}{2} \langle \underline{u}' \cdot \underline{u}' \rangle. \quad (2.2.1)$$

Fluctuations, denoted by a prime  $(..)'$ , are variations around a mean value obtained by means of an appropriate averaging operator  $\langle .. \rangle$ . Reynolds concluded that the dimensionless number

$$Re = \frac{U.H}{\nu} \quad (2.2.2)$$

based on a representative mean fluid velocity magnitude  $U$  and length scale  $H$  has a critical value above which the fluctuations grow and the flow is said to be turbulent. Although the critical value of the so-called Reynolds number  $Re$  for the onset of turbulence is dependent on the situation, typical critical values are around  $10^3$ . In civil engineering practice  $Re$  may reach  $10^6$ . In many scaled laboratory experiments for civil engineering research  $Re$  ranges from  $10^4$  to  $10^5$ . Experiments in homogeneous fluids reveal that at large Reynolds number an equilibrium is reached where the turbulence is well developed with respect to mean flow.

Below we will introduce some basic relationships for the fluxes of momentum and of mass, the production and the viscous dissipation of turbulence and the concepts of eddy viscosity and of eddy diffusivity. In particular we will argue that the ratio between eddy viscosity and eddy diffusivity related to turbulence is close to and may be slightly less than unity. In Section 2.3 we will refer to measurements from which follows that this ratio increases drastically in stably stratified flows and in essence this forms the problem we would like to solve in this report.

We start with the introduction of stresses and forces as a result of averaging momentum fluctuations which are not necessarily induced by turbulence. Averaging of the convective terms  $(\underline{u} \cdot \vec{\nabla} \underline{u})$  of an incompressible fluid produces in the momentum equations an additional force  $\underline{T}$  per unit mass

$$\underline{T} = -\vec{\nabla} \cdot \langle \underline{u}' \underline{u}' \rangle \quad (2.2.3)$$

being the divergence of the so-called Reynolds stress tensor (divided by density)

$$\underline{R} = -\langle \underline{u}' \underline{u}' \rangle, \quad (2.2.4)$$



This tensor contains the momentum fluxes across imaginary control surfaces in the fluid. A theorem of the gradient operator allows us to express the divergence (2.2.3) as

$$\mathbf{T} = \bar{\nabla} \mathbf{q}^2 + \langle \mathbf{u}' * \boldsymbol{\omega}' \rangle, \quad (2.2.5)$$

where  $\boldsymbol{\omega}' = \bar{\nabla} * \mathbf{u}'$  is the vorticity of the motion. Lighthill (1962) calls the last term in (2.2.5) the vortex force. Consequently, the relevant deviatoric part of the stress tensor reads  $(-\langle \mathbf{u}' \mathbf{w}' \rangle)$  and the x-component of the vortex force yields:

$$T_x = \langle \mathbf{u}' * \boldsymbol{\omega}' \rangle_x = -\langle \mathbf{w}' \omega'_y \rangle = -\frac{\partial \langle \mathbf{u}' \mathbf{w}' \rangle}{\partial z}. \quad (2.2.6)$$

The importance of the lateral vorticity component  $\omega'_y$  in (2.2.6) has lead Reynolds, Taylor, Prandtl and many others researchers at the end of the past century and the beginning of this century to the concept of eddies. The eddies that contribute significantly to (2.2.6) are imaginary vortices of limited spatial extend with typical length scale  $L$ . A more precise definition of  $L$  will be given below.

With the introduction of the fluctuations the number of unknowns exceeds the number of equations. Hence, a so-called closure, in which essentially the unknown correlations are expressed in mean quantities, is required to obtain a closed set of equations. In this section we will assume that the fluctuations are induced by turbulence. In the context of the simple flow considered before, Taylor (1921, 1931) proposed to model the velocity fluctuations  $\mathbf{u}'$  as being the result of the transport of mean momentum  $\langle \mathbf{u} \rangle$  in  $z$ -direction along displacement  $Z'$  induced by turbulence:

$$\mathbf{u}' = -\sigma_T \left( Z' \cdot \frac{\partial \langle \mathbf{u} \rangle}{\partial z} \right), \quad (2.2.7)$$

with a proportionality factor  $\sigma_T$  to be determined later. Consequently, the covariance  $\langle \mathbf{u}' \mathbf{w}' \rangle$  appearing in (2.2.6) reads:

$$\langle \mathbf{u}' \mathbf{w}' \rangle = -\sigma_T \left\langle \frac{D \frac{1}{2} Z'^2}{Dt} \right\rangle \frac{\partial \langle \mathbf{u} \rangle}{\partial z} \approx -\sigma_T \frac{\overline{D \langle \frac{1}{2} Z'^2 \rangle}}{Dt} \frac{\partial \langle \mathbf{u} \rangle}{\partial z} = \text{def} = -\nu_T \frac{\partial \langle \mathbf{u} \rangle}{\partial z}. \quad (2.2.8)$$

This so-called eddy viscosity  $\nu_T$  is defined as

$$\nu_T = \sigma_T \frac{\overline{D \langle \frac{1}{2} Z'^2 \rangle}}{Dt}, \quad (2.2.9)$$

with mean material derivative  $\frac{\overline{D}}{Dt} = \frac{\partial}{\partial t} + \langle \mathbf{u} \rangle \cdot \bar{\nabla}$ .

In addition, Taylor (1921) derived for the variance of the fluctuating transverse displacement  $Z'$  by Lagrangian integration along paths  $\mathbf{X}(\tau)$ , with  $\mathbf{X}(0) = \mathbf{x}$ , of fluid particles:

$$\langle Z'^2 \rangle = 2T \int_0^T \left( 1 - \frac{\tau}{T} \right) \langle \mathbf{w}'(\mathbf{X}(\tau), t + \tau) \mathbf{w}'(\mathbf{X}(0), t) \rangle d\tau. \quad (2.2.10)$$

In (2.2.10) is  $\mathbf{w}'(\mathbf{X}(\tau), t + \tau)$  the Lagrangian velocity of a small fluid parcel which equals the Eulerian velocity  $\mathbf{w}'$  when this fluid parcel arrives at time  $(t + \tau)$  in position  $\mathbf{x} = \mathbf{X}(\tau)$ . For increasing travel times  $\tau$  the correlation in (2.2.10) vanishes for turbulent fluctuations and this introduces the definition of a Lagrangian correlation time  $\tau_L$

$$\langle \mathbf{w}'^2 \rangle \tau_L = \lim_{T \rightarrow \infty} \int_0^T \langle \mathbf{w}'(\mathbf{X}(\tau)) \mathbf{w}'(\mathbf{X}(0)) \rangle d\tau. \quad (2.2.11)$$

Hence, (2.2.10) is proportional to  $T$  for  $T \gg \tau_L$  and

$$\lim_{T \rightarrow \infty} v_T = \sigma_T \langle (w'(\mathbf{X}))^2 \rangle \tau_L \quad (2.2.12)$$

Actually, in (2.2.11) and in (2.2.12) it is assumed that the fluctuating velocity field is at least homogeneous during the time interval  $T$  where the correlation in (2.2.11) significantly contributes to the integral. The previous introduction and definition of eddy viscosity is one of many possible justifications.

The connection between (2.2.12) and Prandtl's concept of a mixing length  $L$ , imagined as the typical size of the most energetic eddies, is established by rewriting a part of (2.2.12) in terms of a path length or mixing length as

$$L = \tau_L |w'|, \quad (2.2.13)$$

where  $|w'| \equiv \langle w'^2 \rangle^{1/2}$ .

Thus the mixing length  $L$  is a typical distance created by those eddies which contribute significantly to the integral (2.2.10). These eddies remain coherent over a typical time interval  $\tau_L$ .

Similarly, the previous derivation may be applied to the transport of a constituent  $\phi$  such as salt or heat content, provided  $\phi$  exhibits only a mean gradient in  $z$ -direction. This restriction may be viewed as an approximation for large scale flows in civil engineering. Because of the advection term ( $\underline{u} \cdot \nabla \phi$ ) in the averaged transport equation with mean variables in the LHS, the following flux appears in the RHS:

$$Q = -\nabla \cdot \langle \underline{u}' \phi' \rangle. \quad (2.2.14)$$

For the simple flow considered, only the  $z$ -derivative is of importance and then

$$Q = -\frac{\partial \langle w' \phi' \rangle}{\partial z}. \quad (2.2.15)$$

The transport equation for the fluctuation  $\phi'$  reads:

$$\frac{D\phi'}{Dt} + w' \frac{\partial \langle \phi \rangle}{\partial z} = \kappa \nabla^2 \phi' - Q \quad (2.2.16)$$

and Lagrangian integration of (2.2.16) results into an expression similar to (2.2.7), however, without the yet unspecified correction  $\sigma_T$  due to the incompressibility requirement:

$$\phi' = -Z' \frac{\partial \langle \phi \rangle}{\partial z}. \quad (2.2.17)$$

The final derivation to obtain the covariance  $\langle w' \phi' \rangle$  appearing in (2.2.15) is now straightforward and reads:

$$\langle w' \phi' \rangle = -\Gamma_T \frac{\partial \langle \phi \rangle}{\partial z}. \quad (2.2.18)$$



This so-called eddy diffusivity  $\Gamma_T$  is defined by:

$$\Gamma_T \equiv \frac{\overline{D} \langle \frac{1}{2} Z'^2 \rangle}{Dt} \quad (2.2.19)$$

The increase in variance of  $Z'$  can be inferred from the measurement of for instance dye or smoke particles injected from a point source in the flow and thus the eddy diffusivity may be estimated from experimental observations. In this context Taylor (1921) refers to Richardson who made in 1920 long exposure photographs of smoke plumes from a chimney. The connection between eddy viscosity and eddy diffusivity reads:

$$\nu_T = \sigma_T \Gamma_T . \quad (2.2.20)$$

The ratio between kinematic viscosity and the coefficient of heat or molecular diffusion is called Prandtl number or Schmidt number respectively. In analogy with molecular diffusivity,  $\sigma_T$  in (2.2.20) is called the turbulent Prandtl/Schmidt number. In contrast with its molecular counterpart the distinction between the transported constituent vanishes provided the constituent is not a statistical property of turbulence.

Fortunately, in turbulent flows with constant density,  $\sigma_T$  varies little and usually  $0.5 < \sigma_T < 0.7$  (Rodi, 1984). The lower limit of  $\sigma_T$  is related to round, turbulent jets for which  $D\bar{u}'/Dt$  exhibits more the tendency to volume changes than in channel flows. In the early studies on turbulence and mixing  $\sigma_T = 1$  was assumed which is called the Reynolds analogy between the mixing of constituents and the mixing of momentum. A value of the turbulent Prandtl/Schmidt number that is smaller than unity expressed the notion that the motion of a particle or constituent dissolved in the fluid is not a fluid parcel (small fluid volume).

The work  $P$  per unit time and per unit mass done by the mean flow against the Reynolds stresses reads (Malvern, 1969):

$$P = \underline{\underline{R}} : \underline{\underline{D}} \equiv R_{ij} D_{ij} , \quad (2.2.21)$$

with  $\underline{\underline{D}} = \frac{1}{2} [\vec{\nabla} \langle \underline{u} \rangle + (\vec{\nabla} \langle \underline{u} \rangle)^T]$  .

In (2.2.21),  $\underline{\underline{D}}$  is the strain rate or the rate-of-deformation tensor of the mean flow (Malvern, 1969). The expression (2.2.21) is the production  $P$  of turbulent kinetic energy.

The mean work done by fluctuations per unit time and per unit mass against viscous stresses by fluctuations is defined as the rate of energy dissipation  $\epsilon$ . The expression for  $\epsilon$  in an incompressible flow is similar to (2.2.21) and it reads

$$\epsilon = 2\nu \langle \underline{\underline{d}} : \underline{\underline{d}} \rangle , \quad (2.2.22)$$

with  $\underline{\underline{d}} = \frac{1}{2} [\vec{\nabla} \underline{u}' + (\vec{\nabla} \underline{u}')^T]$  .

The double-contracted product  $\langle \underline{\underline{d}} : \underline{\underline{d}} \rangle$  appearing in (2.2.22) can be written as (Tennekes and Lumley, 1983, page 88):

$$\langle \underline{\underline{d}} : \underline{\underline{d}} \rangle = \eta^2 - \vec{\nabla} \cdot \underline{\underline{T}} , \quad (2.2.23)$$

$$\text{with } \eta^2 = \frac{1}{2} \langle \underline{w}' \cdot \underline{w}' \rangle \text{ and } \vec{\nabla} \cdot \underline{T} = \frac{\partial^2 \langle \underline{u}_i' \underline{u}_j' \rangle}{\partial x_i \partial x_j} .$$

In (2.2.23) is  $\eta^2$  The so-called enstrophy. Neglecting the gradients of covariances in (2.2.23) against the enstrophy for turbulent flows at high Reynolds numbers the rate of energy dissipation of turbulent fluctuations is now approximated by

$$\epsilon \approx 2\nu\eta^2 . \quad (2.2.24)$$

At length scales where viscous dissipation is significant the inertial and viscous forces should balance. Then from (2.2.29) follows the so-called Kolmogoroff length scale  $L_K$  for the dissipation of turbulent kinetic energy and  $L_K$  is defined as

$$L_K = \left( \frac{\nu^3}{\epsilon} \right)^{1/4} . \quad (2.2.25)$$

Finally, to close this section, the important transport equation for the kinetic energy  $q^2$  stored in fluctuations is presented. This so-called  $q^2$ -equation will form the cornerstone of our analysis and is one the starting points of turbulence modelling, see e.g. (Launder, 1984) and (Rodi, 1984). The  $q^2$ -equation is derived by ensemble averaging of the scalar multiplication with  $\underline{u}'$  of the momentum equation for  $\underline{u}'$  for an incompressible, density stratified flow including all mean velocity and density gradients. This procedure was first employed by Reynolds (1894) for unstratified fluids. Including stratification the result reads:

$$\frac{\overline{D}q^2}{Dt} = D + P - \epsilon - B , \quad (2.2.26)$$

$$\text{with } D = -\vec{\nabla} \cdot \left[ \frac{1}{2} \langle \underline{u}' (\underline{u}' \cdot \underline{u}') \rangle + \langle p' \underline{u}' \rangle \right] \text{ and } B = \frac{g \langle \rho' w' \rangle}{\langle \rho \rangle} .$$

Among other terms the  $q^2$ -equation contains the previously introduced production and dissipation terms  $P$  and  $\epsilon$  respectively. The derivation of (2.2.26) does not rely on the particular properties or assumptions of turbulence and equation (2.2.26) is equally valid for, for instance, random internal wave motions.

Ivey and Imberger (1991) have combined all the mechanical energy terms such that

$$P_{\text{net}} = -\frac{\overline{D}q^2}{Dt} + D + P ,$$

so that  $P_{\text{net}} = B + \epsilon$ . The increase in mean potential energy of a turbulent, stably stratified flow by mixing heavier fluid upwards equals the buoyancy-flux  $B$  in the  $q^2$ -equation. Hence, some of the energy flux  $P_{\text{net}}$  lost by the mean flow is recovered through flux  $B$ , however, for turbulence with an efficiency not exceeding 25 % (Ivey and Imberger, 1991).

The term  $D$  in (2.2.26) is called diffusion of  $q^2$  because of its a divergence of flux. Integration of  $D$  over the complete fluid domain with solid or nonturbulent boundaries shows that  $D$  cannot change the volume-averaged  $q^2$ . In  $D$  the flux vector  $\frac{1}{2} \langle \underline{u}' (\underline{u}' \cdot \underline{u}') \rangle$  implies mixing of instantaneous kinetic energy  $\frac{1}{2} \langle \underline{u}' \cdot \underline{u}' \rangle$  similar to mixing of momentum and of mass. For turbulent motions the second term  $\langle p' \underline{u}' \rangle$  is assumed to have a similar diffusive effect. However, for waves it can be shown that  $\langle p' \underline{u}' \rangle$  represents the flux of kinetic and potential energy of the wave induced motions with the group velocity. These aspects will be treated in Section 2.4.



Similarly a transport equation can be derived for dissipation rate  $\epsilon$ . This so-called  $\epsilon$ -equation can be derived exactly (Chou, 1945) using manipulations of the gradient of the Navier-Stokes equations to obtain the transport equation for  $\langle \underline{d} : \underline{d} \rangle$ .

Alternatively, an approximation for the  $\epsilon$ -equation for high Reynolds numbers can be derived in a less tedious manner by considering the Helmholtz equation for transport of fluctuating vorticity  $\underline{\omega}'$  and using the approximation (2.2.24), see (Tennekes and Lumley, Section 3.3, 1983). Although the last procedure is less complicated than Chou's derivation in both cases the resulting equation remains unwieldy.

We summarize this section as follows. In this Section the analogy between mixing of constituents and mixing of momentum has been discussed. It has led to the definition of eddy viscosity and of eddy diffusivity for transverse fluxes of momentum and of constituents respectively in a simple unidirectional flow in x-direction with only transverse mean gradients.

The extension of the concept of eddy viscosity/diffusivity towards fluxes in the remaining horizontal directions in more complicated flows with significant gradients in flow direction, such as  $\partial \langle \phi \rangle / \partial x$  etc., encounters difficulties. As shown by Corrsin (1959) the variance  $\langle X'^2 \rangle$  of streamwise displacements increases with  $T^3$  for large enough travel times  $T$  in equations, similar to (2.2.10), for  $\langle X'^2 \rangle$ . Hence, if this result is substituted into a definition equivalent to (2.2.17) for the horizontal eddy diffusivity, the latter would become unbounded. However, careful derivations using the correct displacements show that there is no anomaly and a finite eddy diffusivity is obtained for  $T \rightarrow \infty$ . This derivation is beyond the scope of this report.

The preceding brief and limited introduction to some of the properties of turbulence will assist us in posing, in the following section, the problem dealt with in this report.

## 2.3 The problem of turbulence in stably stratified flows

In absence of the inevitable viscous dissipation rate  $\epsilon$  of  $q^2$  and in addition neglecting diffusive effects, Richardson (1920) concluded that if the ratio

$$Rf = \frac{B}{P} \quad (2.3.1)$$

exceeds unity, turbulence can no longer persist. This dimensionless number  $Rf$  is called the flux-Richardson number and equals the efficiency of regaining the potential energy content of the mean flow through the production of turbulence. Many experiments (Linden, 1979) have shown that the efficiency of this conversion is limited to  $Rf \leq 1/4$ . However, by implying the Reynolds analogy,  $\sigma_T = 1$ , Richardson actually concluded that if the ratio

$$Ri = \frac{N^2}{\left\langle \frac{\partial u}{\partial z} \right\rangle^2 + \left\langle \frac{\partial v}{\partial z} \right\rangle^2} ; \quad N^2 = -\frac{g}{\langle \rho \rangle} \left\langle \frac{\partial \rho}{\partial z} \right\rangle \quad (2.3.2)$$

exceeds unity, turbulence must vanish. The number  $Ri$  in (2.3.2) is called the gradient Richardson number. From definitions (2.2.18), (2.3.1) and (2.3.2) follows the connection between  $Ri$ ,  $Rf$  and the turbulent Prandtl/Schmidt number

$$\sigma_T = \frac{v_T}{\Gamma_T} = \frac{Ri}{Rf} \quad (2.3.3)$$

In experiments the gradient Richardson number  $Ri$  can be imposed whereas the flux Richardson number  $Rf$  is the outcome of the experiment. The earliest field measurement towards this question appears to be reported by Jacobsen (1913) in the shallow, salt stratified Kattegat. Taylor concluded that, except for one disputable measurement, holds

$$\sigma_T \geq Ri \text{ for } 4 \leq Ri \leq 30.$$

Consequently, by virtue of (2.3.3)  $Rf \leq 1$  and thus turbulence can exist. These and other findings has led to a variety of semi-empirical formulas for an assumed universal function  $\sigma_T = \sigma_T(Ri)$ . A review of experimental research and a collection of different empirical formulations is summarized in (Karels, 1974).

Now the problem is how to explain the violation of the estimation  $\sigma_T \approx 1$  based on turbulence which mixes mass nearly as efficient as momentum. Taylor concludes (1931, p 41) : "The idea latent in the formula (here equation (2.3.3) with  $Rf=1$ ) is that different modes of disturbance correspond to different values of  $\sigma_T$  but the existence of a (stable) density gradient operates so as to prevent the formation of modes of disturbances which are such that the rate of increase of gravitational potential energy in any region would be greater than the rate at which the Reynolds eddy stresses communicate energy to that region."

Thus we are looking for properties of these nonturbulent modes assessed by Taylor, that allow for equivalent turbulent Prandtl/Schmidt numbers exceeding unity. This is the subject of the next section which shows the point of view taken in this report.

## 2.4 Nonturbulent fluctuations in stably stratified flows

In literature frequently the properties and conditions of instabilities and of internal waves are treated separately by the application of different mathematical tools, such as stability analysis and ray tracing methods. These different approaches, presented in separate publications in journals with different scopes, allow for precise and careful considerations of each subject. However, the notion that the same basic theme underlies these rather elaborate computations is not made clear. For the construction of a model which includes the different processes this is unsatisfactory. In what follows we present a unified approach. In essence, the approach is based on the Taylor-Goldstein equation for infinitesimal fluctuations superimposed on an unidirectional stratified flow with a vertical profile  $U(z)$  of the streamwise velocity component, see Fig. 2.4.1. This approach allows for the introduction of instabilities at small, positive  $Ri$ -numbers. In addition, the approximate description of fluxes induced by internal waves.

Consider the set of linearized equations for an incompressible, frictionless and diffusionless, stratified flow using the Boussinesq approximation and with mean horizontal velocity  $\underline{U} = (U, V, W)$  with vertical profile  $U(z)$  in  $x$ -direction,  $V=W=0$  and mean density profile  $\langle \rho(z) \rangle$  :

$$\vec{\nabla} \cdot \underline{\tilde{u}} = 0 ; \frac{\overline{D}\tilde{\rho}}{Dt} + \tilde{w} \frac{\partial \langle \rho \rangle}{\partial z} = 0 ; \frac{\overline{D}\tilde{u}}{Dt} + \tilde{w} \cdot \frac{dU}{dz} + \frac{1}{\rho_0} \vec{\nabla} \tilde{p} - \frac{\tilde{\rho}}{\rho_0} g = 0 ; \frac{\overline{D}}{Dt} = \left( \frac{\partial}{\partial t} + U \cdot \frac{\partial}{\partial x} \right). \quad (2.4.1)$$



Now assume infinitesimal wavelike perturbations of the vertical velocity component  $\tilde{w}$  of the form

$$\tilde{w} = \hat{w}(z) \exp[i(kx + \ell y - \omega t)] \quad (2.4.2)$$

We allow  $\hat{w}(z)$  to be complex valued. Further, the wavenumber components  $k$  and  $\ell$  as well as the angular frequency  $\omega$  are fixed. Taylor (1931) obtained the following equation, usually referred to as the Taylor-Goldstein equation by Hazel (1972), for the amplitude  $\hat{w}(z)$ :

$$\frac{d^2 \hat{w}}{dz^2} + Q(z) \cdot \hat{w}(z) = 0; \quad Q(z) = \frac{(k^2 + \ell^2) N^2}{k^2 (U - c)^2} - (k^2 + \ell^2) - \frac{1}{U - c} \cdot \frac{d^2 U}{dz^2}, \quad (2.4.3)$$

with complex-valued phase velocity  $c = \omega/k = c_r + ic_i$ .

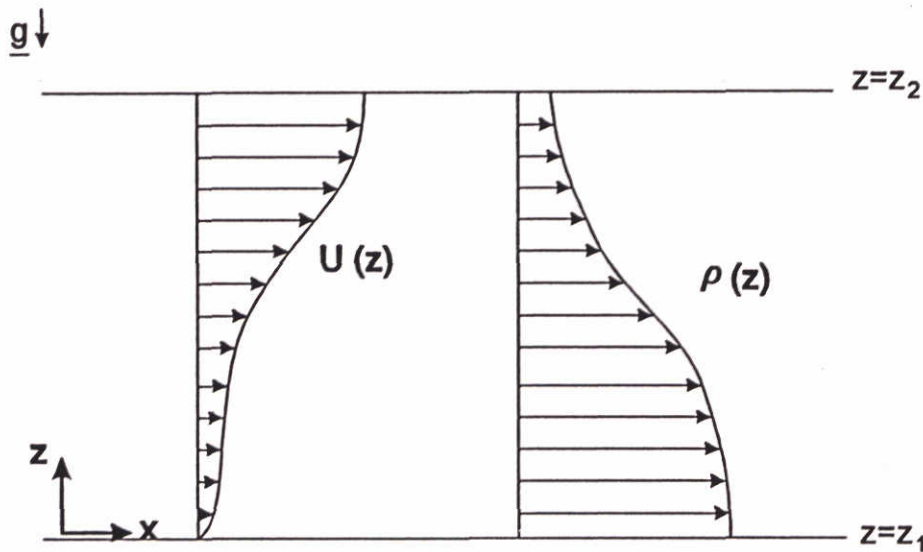


Fig. 2.4.1. An example of profiles for the mean density and for the mean horizontal velocity that may be used in the Taylor-Goldstein equation.

Actually, with suitably chosen boundary conditions at level  $z_1$  and at level  $z_2$  equation (2.4.3) is an eigenvalue problem with eigenvalues  $c$  and eigensolutions or modes  $\hat{w}$ . For frequently occurring velocity and density profiles Hazel (1972) investigated numerically the appearance of unstable modes.

First, without paying attention to boundary conditions, we briefly make some remarks for classes of solutions to (2.4.3) possessing a real-valued phase velocity. Observe with (2.4.3) that for vanishing stratification and for vanishing curvature of the horizontal flow,  $\hat{w}(z)$  satisfies the potential flow solution

$$\hat{w}(z) = W_{\pm} \cdot \exp[\pm (k^2 + \ell^2)^{1/2} z] \quad (2.4.4)$$

similar to the motions induced by surface waves on a uniform flow. For real phase velocity  $c$  and  $U(z) \rightarrow c$  at level  $z_c$  follows for  $Q(z)$  that  $|Q(z)| = O(Ri |z - z_c|^{-2}) \rightarrow \infty$  and the equation becomes singular. Near this so-called critical level  $z_c$  the solution  $\hat{w}(z)$  behaves as, see e.g.

(Booker and Bretherton, 1967):

$$\hat{w}(z) = W_{\pm} |z - z_c|^{\frac{1}{2}} \cdot \cos[\ln |z - z_c| + \phi_{\pm}] , \quad (2.4.5)$$

$$\text{and } \lim_{z \rightarrow z_c} \frac{W_+}{W_-} = \exp(\pm 2\pi \cdot \text{Ri}) .$$

The  $\pm$ -sign in the exponential function depends on the direction from which the energy is supplied towards the critical layer. In (2.4.5) the sign as subscript of the phase  $\phi$  and of the amplitude  $W$  equals the sign of  $(z - z_c)$ .

Hence,  $\hat{w}(z)$  rapidly oscillates in  $z$  and for large  $\text{Ri}$  the amplitude jumps across the critical layer (Booker and Bretherton, 1967). By virtue of the incompressibility condition and (2.4.5) for  $z \rightarrow z_c$  the shear rate  $d\hat{u}/dz$  increases proportional with  $Q(z)$  which grows as  $|z - z_c|^{-2}$ . Hence, the neglected viscous effects and nonlinear become important at the critical level. This is shown by numerical computations of Hazel (1967) whereas Breeding (1972) investigated numerically the limited nonlinear effects near the critical level. Later, in Section 2.5 we will come back to phenomena near this important critical level.

Another, weaker singularity, a so-called caustic, occurs at level  $z = z_r$  where  $Q(z_r) = 0$  and  $Q$  changes sign. The solution is oscillatory in  $z$  for  $z > z_r$  but on the opposite side of the caustic,  $z < z_r$  it decays nonoscillatory. It can be shown that internal waves travelling in  $z$ -direction towards  $z = z_r$  are reflected there.

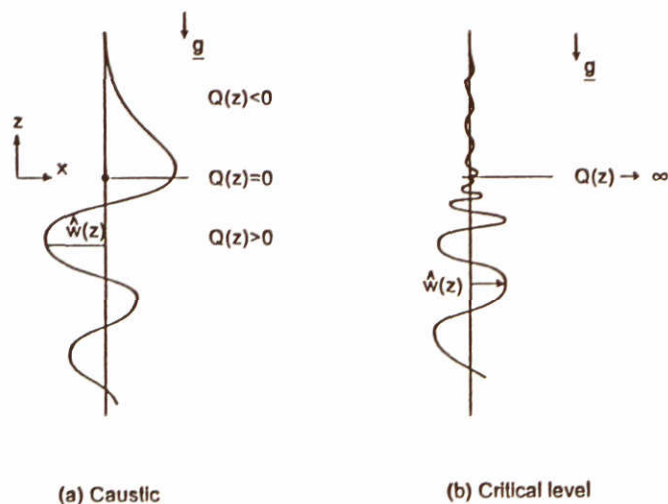


Fig. 2.4.2. Examples of solutions to the Taylor-Goldstein equation.

Hence, positive values of  $Q$  refer to wavelike solutions of  $\hat{w}$  as a function of  $z$  which we define as internal waves. In this report we will mainly study solutions or modes of (2.4.8) with  $Q > 0$  at least in a part of the fluid volume. Fig. 2.4.2 shows typical modes near the critical level and near a caustic.

Next, a complex-valued phase velocity is considered. If a solution to (2.4.3) exists for negative  $c_i$ , i.e. decaying in time, then also an exponentially growing mode for  $c_i$  exists.



Squire's theorem (Drazin and Reid, 1981) shows that for  $\ell=0$  the solutions to the Taylor-Goldstein equation are the least stable. Howard (1961) derived a sufficient condition for stable solutions to (2.4.3) i.e. with  $c_i=0$ . He showed that if holds  $\hat{w}(z_1)=0$  and  $\hat{w}(z_2)=0$  and  $Ri > \frac{1}{4}$  then the only solution is  $c_i=0$ , hence stable waves. In addition Howard showed that if  $c_i \neq 0$  then  $c_r$  lies in the range  $\{\min(U), \max(U)\}$ . Thus for neutrally stable modes i.e.  $c_i \rightarrow 0$  holds  $(U(z) - c) \rightarrow 0$  at some level  $z_c \in (z_1, z_2)$  and (2.4.3) becomes singular: the level  $z_c$  is called the critical layer.

In addition, for  $Ri > \frac{1}{4}$  growing waves can occur, for instance, if holds  $\hat{w}(z_2)=0$  but  $\hat{w}(z_1) \neq 0$  like the flow along a corrugated bottom topography. In meteorology this called orographic generation (Palmer et al., 1986). As investigated by Hazel (1972), depending on the particular velocity and density profile, the sufficient condition of  $Ri > \frac{1}{4}$  for stationary waves can be replaced by another necessary one with a value in the range  $(0, \frac{1}{4})$ .

For small enough Richardson number the growing solution to the Taylor-Goldstein equation is called the Kelvin-Helmholtz instability. Initially, this instability consists of rolling up and subsequent merging of two-dimensional vortices (Fig. 2.4.3). However, soon after this well-organized stage, three dimensional instabilities take over and turbulence evolves.

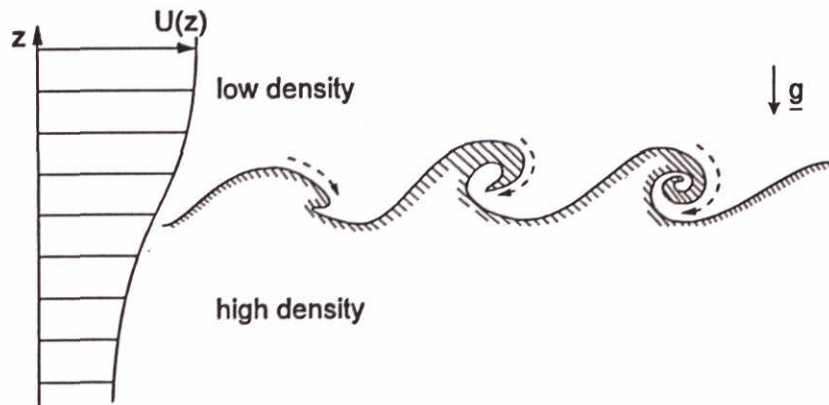


Fig. 2.4.3. The evolution of the Kelvin-Helmholtz instability in stably stratified flow at sufficiently small, positive  $Ri$ -number.

Although  $c_i=0$  holds for  $Ri > \frac{1}{4}$ , a critical layer and thus a singular solution may exist as discussed previously. Hence, despite the sufficient condition  $Ri > \frac{1}{4}$  for linear stability other instabilities, not incorporated in (2.4.3), may appear. These other additional instabilities can produce turbulence as well as and thus involve mixing of mass. We will come back to this subject later in this section.

Of importance is the force  $\tilde{T}_x$  which appears in the streamwise momentum equations. First, we present this force for wave-induced motions parallel to the flow plane i.e. with  $\ell=0$ . Using  $\tilde{\nabla} \cdot \tilde{\mathbf{u}} = 0$ ,  $\tilde{v} = 0$  as well as the streamwise horizontal momentum equation in (2.4.1) yields the contribution to the vertical momentum flux  $\langle u'w' \rangle$  that appears in (2.2.6):

$$\text{Re} \langle \tilde{u} \tilde{w}^{\text{cc}} \rangle = \frac{i}{4k} \cdot \left( \tilde{w}^{\text{cc}} \cdot \frac{d\tilde{w}}{dz} - \tilde{w} \cdot \left( \frac{d\tilde{w}}{dz} \right)^{\text{cc}} \right) \quad \text{for } \ell=0. \quad (2.4.6)$$

For finite  $\hat{w}$  and  $d\hat{w}/dz$  this expression yields the contribution  $\tilde{T}_x$  to the force  $T_x$  defined in (2.2.3):

$$\tilde{T}_x = -\frac{d\text{Re}\langle \hat{u}\hat{w}^{\infty} \rangle}{dz} = -\frac{1}{k} \langle \hat{w}^2 \rangle \text{Im} Q, \quad (2.4.7)$$

where  $Q$  has been defined in (2.4.3) and hence

$$\tilde{T}_x = \frac{\bar{D} \frac{1}{2} \langle \tilde{Z}^2 \rangle}{Dt} \left[ \frac{d^2 U}{dz^2} + 2N^2 \frac{c_r - U}{|U - c|^2} \right] \text{ for } \ell = 0, \quad (2.4.8)$$

$$\text{with } \hat{w} = \frac{\bar{D} \tilde{Z}}{Dt}, \quad \langle \hat{w}^2 \rangle = \frac{1}{2} \langle \hat{w} \hat{w}^{\infty} \rangle \text{ and likewise } \langle \tilde{Z}^2 \rangle = \frac{1}{2} \langle \hat{Z} \hat{Z}^{\infty} \rangle.$$

Observe in (2.4.8) that for vanishing stratification,  $N \rightarrow 0$ , an expression is obtained which resembles the one derived by Taylor for turbulence, however, now with the material derivative of  $\langle \tilde{Z}^2 \rangle$  before the second-order derivative  $d^2 U/dz^2$ .

For internal waves, with  $c_i = 0$   $\text{Im} Q = 0$  and then  $\tilde{T}_x = 0$ . Across a critical layer the momentum fluxes jumps according to the ratio (2.4.5) and there  $\tilde{T}_x \neq 0$ . The condition  $\tilde{T}_x = 0$  for  $c_i = 0$  is called the noninteraction theorem of Eliassen and Palm (1961). This theorem states that stationary fluctuations induce stresses which are in mutual equilibrium i.e. they do not create an acceleration of the mean flow. If the solution is steady ( $c_i = 0$ ) and  $\hat{w}(z_0) = 0$  holds somewhere in the flow then by virtue of (2.4.7) and (2.4.8) holds  $\langle \bar{u} \bar{w} \rangle = 0$  everywhere. In view of (2.4.7) this implies that the ratio  $\text{Im}(\hat{w})/\text{Re}(\hat{w})$  is independent of  $z$  which can be recognized as standing internal waves.

In the following we present several expressions for fluxes of momentum and of mass induced by infinitesimal oscillatory motions in a stably stratified fluid. For convenience we will express the mass flux vector and the streamwise shear stress in terms of the variance of the wave-induced vertical displacement  $\tilde{Z}$ . Actually, this variance can be estimated from observations of density fluctuations at a fixed spatial point. In Chapter 4 we will discuss our field observations using spectral analysis of time series. The properties presented below are then considered as spectral components per streamwise wavenumber  $k$  and averaged over the transverse wavenumber  $\ell$  as well as averaged over the vertical wavenumber  $m$ .

First we define the vertical wavenumber  $m$  from the infinitesimal perturbations (2.4.2) now expressed for the complex-valued amplitude of the vertical displacement  $Z$  as:

$$\tilde{Z}(x, t) = \tilde{Z}(z) \exp[i(kx + \ell y - \omega t)] \quad (2.4.2)$$

From the vertical variations of  $\hat{w}(z)$  we derive the local vertical wavenumber component  $m$  by first writing

$$\hat{Z}(z) = |\hat{Z}(z)| \cdot \exp[i\phi_Z(z; k, \ell)] \quad (2.4.9)$$

Related to (2.4.9) we define the vertical wavenumber  $m$  belonging to the perturbations with horizontal wavenumber components  $(k, \ell)$  as:

$$m = \frac{\partial}{\partial z} \phi_Z(z; k, \ell) \quad (2.4.10)$$



Despite this definition the interpretation that  $m$  actually is a wavenumber is only meaningful if the modulus  $|\hat{Z}(z)|$  varies slowly over the vertical distance  $2\pi/m$ . In Section 2.5 we will specify this notion mathematically.

Moreover, the definition (2.4.10) of the vertical wavenumber component shows that  $m$  is actually an independent variable, however, in the following we will conveniently express the results in the wavenumber vector  $\underline{k} = (k, \ell, m)$ . From (2.4.2) and (2.4.9) follows for the variance of the vertical displacement:

$$\langle \tilde{Z}^2 \rangle = \frac{1}{2} |\hat{Z}|^2 \quad (2.4.11)$$

Further, we define the angular frequency  $\Omega$  as the real part of  $k(c-U)$

$$\Omega = k(c_r - U), \quad (2.4.12)$$

whereas the imaginary part of  $kc_i = \text{Im}\{k(c-U)\}$  is written as

$$\beta = kc_i \quad (2.4.13)$$

$$\text{so that } \beta^2 + \Omega^2 = |k(U - c)|^2. \quad (2.4.14)$$

In the spirit of the Taylor-Goldstein equation we will use the property

$$\beta \langle \tilde{Z}^2 \rangle = \frac{1}{2} \frac{D \langle \tilde{Z}^2 \rangle}{Dt}. \quad (2.4.15)$$

In particular, the following analytical expressions will be useful. Elimination of pressure yields:

$$\hat{u} = \frac{1}{k^2 + \ell^2} \left( i k \frac{d\hat{w}}{dz} + \ell^2 \hat{Z} \frac{dU}{dz} \right), \quad (2.4.16a)$$

$$\hat{v} = \frac{1}{k^2 + \ell^2} \left( i \ell \frac{d\hat{w}}{dz} + k \ell \hat{Z} \frac{dU}{dz} \right), \quad (2.4.16b)$$

$$\hat{w} = i k (U - c) \hat{Z}. \quad (2.4.16c)$$

These expressions in conjunction with the Taylor-Goldstein equation enable us to express fluxes etc. into mean flow variables and the magnitude  $\hat{Z}$  of the wave-induced vertical displacement. For the latter we will define in Chapter 3 estimators which can be derived from field observations.

The wave-induced shear stress at wavenumber vector  $\underline{k}$  follows from (2.4.16)

$$\text{Re} \langle \tilde{u} \tilde{w}^\infty \rangle = -\frac{1}{2} \frac{D \langle \tilde{Z}^2 \rangle}{Dt} \frac{dU}{dz} - \frac{k \cdot m}{k^2 + \ell^2} (\beta^2 + \Omega^2) \langle \tilde{Z}^2 \rangle. \quad (2.4.17)$$

Note that differentiation of (2.4.17) with respect to  $z$  yields the streamwise force  $\{-\tilde{T}_x\}$  for the general case  $\ell \neq 0$ . Then the first term in (2.4.17) now is equivalent to (2.2.8) with  $\sigma_T = 1$ . The complex-valued product of the wave-induced density fluctuations with the complex conjugate of the wave-induced vertical velocity reads:

$$\langle \bar{\rho} \tilde{w}^{cc} \rangle = - \left( \frac{\bar{D}^{1/2} \langle \tilde{Z}^2 \rangle}{Dt} + i \Omega \langle \tilde{Z}^2 \rangle \right) \left\langle \frac{\partial \rho}{\partial z} \right\rangle. \quad (2.4.18)$$

Later, in Chapter 4, we will interpret (2.4.18) as the cross spectrum of infinitesimal internal waves. The real part of the cross spectrum is called coincidence spectrum and its imaginary part the quadrature spectrum. Actually, the real part, the coincidence spectral component, of (2.4.18) is the buoyancy-flux and we will abbreviate the imaginary part as the quadrature related to the vertical velocity component. Equation (2.4.18) shows that the buoyancy flux is positive for growing waves and this growth represents the increase of fluctuating potential energy. For small changes in variance  $\langle \tilde{Z}^2 \rangle$  the expression (2.4.18) shows that the phase angle between  $\bar{\rho}$  and  $\tilde{w}$  is close to  $\pm 90^\circ$ .

Moreover, the horizontal wave-induced mass fluxes as well as their quadratures are observable and hence their analytical expressions are of interest. Although the derivation of these mass fluxes are cumbersome we will present them without further introduction.

The streamwise, wave-induced mass flux at wavenumber vector  $\underline{k}$  reads:

$$\text{Re} \langle \bar{\rho} \tilde{u}^{cc} \rangle = \left( \frac{1}{k^2 + \ell^2} \frac{dU}{dz} + k \gamma \right) \langle \tilde{Z}^2 \rangle \left\langle \frac{\partial \rho}{\partial z} \right\rangle, \quad (2.4.19)$$

where

$$\gamma = \frac{1/2 m \Omega}{k^2 + \ell^2} \cdot \left( \frac{1}{\Omega} \frac{\bar{D}}{Dt} \left( \frac{d|\tilde{Z}|^2}{dz} \right) - \frac{1}{m} \frac{d|\tilde{Z}|^2}{dz} \right). \quad (2.4.20)$$

If the wave field is practically stationary and the wave field depends only weakly on the vertical coordinate  $z$  then  $\gamma$  in (2.4.20) becomes insignificant and the first term in the RHS of (2.4.19) dominates. Actually, this term is the Stokes drift for mass due to internal wave motions in a shear flow. The wave-induced quadrature between density and streamwise velocity reads:

$$\text{Im} \langle \bar{\rho} \tilde{u}^{cc} \rangle = \frac{k}{k^2 + \ell^2} \left[ \frac{1}{8} \frac{\bar{D}}{Dt} \left( \frac{d|\tilde{Z}|^2}{dz} \right) + m \Omega \langle \tilde{Z}^2 \rangle \right] \left\langle \frac{\partial \rho}{\partial z} \right\rangle \quad (2.4.21)$$

For stationary waves the last term is the streamwise contribution to the quadrature of  $\langle \bar{\rho} \tilde{v}^{cc} \rangle$ . Similarly, the transverse mass flux reads:

$$\text{Re} \langle \bar{\rho} \tilde{v}^{cc} \rangle = (\ell \gamma) \langle \tilde{Z}^2 \rangle \left\langle \frac{\partial \rho}{\partial z} \right\rangle. \quad (2.4.22)$$

$$\text{Im} \langle \bar{\rho} \tilde{v}^{cc} \rangle = \frac{\ell}{k^2 + \ell^2} \left[ \frac{1}{8} \frac{\bar{D}}{Dt} \left( \frac{d|\tilde{Z}|^2}{dz} \right) + m \Omega \langle \tilde{Z}^2 \rangle \right] \left\langle \frac{\partial \rho}{\partial z} \right\rangle. \quad (2.4.23)$$

For stationary waves the last term in (2.4.23) is the only contribution to the quadrature of the transverse mass flux. The transverse component (2.4.22) of the mass flux possesses no Stokes drift. Actually, the transverse component (2.4.22) is proportional to  $\gamma$  defined in (2.4.20) and  $\gamma$  contains the vertical derivative as well as the material derivative of the variance of the wave-induced vertical displacement.

If we regard the quadratures  $\text{Im} \langle \bar{\rho} \tilde{u}_i^{cc} \rangle$  with  $(i=1,2,3)$  as orthogonal components of a vector then the magnitude of this vector reads

$$\left( \text{Im} \langle \bar{\rho} \tilde{u}_1^{cc} \rangle, \text{Im} \langle \bar{\rho} \tilde{u}_2^{cc} \rangle \right)^{1/2} = \langle \tilde{Z}^2 \rangle \left\langle \frac{\partial \rho}{\partial z} \right\rangle \frac{\Omega |\underline{k}|}{k_h} (1 + \mu^2)^{1/4}. \quad (2.4.24)$$



where

$$\mu = \frac{1}{4 \Omega |\mathbf{k}| |\hat{Z}|^2} \frac{\overline{D}}{Dt} \left( \frac{d|\hat{Z}|^2}{dz} \right). \quad (2.4.25)$$

For vanishing relative changes as well as vanishing vertical derivative of the wave-induced vertical displacement variance holds  $\mu \rightarrow 0$ . Then equation (2.4.24) will yield an expression for the sum of kinetic and potential energy of fluctuations induced by internal gravity waves. However, further exploration of (2.4.24) is postponed until the dispersion relation  $\Omega = \Omega(\mathbf{k})$  has been derived in the next section. Instead, we continue with the variances of velocity components.

Twice the variance of the streamwise fluctuations reads:

$$|\hat{u}|^2 = \frac{m^2 k^2}{(k^2 + \ell^2)^2} (\beta^2 + \Omega^2) |\hat{Z}|^2 \left[ 1 + \left( \frac{1}{m |\hat{Z}|} \frac{d|\hat{Z}|}{dz} \right)^2 \right] + k \gamma |\hat{Z}|^2 \frac{dU}{dz} + |\hat{Z}|^2 \left( \frac{dU}{dz} \right)^2. \quad (2.4.26)$$

The variable  $\beta$  in (2.4.26) has been defined in (2.4.13) and (2.4.15). Further, for stationary variance as well zero vertical derivative of the wave-induced vertical displacement, the variable  $\gamma$ , defined in (2.4.20), disappears. However, in (2.4.26) there still remains its last contribution

$$|\hat{Z}|^2 \left( \frac{dU}{dz} \right)^2 \quad (2.4.27)$$

to the variance of  $u$ . It is induced by vertical perturbations on the mean vertical gradient  $dU/dz$ . Of course this contribution disappears in the following expression for the variance of the transverse velocity fluctuations

$$|\hat{v}|^2 = \frac{\ell^2 m^2}{(k^2 + \ell^2)^2} (\beta^2 + \Omega^2) |\hat{Z}|^2 \left[ 1 + \left( \frac{1}{m |\hat{Z}|} \frac{d|\hat{Z}|}{dz} \right)^2 \right]. \quad (2.4.28)$$

While the variance of the vertical velocity component simply yields

$$|\hat{w}|^2 = (\beta^2 + \Omega^2) |\hat{Z}|^2. \quad (2.4.29)$$

Hence, twice the kinetic energy reads:

$$\hat{\mathbf{u}} \cdot \hat{\mathbf{u}}^{\infty} = \frac{|\mathbf{k}|^2}{k^2 + \ell^2} (\beta^2 + \Omega^2) |\hat{Z}|^2 \left[ 1 + \left( \frac{1}{|\mathbf{k}| |\hat{Z}|} \frac{d|\hat{Z}|}{dz} \right)^2 \right] + k \gamma |\hat{Z}|^2 \frac{dU}{dz} + |\hat{Z}|^2 \left( \frac{dU}{dz} \right)^2. \quad (2.4.30)$$

For steady waves as well as for an uniform vertical distribution of wave energy (2.4.30) simplifies to the following expression for the kinetic part of the wave energy

$$\frac{1}{2} \langle \hat{\mathbf{u}} \cdot \hat{\mathbf{u}} \rangle = \frac{1}{2} \langle \hat{Z}^2 \rangle \left[ \frac{|\mathbf{k}|^2}{k^2 + \ell^2} \Omega^2 + \left( \frac{dU}{dz} \right)^2 \right]. \quad (2.4.31)$$

This result is essential to this report because it expresses the kinetic energy of velocity fluctuations, satisfying the Taylor-Goldstein equation, into the variance of vertical displacement. Later we will introduce measurable estimators for the wave-induced vertical displacement.

Further, the combination of vertical gradient of the streamwise velocity component and the vertical wave-induced displacement provides an additional contribution to the variance  $\langle \tilde{u}^2 \rangle$ , see (2.4.26) and (2.4.27). This is represented by the last term in (2.4.31) and makes (2.4.31) dependent of the gradient Richardson number (2.3.2).

Finally some additional remarks. Observe that the first part of the expression (2.4.17) for the shear stress is similar to Taylor's estimation (2.2.18) with (2.2.19) for turbulence. However, the essential property of turbulence is the ever increasing variance  $\langle Z'^2 \rangle$  and thus a positive eddy diffusivity. In contrast with turbulence, however, the variance  $\langle \tilde{Z}^2 \rangle$  may decrease for decaying waves so that the buoyancy flux is opposite to the one induced by turbulence. Then the equivalent wave-induced eddy diffusivity becomes negative for decaying waves. This reversal derived with linear theory cannot be interpreted as "de-mixing" of, for instance, salt and fresh water but implies the restoration of the initial density profile before the waves perturbed it in a regular, well-ordered and reversible way.

For steady fluctuations, by virtue of (2.4.15) the buoyancy-flux, which is the real part of (2.4.17), vanishes. Then, outside critical layers, also the wave force  $\tilde{T}_x$  vanishes but not necessarily the shear stress (2.4.17). Hence, the fluxes of momentum and of mass induced by modes satisfying the Taylor-Goldstein equation exhibit not a distinct mutual relation in contrast with the turbulence fluxes of momentum and of mass. This difference may be the origin of the experimentally observed anomaly of the "turbulent" Prandtl/Schmidt number exceeding unity in stratified flows at large Ri numbers as discussed in Section 2.3.

## 2.5 Description of nonturbulent fluctuations in stably stratified flows as slowly varying internal waves

In the following we will relate the well-known properties of internal gravity waves to the Taylor-Goldstein equation. Many textbooks give these properties, see for instance (Turner, 1979), (Phillips, 1980), (Gill, 1981), (Pedlosky, 1979).

Before we continue estimating the energy fluxes, first approximations to solutions of (2.4.1) are presented without paying attention to boundary conditions. These solutions reveal some of the properties of freely-travelling, internal waves. In contrast with turbulence, waves of infinitesimal amplitude exhibit a distinct connection, the dispersion relation, between the so-called intrinsic frequency  $\Omega$  of the waves measured by an observer moving along with the mean flow and the state parameters of the waves such as their wavenumber  $\underline{k}$ . That the solutions to the Taylor-Goldstein exhibit wave properties, defined in this manner, may not be immediately obvious from the discussion presented in Section 2.4. Therefore, the present Section is devoted to make these wave properties clear by assuming that particular properties of the modes are either slowly or either rapidly varying in space. Then we can derive the dispersion relation and relate the shear stress to the wavenumber vector and to the energy of the wave. In addition, we derive the conservation equation of the so-called wave action as a counterpart of the  $q^2$ -equation of Section 2.2 etc..



The essential starting point of this Section lies in the assumption that if we write similar to (2.4.2)

$$\hat{w}(z) = F(z) \cdot \exp i\phi(z) \quad (2.5.1a)$$

so that (2.4.2) yields

$$\bar{w}(\underline{x}, t) = F(z) \cdot \exp[i(kx + \ell y + \phi(z) - \omega t)] \quad (2.5.1b)$$

the amplitude  $F(z)$  varies slowly in comparison with the phase function  $\phi(z)$ . This is the essence of the WKB-asymptotic expansion (Wentzel, Kramers, Brillouin) see e.g. (Bender and Orszag, 1978). A similar statement is to assume that the length scale  $(\text{Re}Q)^{-1/2}$  is much smaller than the typical vertical length scale over which  $U(z)$  and  $N(z)$  vary. Hence, this approximation is valid for large positive Ri-numbers. Following (Gill, 1981) the substitution of (2.5.1a) into (2.4.1) and considering the real parts of (2.4.3) yields:

$$\left(\frac{d\phi}{dz}\right)^2 = Q + \frac{1}{F} \frac{d^2 F}{dz^2} \quad (2.5.2)$$

The second term in (2.5.2) is neglected compared to  $Q$ . This neglect implies slow spatial variations of  $F$  so that the approximation to (2.5.2) reads

$$\phi(z) \approx \pm \int^z Q^{1/2}(z') dz' , \quad (2.5.3)$$

where, instead of an additional constant, the lower bound of the integral is left unspecified. The solution for  $F(z)$  is straightforward and without further approximations it follows from the imaginary part of the Taylor-Goldstein equation (2.4.1) after substitution of (2.5.1). The final result, with the yet unspecified constant  $W_0$ , reads:

$$\hat{w}(z) = W_0 \cdot Q^{-1/4} \cdot \exp\left(\pm i \int^z Q^{1/2}(z') dz'\right) \quad (2.5.4)$$

By definition the wavenumber  $\underline{k} = \vec{\nabla} \Phi(\underline{x}, t)$  equals the spatial gradient of the total phase function  $\Phi(\underline{x}, t)$  of homogeneous and stationary oscillations which are proportional to  $\exp(i\Phi)$ . However, in (2.5.1b) we have already introduced this definition for the horizontal wavenumber components under the approximation of slow spatial variations of the wave amplitude. Hence, in virtue of (2.5.4) and (2.5.3) we define the vertical wavenumber component  $m(z)$  as:

$$m(z) = \pm (\text{Re}Q)^{1/2} , \quad (2.5.5)$$

provided  $\text{Re}Q \geq 0$ .

Observe, in view of (2.5.2), that the vertical wavenumber of (2.5.5) is not exact if the vertical distribution of the amplitude  $F(z)$  in (2.5.1a) possesses a curvature. In particular near a caustic (Fig. 2.4.2a), where  $F(z)$  tends to zero, the approximation (2.5.3) fails and thus definition (2.5.5) is not applicable near a caustic.

Further, according to the linear theory that led to the Taylor-Goldstein equation, holds  $\bar{D}\hat{w}/Dt = ik(U - c) \cdot \hat{w}$ .

This notion introduces the so-called intrinsic frequency, measured by a co-moving observer, and it is defined as

$$\Omega = k(c_r - U) \text{ and } \Omega \geq 0, \quad (2.5.6)$$

The definition (2.5.6) requires that if  $c_r < U$  then  $k < 0$ . This sign convention is necessary to unambiguously define the directions of the phase velocity and of the group velocity. The phase velocity  $c_p$  is defined as the velocity at which the phase is stationary. The group velocity  $c_g$  is defined as the energy flux vector divided by the energy and it can be shown that  $c_g = \partial\omega/\partial\mathbf{k}$ , see e.g. (Lighthill, 1965) and (Tolstoy, 1973).

For real-valued  $Q$  the definition (2.4.8) provides a so-called dispersion relation between  $\Omega$  and  $k, \ell$  and  $Q$  or  $m$  using (2.5.5); its solution yields

$$\Omega = \frac{k_h}{|\mathbf{k}|} N [\delta + (1 + \delta^2)^{1/2}], \quad (2.5.7)$$

$$\text{with } k_h = (k^2 + \ell^2)^{1/2}, \quad |\mathbf{k}| = (k^2 + \ell^2 + m^2)^{1/2} \text{ and } \delta = \frac{k}{k_h |\mathbf{k}|} N \frac{d^2 U}{dz^2}.$$

In the spirit of the WKB-approximation  $\delta$  must be negligible small because the vertical wavelength ( $2\pi/m$ ), hidden in the magnitude  $|\mathbf{k}|$  of the wavenumber vector  $\mathbf{k} = (k, \ell, m)$ , is assumed to be much smaller than the vertical length scale over which  $U(z)$  varies. Hence, in correspondence to the WKB-solution (2.5.4) the following dispersion relation is obtained:

$$\Omega = \cos\Theta(\mathbf{k}), \quad (2.5.8)$$

$$\text{with } \cos\theta = k_h / |\mathbf{k}|.$$

From (2.5.8) follows that the maximal intrinsic frequency of internal waves equals the so-called Brunt-Väisälä (radian) frequency  $N$ . Further, the WKB-approximations leading to (2.5.4) required large vertical wavenumbers  $m$  so that holds:

$$\frac{d\hat{w}}{dz} \approx im\hat{w}. \quad (2.5.9)$$

In the following we consider the connection between physical space and wavenumber space with respect to internal wave properties and directions. Define the unit vectors  $\mathbf{e}_x$ ,  $\mathbf{e}_y$  and  $\mathbf{e}_z$  as a Cartesian  $(x, y, z)$ -coordinate system in physical space. Similarly, define the unit vectors  $\mathbf{e}_k$ ,  $\mathbf{e}_\ell$  and  $\mathbf{e}_m$  as the Cartesian base in wavenumber space or Fourier space. Next, we connect the base vectors in physical space with those in wavenumber space as follows. Because the wavenumber components  $(k, \ell, m)$  are related to  $(x, y, z)$  respectively we may take advantage by defining the following equivalence:

$$\mathbf{k} = k\mathbf{e}_x + \ell\mathbf{e}_y + m\mathbf{e}_z \equiv k\mathbf{e}_k + \ell\mathbf{e}_\ell + m\mathbf{e}_m. \quad (2.5.10)$$

The components  $(\hat{u}(\mathbf{x}; \mathbf{k}), \hat{v}(\mathbf{x}; \mathbf{k}), \hat{w}(\mathbf{x}; \mathbf{k}))$  of  $\hat{\mathbf{u}}(\mathbf{x}; \mathbf{k})$  in physical space, with wavenumber  $\mathbf{k}$  as parameter, become the Fourier coefficients  $(\hat{u}(\mathbf{k}), \hat{v}(\mathbf{k}), \hat{w}(\mathbf{k}))$  in wavenumber space so that if holds  $\hat{u}(\mathbf{x})=0$  then also  $\hat{u}(\mathbf{k})=0$  etc..



We conclude from (2.5.9), the connection (2.5.10) between base vectors as well as the incompressibility condition  $\nabla \cdot \underline{\hat{u}} = 0$  that the wavenumber vector  $\underline{k}$  is said to be perpendicular to the amplitude vector  $\underline{\hat{u}}(\underline{x}; \underline{k})$  in physical space of a wave with wavenumber  $\underline{k}$  or, equivalently,  $\underline{k}$  is perpendicular to  $\underline{\hat{u}}(\underline{k})$  in wavenumber space:

$$\underline{k} \cdot \underline{\hat{u}}(\underline{x}; \underline{k}) = 0 ; \underline{k} \cdot \underline{\hat{u}}(\underline{k}) = 0 . \quad (2.5.11)$$

Actually,  $\underline{\hat{u}}$  equals the sum of contributions from different wavenumbers, a Fourier series. Consequently, (2.5.11) is a sufficient but not a necessary condition for incompressibility. Instead, incompressibility imposes the sum of  $(\underline{\hat{u}}(\underline{k}) \cdot \underline{k})$  to be zero so that, with a distinct phase coupling between the different modes, the individual contributions may deviate from (2.5.11). Hence, (2.5.11) either holds for a wave with energy in one distinct wavenumber or for random waves with mutually independent phase coupling. This last condition is formalized by Kraichnan (1959) for turbulence as the "principle of maximal randomness" or "the principle of weak dependence" (between modes).

In this report we mainly consider random internal waves and thus we rely on Kraichnan's principle and on (2.5.11).

In addition, from the linearized equations (2.5.7) follows, while neglecting the shear rate  $(dU/dz)$  i.e. very large Ri numbers,  $\hat{v} = (\ell/k)\hat{u}$  so that  $\underline{\hat{u}}(\underline{x}; \underline{k})$  lies in the plane that contains  $\underline{k}$  and the plane is parallel to the vertical z-coordinate in physical space or equivalently the plane is parallel to the vertical wavenumber axis in wavenumber space. Hence, internal gravity waves are transversal waves. By virtue of (2.5.11) and the property  $\hat{v} = (\ell/k)\hat{u}$  we may decompose  $\underline{\hat{u}}$  into vectors parallel with the unit vectors  $\underline{e}_1$  and  $\underline{e}_2$  both perpendicular to  $\underline{k}$  and defined below. This decomposition is called Craya decomposition and is presented in (Craya, 1958, p. 34) but based on the general theorem by Kampé de Fériet (1948) on spectra of homogeneous turbulence. The Craya decomposition yields

$$\underline{e}_1 = \frac{\underline{k} * \underline{g}}{|\underline{k} * \underline{g}|} ; \underline{e}_2 = \frac{\underline{k} * (\underline{k} * \underline{g})}{|\underline{k} * (\underline{k} * \underline{g})|} , \quad (2.5.12)$$

with  $\underline{g}$  the vector of gravitational acceleration.

In virtue of (2.5.10) the vectors  $\underline{e}_1$  and  $\underline{e}_2$  are defined in physical space as well as in wavenumber space. Hence, given  $(\underline{k}, \ell)$  and the angular frequency  $\omega$  the WKB-solutions to the Taylor-Goldstein equation are plane transversal waves with  $\underline{\hat{u}}$  parallel to  $\underline{e}_2$ , see Fig. 2.5.1. The contribution to  $\underline{\hat{u}}(\underline{k})$  and parallel with  $\underline{e}_1$  is called quasi two-dimensional turbulence but also more ambiguously the vortical component (of the velocity vector). This latter definition may be confusing because internal waves induce also vorticity: due to the buoyancy horizontal, force  $\bar{\rho}g$  in the momentum equations (2.4.7) the wave-induced vorticity  $\underline{\hat{\omega}} = \nabla * \underline{\hat{u}}$  is nonzero and is parallel with  $\underline{e}_1$ .

In contrast with two-dimensional turbulence the vertical vorticity of quasi two-dimensional turbulence may vary along the depth. Two-dimensional turbulence has only a nonzero component Fourier coefficients parallel  $\underline{e}_1$  for a horizontal wavenumber; in free surface flows this is a so-called barotropic mode. However, according to analysis of Riley, Metcalfe and Weissman (1981) extended in (LeLong and Riley, 1992) the vertical variability of the vertical vorticity component of quasi two-dimensional turbulence interacts with and/or induces internal waves. This is immediately clear from the vector property:

2 - 20



For the wave-induced shear stress can be written as:

$$-\langle \tilde{u} \tilde{w} \rangle = -k c_{gz}^+ \left( \frac{\tilde{E}}{\Omega} \right) \equiv -c_{gz}^+ P_x . \quad (2.5.16)$$

In (2.5.16) appears the x-component of the so-called pseudomomentum vector defined as

$$\underline{P} = \underline{k} \cdot A , \quad (2.5.17)$$

which is a wave property, second-order in velocity amplitude  $|\hat{u}|$ , and in (2.5.17) is A the well-known wave action (Bretherton and Garrett, 1968) defined as:

$$A = \frac{\tilde{E}}{\Omega} . \quad (2.5.18)$$

In addition, equation (2.4.1) reveals another expression for force  $\tilde{T}_x$ , provided the temporal variations of  $|\hat{u}|$  are slow so that  $c_i < c_r$ . Then equation (2.4.8) can be converted into

$$\tilde{T}_x = -k \cdot \frac{\bar{D}A}{Dt} + \frac{1}{2} \frac{k^2}{k^2 + \ell^2} \frac{\bar{D}\langle \tilde{Z}^2 \rangle}{Dt} \frac{d^2 U}{dz^2} . \quad (2.5.19)$$

Finally, the constancy of the angular frequency  $\omega = (kU - \Omega)$ , for instance in z-direction, may be used to obtain the following refraction equation for stationary internal waves:

$$c_{gz}^+ \frac{dm}{dz} = -k \frac{dU}{dz} + \cos \theta \frac{dN}{dz} . \quad (2.5.20)$$

Fig. 2.5.2 summarizes in Fourier space some properties of infinitesimal internal gravity waves. This figure may assist the reader in finding the correct signs and direction of shear stress, group velocity and the occurrence of a caustic or a critical level. The latter properties are related to physical space through Fig. 2.4.2 while using the vertical wavenumber m defined in (2.5.5).

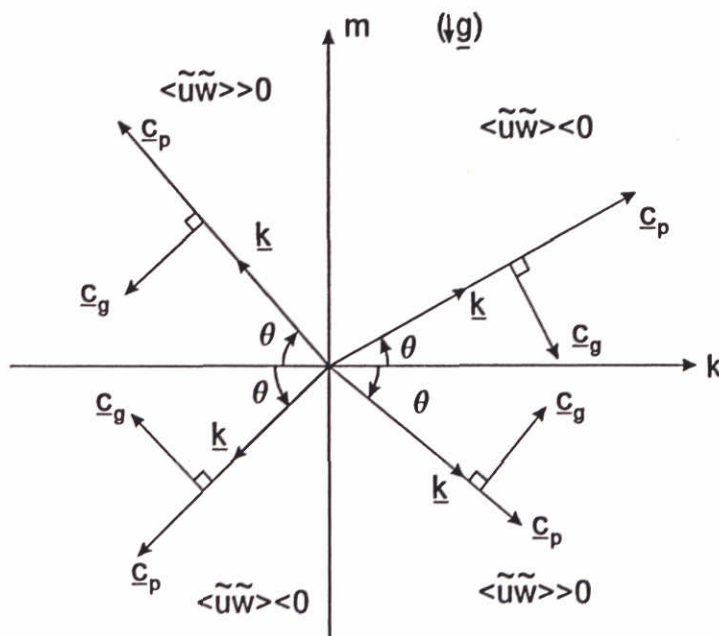


Fig. 2.5.2. Some properties of internal waves presented in Fourier space.

The differential equation (2.5.20) for  $m$  is important as it reveals that in Fourier-space the energy density  $\tilde{E}(\mathbf{k})$  related to  $\mathbf{k}$  is transported in  $m$ -direction and the initial spectrum of infinitesimal waves is shear-deformed by vertical gradients of  $U$  and of  $N$ . The formation of a caustic (Fig. 2.4.2a) yields  $m=0$  according to (2.5.5). In Fig. 2.5.3 this means the passage of  $k$ -axis by the wavenumber path (2.5.20) at constant  $k$ . Conversely, for  $m$  tending to infinity, at constant streamwise wavenumber  $k$ , we find the condition near a critical layer.

For instance, the formation of a critical layer, described mathematically by (2.4.5) and indicated by Fig. 2.4.2b. This can also be understood by tracing rays (path lines of group velocity) using (2.5.20). Fig. 2.5.2 shows an example of critical layer formation where holds  $U(z_c)=0$  if the internal waves were generated by an uneven bed where the vertical wave amplitude is prescribed. By means of the amplitude jump (2.4.5) over the critical level it can be shown that the shear stress jumps as well and thus  $T_x$  is nonzero. In this example, first the internal wave energy is generated near the bed and causes a flow drag:  $T_x$  acts locally against the flow. In meteorology this wave drag is significant and has been parametrized (Palmer et al., 1986). However, Kranenburg et al. (1991) estimated this drag as insignificant even for a strong forcing of lee waves in a section of the Rotterdam Waterway (salt stratified tidal shear flow).

The vertical flux of internal wave energy towards the critical level cannot pass this level. Near the critical level  $T_x$  accelerates the flow: the internal energy is converted into mean energy. On the one hand, without wave breaking nor viscous effects this energy conversion process is conservative. On the other hand the mean velocity profile will be affected by the internal waves, see (Fritts, 1982a, fig. 11) and (Fritts, 1982b, fig. 6, 10 and 15). Between the bed and the critical level the wave-induced shear stress remains constant, see the remarks following (2.4.8) for the Eliassen and Palm (1961) theorem: the depth-averaged wave-induced force is zero.

Similarly, internal waves can also be generated internally in the fluid by several hydrodynamic mechanism, including turbulence (Townsend, 1965, 1966, 1968), (Carruthers and Hunt, 1986) etc.. Under the idealized assumption that these internal waves do not break or suffer viscous effects, then also the net vertical energy transfer is conserved and the depth-averaged force remains zero. In reality this picture is disturbed by turbulence generation through a wave-induced strain rate and internal wave breaking. We will return to this subject, crucial for this report, in Chapter 3.

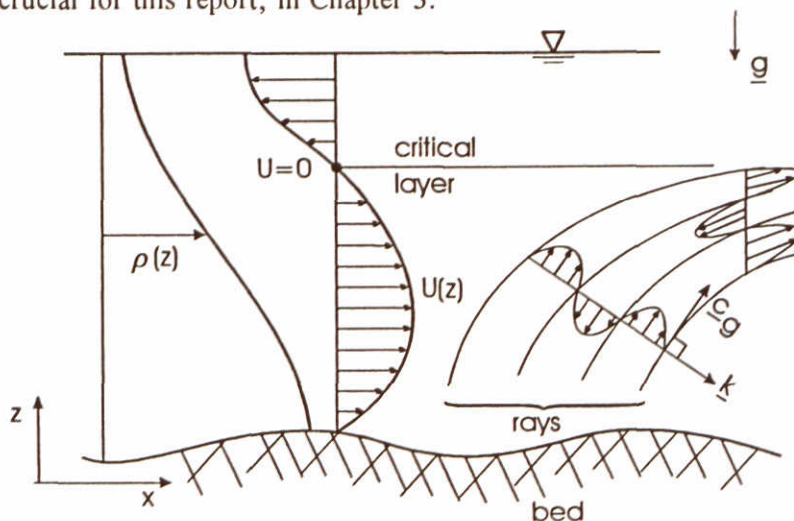


Fig. 2.5.3. An example of critical layer formation by an uneven bed in a tidal shear flow.



We close this section with the following remarks. In literature more detailed and more careful derivations and extensions have been given. The starting point for wave action applied to infinitesimal internal waves lies in (Garrett and Bretherton, 1968). However, Grimshaw (1972, 1984a) derived an equation in conservational form for wave action for large amplitude waves including viscous dissipation with slow temporal and spatial variations. Finally, Andrews and McIntyre (1978a, 1978b) gave the most general theorems for wave action without restrictions to slowness of wave properties. Grimshaw (1984) reviewed these studies using a Lagrangian concept.

All these derivations require periodicity related to some ensemble averaging parameter such as a phase, a spatial coordinate or time. For a group of waves with different wave numbers and/or intrinsic frequencies this periodicity cannot be fulfilled exactly. For instance, Grimshaw (1988) has derived the temporal and spatial exchange of wave action between three internal waves with different wavenumbers.

Apart from the following remarks we will not go into the complicated matter of wave-wave interaction theories, except for a brief discussion in Section 2.7.

Based on the assumption of selected, slow and weak interactions between waves at different wavenumbers Hasselmann (1968) provided a theoretical basis to describe the wave-wave interactions with similarities between interacting/colliding wave groups and the molecular collision theory of Boltzmann. Using Hasselmann's theory, researchers (McComas and Bretherton, 1977), (Müller and Olbers, 1975) have numerically computed spectra of and interactions between internal waves under oceanographic conditions. However, Holloway (1980) criticized the basic assumption in Hasselmann's theory about the slowness and weakness of the interactions for internal waves in the ocean using strong arguments based on the outcome of these computations. Gradually, the application of DNS has avoided the usage of similarities with Boltzmann's molecular collision integrals.

## 2.6 Instabilities of internal waves

To main purpose of this Chapter 2 is to establish a conceptual basis to understand turbulence production by internal waves. In the section, therefore, we review the relevant instabilities of internal waves. Then, in Chapter 3, we can consider known or newly formulated criteria for wave breaking and thus for turbulence production by internal waves. Finally, in Chapter 4, we will attempt to verify these conditions with our observations in the field.

In this section we will briefly review critical layer formation, some causes of internal wave breaking and we will estimate the wave-induced strain rate which may, irrespective of wave instabilities, also produce turbulence.

For an appreciation of the significance of critical layer formation in a stably stratified flow with a significant shear rate we estimate the vertical excursion over which an internal wave can travel before it reaches its critical layer. Consider an internal gravity wave with horizontal wavenumber  $k$  and propagating in the vertical plane which contains the mean vertical shear rate. The maximal vertical distance  $\Delta z$  this wave can travel in the shear flow before it reaches its critical level follows from integration of the refraction equation (2.5.22) giving:

$$k \cdot \Delta z \approx \pm \left[ 1 + \frac{N(z \pm \Delta z)}{N(z)} \right] \text{Ri}^{1/2}(z) . \quad (2.6.1)$$



In (2.6.1) is  $Ri(z)$  the gradient Richardson number (2.3.2),  $N(z)$  is the local buoyancy frequency defined in (2.3.2) and  $z$  is the initial starting point of the wave. Equation (2.6.1) shows that waves with sufficiently small horizontal wavelengths are trapped in a layer with thickness  $2|\Delta z|$ . This phenomenon is nicely demonstrated by the experiments of Koop (1981).

In addition, (2.6.1) shows the spreading of waves with different horizontal wavelengths across the waterdepth due to the presence of a mean shear. On the way to their respective critical levels these waves induce an increasing vertical shear rate ( $|\mathbf{m}| |\hat{\mathbf{u}}|$ ) and are damped by viscosity or by turbulence.

If the damping is not sufficient the internal waves will create instabilities at background  $Ri$ -numbers well above the maximal, critical value of the mean flow. In this respect there are two possible causes for wave breaking:

- convectional overturning due to an instantaneous unstable density gradient, i.e.  $\partial\rho/\partial z > 0$ , also called the gravitational Rayleigh-Taylor instability,
- hydrodynamic (Kelvin-Helmholtz) instability due to a local and temporal value of  $Ri(\underline{x}, t)$  below some critical value and this critical value has  $1/4$  as the upper limit from linear theory.

The tendency to form these critical levels with the magnitude of the vertical wavenumber growing to infinity seems to be the "fate" of internal gravity waves in shear flows, see Henney and Pomphrey (1983). Near the critical level the waves diminish i.e. the fluctuating energy is exchanged into an energy increase of the main flow and this conversion causes locally an acceleration of the flow. This momentum exchange mechanism is quite different from momentum diffusion by turbulence (Phillips, 1980).

Thus the shear-induced spreading of waves may transport fluctuating (wave-) energy to locations where turbulence production is diminished and turbulent diffusion is suppressed by stratification. Critical layer formation at these initially "quiet" turbulent levels may increase the vertical mixing in a flow with a background gradient Richardson number well above the one for instability of the mean flow. This assumption is investigated in this report.

Below, both types of instabilities are briefly discussed for monochromatic waves i.e. waves with spectral energy concentrated near one distinct wavenumber. We will show that both criteria give practically similar limitations on the following ratio between wave displacement amplitude and vertical wavelength

$$\mu = |\mathbf{m}| \hat{Z}, \quad (2.6.2)$$

with vertical wavenumber  $m$ .

#### Convectional overturning

Provided the mean density gradient is vertical the small wave-induced density fluctuation  $\tilde{\rho}$  follows from (2.4.7) and is written as:

$$\tilde{\rho} = -\hat{Z} \cos\Phi \left\langle \frac{\partial\rho}{\partial z} \right\rangle, \quad (2.6.3)$$



with time dependent phase  $\Phi(t)$  and the small magnitude  $\hat{Z}$  of the vertical wave-induced particle displacement. In absence of turbulence we can express the total density as  $\rho(\mathbf{x}, t) = \langle \rho \rangle + \tilde{\rho}$  and exploit (2.6.3) to derive the total, instantaneous vertical density gradient:

$$\frac{\partial \rho}{\partial z} = (1 - m \hat{Z} \sin \Phi) \left\langle \frac{\partial \rho}{\partial z} \right\rangle. \quad (2.6.4)$$

This vertical density gradient becomes positive and thus sensible to gravitational instability for  $(m \hat{Z} \sin \Phi) > 1$ . Orlanski (1972) found for the onset of gravitational instability of standing waves  $\mu \approx 0.64$ . He attributes the deviation from his theoretical value  $\mu \approx 0.74$  for his experiments to second order contributions to the vertical density gradient. Despite the neglect of the dynamics the criterion (2.6.4) appears to be appropriate for Orlanski's experiments.

The experimental value of  $\mu = 0.64$  implies that the vertical displacement amplitude is about 10% of the vertical wavelength. Another way of presenting the same result is to compute the rms value of the fluctuating slope of density isolines, it simply yields:

$$\left| \frac{\partial \tilde{Z}}{\partial z} \right| = \frac{\mu}{\sqrt{2}} \leq 0.45 \quad ; \quad \mu \leq 0.64. \quad (2.6.5)$$

In Chapter 3 we will return to this ratio when we consider density fluctuations and vertical density gradients related to vertical wavenumber spectra.

#### Kelvin-Helmholtz instability superimposed on an internal gravity wave

In view of Section 2.7 where we summarized the theory of wave-wave interactions and the importance of long waves straining smaller ones we may define the instantaneous (gradient) Richardson number  $\tilde{Ri}(\mathbf{x}, t)$  as:

$$\tilde{Ri}(\mathbf{x}, t) = - \frac{g}{S^2} \frac{\partial \rho}{\partial z}, \quad (2.6.6)$$

with the vertical shear rate  $S(\mathbf{x}, t)$  of the horizontal velocity including the contribution from internal waves. In the following we consider a monochromatic wave and we assume the mean shear rate is maximal in the x-z plane so that  $\langle S \rangle = \partial U / \partial z$ . For internal waves in the plane of maximal mean shear rate the Richardson number is smallest (Squire's theorem) and then (2.6.5) yields:

$$\tilde{Ri}(\mathbf{x}, t) = \frac{1 - \mu \sin \Phi}{(Fr + \mu \sin \Theta \cos \Phi)^2} \quad ; \quad Fr = Ri^{-1/2}. \quad (2.6.7)$$

In this equation we conveniently applied the so-called internal Froude number  $Fr$  instead of the gradient Richardson number  $Ri$  given in (2.3.2). In absence of a mean shear rate ( $Fr = 0$ ) and with  $\mu > 1$  we conclude from (2.6.7) that  $\tilde{Ri} < 0$  for a certain range of the phase  $\Phi$ . The addition of shear ( $Fr > 0$ ) will further reduce  $\tilde{Ri}$  if it is positive. The growth of the Kelvin-Helmholtz instability, now considered to occur superimposed on the wave-induced flow, is usually much faster than the period of the internal gravity wave. Hence, the instability may grow as if the flow was steady. The possible occurrence of the Kelvin-Helmholtz instability in a flow with an extended bandwidth of internal waves is indicated by the photograph (Koop and McGee, 1986, Fig. 9).

The criterion of shear instability (2.6.7) shows that the upper limit of  $\mu$  decreases with decreasing mean Richardson number  $Ri$  and that  $\bar{Ri}$  is minimal for  $\Theta=90^\circ$ . This results implies that with decreasing mean Richardson number  $Ri$ , first the internal waves with most of their kinetic energy stored in the horizontal motions will break, for example an internal gravity waves approaching the level of critical layer formation, see Fritts (1976, eq. 8 and fig. 5) who applied (2.6.7) for wave breaking near a critical level.

#### Criterion to estimate the upper limit for IWE

In terms of  $\mu$  the criterion for convectional overturning and for hydrodynamic instability is practically equal and the maximal value for the upper limit of  $\mu$  in (2.6.2) before convectional overturning will occur or before  $\bar{Ri} < 0$  reads:

$$\mu = |\mathbf{m}| \hat{Z} \leq 1. \quad (2.6.8)$$

Actually, the criterion (2.6.8) is only valid for an internal gravity wave with spectral energy concentrated near one distinct wavenumber. An extension of this idealized picture may be a "rarefied field" of waves i.e. a large water volume in which one solitary group of waves with a certain wavenumber vector passes our point of observation and in due time, without overlapping the previous group, the next group with possibly another wavenumber vector may follow. Here a wave group is thought of having a size of a few wavelengths. The musical analogy may be a melody consisting of a series of tones possibly with silent intervals in between and each tone short but distinct enough to observe its pitch.

The alternative is that groups of internal gravity waves with different origins of creation and with different wavenumber vectors appear at the same time in our point of observation. The musical analogy may be a chord. For the latter spectrum of internal waves the general criterion for gravitational or hydrodynamic instability must be replaced by

$$\left| \frac{\partial \bar{\rho}}{\partial z} \right| = \alpha \left| \left\langle \frac{\partial \rho}{\partial z} \right\rangle \right|, \quad (2.6.9)$$

with  $\left| \frac{\partial \bar{\rho}}{\partial z} \right| = \left\langle \left( \frac{\partial \bar{\rho}}{\partial z} \right)^2 \right\rangle^{1/2}$  and  $\alpha \leq 1/2$  in view of (2.6.5).

The value of  $\alpha$  depends on the probability distribution of the instantaneous vertical density gradient and the allowed level of exceedence. We have indicated our expectation of the upper limit for  $\alpha$  based on (2.6.5) derived from Orlanski's experiments. In Chapter 3 we will investigate the limitations imposed by criterion (2.6.9) on the kinetic energy of a spectrum of internal waves.

#### Wavenumber dependence of the spectral energy density of IWE

From observations (CTD drops) we can derived the spectrum of vertical displacement of fluid parcels as a function of vertical wavenumber  $m$ . Here aliasing occurs of spectral energy density belonging to different wavenumber vectors  $\mathbf{k}$  but with the same vertical wavenumber component  $m$ . Actually, this aliasing implies the application of a high-pass filter on the 3D-spectral energy density  $\hat{\Pi}_Z(\mathbf{k})$  of wave-induced displacements and provides the 1D-spectral energy density  $\tilde{E}_Z(m)$  depending on the vertical wavenumber:

$$\langle \tilde{Z}^2 \rangle_m = \int_m^\infty \left( \int_0^\infty \int_0^\infty \hat{\Pi}_Z(\mathbf{k}, \ell, \mu) d\mathbf{k} d\ell \right) d\mu = \int_m^\infty \tilde{E}_Z(\mu) d\mu. \quad (2.6.10)$$



In view of the preceding arguments on the upper limit of  $\mu$  we may postulate the dependence:

$$\langle \tilde{Z}^2 \rangle |_{\mathbf{m}} \propto \mathbf{m}^{-2} \quad (2.6.11)$$

Differentiation of (2.6.11) and (2.6.10) with respect to  $\mathbf{m}$  provides the following shape of the 1D-spectral energy density of vertical displacements:

$$\tilde{E}_Z(\mathbf{m}) = c \mathbf{m}^{-3} . \quad (2.6.12)$$

CTD drops in the ocean exhibit the  $\mathbf{m}^{-3}$  shape of the energy density field at an intermediate range of vertical wavenumbers, the so-called buoyancy subrange, see e.g. (Gargett et al., 1981) and the subsequent transition at larger wavenumbers towards the inertial subrange of unstratified turbulence (Gargett et al., 1984).

Alternatively, more elaborate theoretical arguments have been presented by Lumley (1964), Weinstock (1978), Bolzano (1959). These authors suggest powers of  $\mathbf{m}$  which are slightly different from -3. However, field observations in the atmosphere as well as in the ocean are not precise enough to select between these proposals. Hence, we will rely on (2.6.12).

#### Variance of the wave-induced strain rate

Below we will derive the ensemble-averaged square of the wave-induced strain rate. This provides an additional straining of the turbulence and thus turbulence production.

According to (2.2.23) the mean square  $\langle \tilde{\gamma}^2 \rangle$  of the sum of all the wave-induced strain rates reads

$$\langle \tilde{\gamma}^2 \rangle = \langle \tilde{\underline{\underline{d}}} : \tilde{\underline{\underline{d}}} \rangle = \tilde{\eta}^2 - \tilde{\nabla} \cdot \langle \tilde{\underline{\underline{T}}} \rangle ; \quad \tilde{\eta}^2 = \frac{1}{2} \langle \tilde{\underline{\underline{\omega}}} \cdot \tilde{\underline{\underline{\omega}}} \rangle . \quad (2.6.13)$$

In (2.6.13) is  $\tilde{\eta}^2 = \frac{1}{2} \langle \tilde{\underline{\underline{\omega}}} \cdot \tilde{\underline{\underline{\omega}}} \rangle$  the internal-wave enstrophy. It is expressed into the variance  $\langle \tilde{Z}^2 \rangle$  of the wave-induced vertical displacement as follows. The wave-induced rotation  $\tilde{\underline{\underline{\omega}}}$  is decomposed into

$$\tilde{\underline{\underline{\omega}}} = \tilde{\underline{\underline{\omega}}} \cdot \exp[i(\mathbf{k}\mathbf{x} + \ell\mathbf{y} - \omega t)] . \quad (2.6.14)$$

Thus we can express the Cartesian components of the complex-valued amplitude  $\tilde{\underline{\underline{\omega}}}$  as:

$$\tilde{\omega}_x = i\ell\tilde{\omega} - \frac{d\tilde{\omega}}{dz} ; \quad \tilde{\omega}_y = \frac{d\tilde{\omega}}{dz} - ik\tilde{\omega} ; \quad \tilde{\omega}_z = i(k\tilde{\omega} - \ell\hat{u}) . \quad (2.6.15)$$

Substitution of (2.4.16) into (2.6.15) yields:

$$\tilde{\omega}_x = \frac{\ell\hat{Z}N^2}{k(U-c)} - \frac{k\ell}{k^2 + \ell^2} \frac{d\hat{Z}}{dz} \frac{dU}{dz} , \quad (2.6.16a)$$

$$\tilde{\omega}_y = \frac{k\hat{Z}N^2}{k(U-c)} - \hat{Z} \frac{d^2U}{dz^2} - \frac{\ell^2}{k^2 + \ell^2} \frac{d\hat{Z}}{dz} \frac{dU}{dz} , \quad (2.6.16b)$$

$$\tilde{\omega}_z = i\ell\hat{Z} \frac{dU}{dz} . \quad (2.6.16c)$$

The appearance of the wave-induced vertical vorticity component  $\hat{\omega}_z$  in (2.6.16c) is due to the shear rate of the main flow and is nonzero for waves which travel out of the flow plane  $\ell \neq 0$ . Incidentally, this vertical vorticity component of internal waves in a shear flow makes the Craya decomposition (2.5.12) of motions into internal waves and quasi two-dimensional turbulence inappropriate.

To compute the wave-induced enstrophy we simplify the expressions (2.6.16) for waves which are practically steady so that  $c$  is real-valued. Further, we apply the dispersion relation (2.5.8) instead of the exact one (2.5.7) and thus neglect the curvature of the vertical profile of the mean streamwise velocity. In addition, we apply the WKB expansion so that holds  $\mathbf{m} = d\hat{\mathbf{z}}/dz$ , see also (2.4.9) and (2.4.10). Finally, for slow spatial and temporal variations of IWE the divergence of the mean wave force,  $\vec{\nabla} \cdot \langle \hat{\mathbf{T}} \rangle$ , is negligible.

Thus the variance of the wave-induced strain rate is approximated by:

$$\langle \tilde{\gamma}^2 \rangle \approx \frac{1}{2} |\mathbf{k}|^2 N^2 \langle \tilde{z}^2 \rangle \left( 1 + \frac{\sin^2 \phi}{\text{Ri}} \right); \quad \sin \phi = \frac{\ell}{(k^2 + \ell^2)^{1/2}}. \quad (2.6.17)$$

From (2.6.17) we learn that internal waves travelling perpendicular to the vertical plane which contains the mean shear flow enhance the variance of their strain rates. Further, from critical layer formation follows that  $\langle \tilde{\gamma}^2 \rangle$  increases proportional to  $|\mathbf{m}|$ , provided the magnitude of the vertical wavenumber  $m$  largely exceeds the horizontal wavenumber components. Consequently, the wave-induced strain rate becomes large near a critical layer. The converse occurs near a caustic where the variance of the strain rate is minimal.

## 2.7 Waves with large amplitude and wave-wave interactions

As we announced in the introduction to this Chapter 2 we will exploit linearized wave theory as much as possible to diagnose our field observations in Chapter 4. Yet we must be aware of several nonlinear effects and verify whether these may explain for possible deficiencies in our analysis. Therefore, this section presents a conceptual basis for the formation of continuous wave spectra and the possible tendency of the wave patterns to create isotropy random fluctuations.

We could have shortened the title of this section into "nonlinearity". However, this term is not uniquely interpreted by everybody. For instance, some wave-wave interaction theories apply essentially linear wave theory. Or a monochromatic wave, with a large amplitude, does not produce a convection term  $(\mathbf{u} \cdot \vec{\nabla})\mathbf{u}$  nor an advection term  $(\mathbf{u} \cdot \vec{\nabla})\rho$  but that does not imply linear theory either. In particular this last example of large amplitude waves introduces the problem of a proper decomposition of the flow into waves and mean flow. The waves may invoke a so-called Stokes drift which is a wave property, second order in amplitude. Consequently, the orbital motions only have a zero mean value if these motions are superimposed on a mean flow being the sum of Eulerian and Stokes contributions. Actually, this formulation is the basis of the elegant theory of Generalized Lagrangian Mean (GLM) by Andrews and McIntyre (1978a, 1978b). In this GLM theory the mean is the sum of Eulerian mean and the Stokes drift terms. The momentum equations in terms of GLM allow for a proper description of wave force (2.2.6) even if the first-order wave theory is applicable. However, we will not go into details here but continue with a criterion for "large amplitude".



A criterion for large amplitude of internal waves may read as follows. Using (2.6.10) we define the mean square wave-induced vertical displacement  $|\tilde{Z}(\lambda_z)|$  spatially high-pass filtered at vertical wavelength  $\lambda_z$ . Upon using the particular choice of spectrum (2.6.12) the criterion for a large amplitude then yields:

$$\frac{|\tilde{Z}(\lambda_z)|}{\lambda_z} = \frac{1}{2\pi} \sqrt{\frac{1}{2}c} . \quad (2.7.1)$$

For small enough  $c$  so that (2.7.1) yields a ratio of a few % we will conclude the wave-spectrum describes small-amplitude waves.

Next, we continue below with a brief description of wave-wave interactions. The interactions can be of the resonant type where two or more waves interact so that another wave is excited in its natural intrinsic frequency similar to a weakly damped mechanical mass-spring-damper system excited in its resonance frequency. In this case the sum or difference of all interacting waves equals zero. However, if this sum deviates significantly from zero a forced wave mode is excited and this is the off-resonance condition: the frequency imposed on this forced wave mode does not match the dispersion relation for a solitary wave.

The ratio (2.7.1) also plays a role in determining whether the wave field consists of interacting free internal waves or that the interactions are so strong that non-resonant (forced) wave modes are significantly produced. Phillips (1980, p. 196) introduces the neglect of non-resonant modes if

$$[m^3 \tilde{E}_Z(m)]^{1/2} \ll 1 . \quad (2.7.2)$$

is satisfied, however, how small the  $\ll$  sign invokes is left unspecified. Substitution of (2.6.12) immediately results into the equivalent statement of a small ratio (2.7.1).

### *Three interacting internal waves in one vertical plane*

The opposite of the rather vague criterion (2.7.2) for the dominance of internal waves over non-resonant components in a broad-banded spectrum is to derive arguments from the analytical theory on the interaction between three internal gravity waves. A complete description, if it exist, is not possible in this study.

Instead, we are mainly interested in the rate of energy exchange between interacting waves, to what extent linear theory is still applicable and what we may expect from interacting waves in a tidal shear flow.

For this purpose we analyze and summarize below the exact, nonlinear study of (Ripa, 1981) for three waves in an infinitely extended and uniform flow with arbitrary amplitudes and with orbital motions in one vertical  $x$ - $z$  plane. The latter restriction reduces the problem to two dimensions and thus enables the introduction of a complex-valued stream function  $\psi(x,z,t)$  for an incompressible flow. In addition, the density variations are related to a Lagrangian vertical coordinate  $\tilde{Z}(t;x,z)$  with  $(x,z)$  the reference equilibrium position. Hence,

$$\tilde{u} = -\text{Re}\left(\frac{\partial \psi}{\partial z}\right) ; \tilde{w} = \text{Re}\left(\frac{\partial \psi}{\partial x}\right) ; \frac{\rho}{\rho_0} = 1 + \frac{N^2}{g}(\tilde{Z} - z) . \quad (2.7.3)$$

In (2.7.3) is  $\rho_0$  a constant reference density and  $N$  the constant buoyancy frequency. Taking the curl of the Euler equations for  $u$  and for  $w$  produces the Helmholtz equation for the transverse vorticity component  $\tilde{\omega}_y = -\nabla^2 \psi$ .

Further, mass conservation, with  $\rho$  defined by (2.7.3), simply yields the definition of the vertical velocity. The two relevant equations for transverse vorticity and for density now read:

$$\frac{D \nabla^2 \psi}{Dt} + N^2 \frac{\partial \tilde{Z}}{\partial x} = 0 ; \quad \frac{D \tilde{Z}}{Dt} - \frac{\partial \psi}{\partial x} = 0 \quad \text{with} \quad \frac{D}{Dt} \equiv \frac{\partial}{\partial t} + \tilde{u} \frac{\partial}{\partial x} + \tilde{w} \frac{\partial}{\partial z} . \quad (2.7.4)$$

These equations are reformulated in the following two steps. Firstly, we will formulate the solution to the linearized and homogeneous versions of (2.7.4) with constant amplitude  $\zeta_0$ . Secondly, this solution is substituted into the original equations (2.7.4) but now with a time-dependent complex-valued amplitude  $\zeta(t)$ . In the second step the quadratic terms are located in the RHS of the linearized equations.

Each plane internal wave is defined at a constant wavenumber vector  $\underline{k}$  and for the first step we write:

$$\psi = \zeta_0 \exp(i \underline{k} \cdot \underline{x} - i \Omega t) ; \quad \tilde{Z} = c_z \text{Re}(\psi) ; \quad \frac{\Omega}{N} = \frac{k}{|\underline{k}|} ; \quad \underline{k} = (k, 0, m) . \quad (2.7.5)$$

Here we allow  $\Omega$  to become negative, however, this creates the sign-ambiguity of the phase velocity which has been avoided in the previous sections. In (2.7.5) we anticipated the linear solution of internal waves in the x-z plane and in an infinitely extended fluid with zero mean velocity. Substitution of (2.7.5) into the linearized version of (2.7.4) yields:

$$c_z = -\frac{K}{N} , \quad \text{with} \quad K = \text{sign}(k) |\underline{k}| . \quad (2.7.6)$$

Later it will become evident that the proper definition of total energy E reads:

$$E = \frac{1}{2} \langle \tilde{u}^2 \rangle + \frac{1}{2} \langle \tilde{w}^2 \rangle + \frac{1}{2} N^2 \langle \tilde{Z}^2 \rangle . \quad (2.7.7)$$

With the expression (2.7.6) for  $c_z$  there is equipartitioning between potential and kinetic energy. The ensemble averaging operation is now replaced by averaging along the x-direction due to spatial homogeneity in the x-direction. This completes the first step using the homogeneous linearized version of (2.7.4).

Ripa defines three internal waves "a", "b" and "c" and the variables belonging to it obtain the subscripts a, b or c. Each wave possesses a fixed wavenumber vector. This point of view differs from our deductions from the Taylor Goldstein equation where the vertical wavenumber was flow dependent. In the present case the wavenumber remains fixed and the nonlinearities are notable as temporal changes in the magnitude as well as in the phase of the complex-valued amplitude  $\zeta(t)$ .

If waves "b" and "c" are substituted into the quadratic terms then, obviously, they excite wave "a" with wavenumber  $\underline{k}_a$  that satisfies the following necessary condition for interaction:

$$\underline{k}_a + \underline{k}_b + \underline{k}_c = \underline{0} . \quad (2.7.8)$$

This requirement creates a triangle in wavenumber space with the base of one wavenumber positioned at the end of another wavenumber. Instead of the usual definition of  $\theta$  in the interval  $[\frac{1}{2}\pi, \frac{3}{2}\pi]$ , thus keeping  $\cos\theta \geq 0$ , it will be advantageous to define the accompanying angles  $\theta$  on the interval  $[0, 2\pi]$ , see Fig. 2.7.1. These angles are measured anticlockwise from the positive x-direction to the direction of the relevant wavenumber vector.



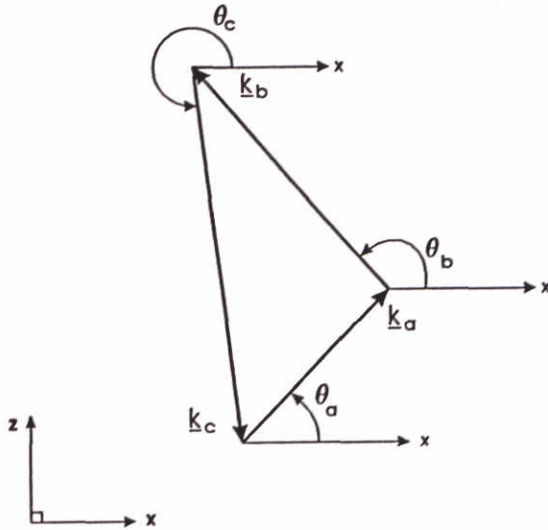


Fig. 2.7.1. Triangle of wavenumbers and angles of three interacting waves.

As a preparation to the second step we define the time-dependent complex-valued amplitude  $\zeta_a(t)$  for wave "a" as:

$$E_a(t) = \text{def} = \zeta_a(t) \zeta_a^*(t) ; \quad \zeta_{0_a} \rightarrow \zeta_{0_a}(t) = \text{def} = \frac{\sqrt{2}}{K_a} \zeta_a(t) \quad (2.7.9)$$

and likewise for waves "b" and "c". In (2.7.9) we have used  $\zeta^+$  as the complex conjugate of  $\zeta$  instead of the superscript "cc" to avoid ambiguity with the wave indicator.

In the following second step we substitute for each wave "a", "b" and "c" the time-dependent amplitude  $\zeta_0$  into (2.7.5). The result is substituted into the nonlinear equations (2.7.4). These nonlinear equations are written as the linearized version with the quadratic terms in the RHS and this finally yields:

$$\frac{d\zeta_a}{dt} + i\Omega_a \zeta_a = \sigma_a^{bc} \zeta_b^* \zeta_c^* , \quad (2.7.10)$$

with interaction coefficient

$$\sigma_a^{bc} = c_{abc} (K_b - K_c) ; \quad c_{abc} = \sqrt{2} \sin[\frac{1}{2}(\theta_a - \theta_b)] \sin[\frac{1}{2}(\theta_b - \theta_c)] \sin[\frac{1}{2}(\theta_c - \theta_a)] . \quad (2.7.11)$$

Cyclic permutation in the set (a,b,c) provides the interaction coefficients for the evolution equation (2.7.10) for wave "b" or "c". However, the coefficient  $c_{abc}$  is a property of the triad rather than of a particular wave within the triad.

After substitution of (2.7.5) into (2.7.4) the interaction coefficient (2.7.11) follows from geometrical arguments of the mutual relation between angles and wavenumber components that satisfy (2.7.8) and they are indicated in Fig. 2.7.1. The invariance of the coefficient  $c_{abc}$  for a particular wave of the triad is used to readily derive the following essential properties of the interaction coefficients:

$$\sigma_a^{bc} + \sigma_b^{ca} + \sigma_c^{ab} = 0 ; \quad K_a \sigma_a^{bc} + K_b \sigma_b^{ca} + K_c \sigma_c^{ab} = 0 . \quad (2.7.12)$$

These properties will yield the conservation of total energy and of total pseudo-momentum. Later we will need the interaction coefficient with largest magnitude. The first equation in (2.7.12) implies that, for a given triad, one of the three coefficients has a sign opposite to that of the other two, and consequently is the largest in absolute value. The second equation in (2.7.12) implies that the wave with the largest absolute value of its interaction coefficient is the one with the intermediate value of  $K_i = \text{sign}(k_i) |k_i|$  ( $i=a,b,c$ ). Therefore we conveniently order the participants in the triad so that "b" has the intermediate value for  $K_b$  and consequently the largest magnitude of the interaction coefficients involved:

$$|\sigma_a^{ca}| \geq \sigma_a^{bc} \text{ and } |\sigma_b^{ca}| \geq \sigma_c^{ab} \text{ if } K_c \leq K_b \leq K_a \quad (2.7.13)$$

Of importance for energy exchange in the triad is the occurrence of phase locking among the waves. This phase locking is represented by means of angle  $\delta(t)$  as the sum of the phases of the three waves:

$$\delta(t) = \text{def} = \arg \zeta_a + \arg \zeta_b + \arg \zeta_c ; \zeta = |\zeta| \exp(i \arg \zeta) . \quad (2.7.14)$$

In (2.7.10) is the radian frequency  $\Omega_a$  a parameter rather than the actual intrinsic frequency  $\Omega'_a$  of wave "a". Ripa defines and connects the latter to the temporal derivative of the phase of the complex-valued amplitude given in (2.7.14). However, this definition is disputable if the frequency perturbations are of the same order of magnitude as the radian frequency  $\Omega_a$ . Then we may better interpret these perturbations as rapid amplitude modulations. Substitution of  $\zeta_a = |\zeta_a| \exp(i \arg \zeta_a)$  into (2.7.10) while considering the imaginary part of this equation yields:

$$\Omega'_a = - \frac{d \arg \zeta_a}{dt} = \Omega_a - \sigma_a^{bc} \left( \frac{E_b E_c}{E_a} \right)^{1/2} \sin \delta(t) . \quad (2.7.15)$$

This equation immediately reveals that if the energy of wave "a" is much larger than the remaining "perturbing" modes then the actual intrinsic frequency of the most energetic wave "a" in the triad equals the frequency of a solitary wave with wavenumber  $k_a$ .

The ordinary differential equation for the fluctuating energy, which is defined by (2.7.9), of one wave mode is obtained as follows. Equation (2.7.10) is multiplied by  $\zeta_a^*$  and added to this the complex conjugate of (2.7.10) multiplied with  $\zeta$ . The result reads:

$$\frac{dE_a}{dt} = 2 \sigma_a^{bc} (E_a E_b E_c)^{1/2} \cos \delta(t) . \quad (2.7.16)$$

An alternative expression follows from (2.7.16) through scaling the energy with the interaction coefficient belonging to it:

$$\frac{dA_a}{dt} \equiv \frac{dA_b}{dt} \equiv \frac{dA_c}{dt} \equiv 2 (\sigma_a^{bc} \sigma_b^{ca} \sigma_c^{ab})^{1/2} (A_a A_b A_c)^{1/2} \cos \delta(t) ; A_a = \text{def} = \frac{E_a}{\sigma_a^{bc}} \text{ etc.} \quad (2.7.17)$$

An indication of the time-dependence of the phase locking angle  $\delta$  follows from considering the temporal integral of the imaginary part of the sum

$$\zeta_a \zeta_b \frac{d\zeta_c}{dt} + \zeta_b \zeta_c \frac{d\zeta_a}{dt} + \zeta_c \zeta_a \frac{d\zeta_b}{dt} \text{ which yields:} \\ (E_a E_b E_c)^{1/2} \sin \delta(t) + \Omega A_a = \text{constant} ; \Omega = \Omega_a + \Omega_b + \Omega_c . \quad (2.7.18)$$



If we consider the square of (2.7.17), eliminate  $\cos^2(\delta)$  from it by means of (2.7.18) and if we put  $A_i = a_i + J(t)$  ( $i = a, b, c$ ) then we obtain a third order polynomial in  $J(t)$  for the  $(dJ/dt)^2$ . The solution for  $J(t)$  can be expressed into Jacobian elliptic functions, but we will not pursue this here and refer to the appendix in (Ripa, 1981). Instead, we prefer to continue with more general properties for wave-wave interactions in one vertical plane.

$$E = E_a + E_b + E_c \equiv \text{constant}; \quad P = \frac{K_a}{N} E_a + \frac{K_b}{N} E_b + \frac{K_c}{N} E_c \equiv \text{constant} \quad (2.7.19)$$

2 - 33

The conservation of total energy demands that the energy state of the triad ( $E_a, E_b, E_c$ ) lies in the plane  $E = \text{constant}$ . In addition, the conservation of pseudo-momentum restricts the possible energy state to a line (A B in Fig. 2.7.2) being the intersection of the planes  $E = \text{constant}$  and  $P = \text{constant}$ . Conditions (2.7.19) show that the mode with the largest wavelength suffers the least perturbations in its energy level, for instance mode "c" in Fig. 2.7.2. An interesting application is to consider one vertical Fourier mode of a mean flow with infinite horizontal wavelength, we shall consider this later. First we analyze the general energy transfer between the modes.

In addition to the restrictions (2.7.19), the expression (2.7.18) reduces the admissible variations in energy levels even more. We will investigate the implication of (2.7.17) as follows. Suppose the following condition is satisfied:

$$\Omega = \Omega_a + \Omega_b + \Omega_c = 0 \quad (2.7.20)$$

The convenience of allowing the intrinsic radian frequencies, defined in (2.7.5), to become negative becomes obvious now. It will not be immediately apparent that the necessary interaction condition (2.7.8) and the condition (2.7.20) posses a solution, however, it can be shown that for two as well three dimensions this is indeed the case. The condition (2.7.20) creates resonance because the sum or the difference of the natural frequencies of two waves excites the third one in its natural frequency.

Next, we continue with the assumption that (2.7.20) holds for a particular triad and in addition we assume  $\delta = n\pi$  ( $n=0,1,2,\dots$ ) at a given time. Then the constant in (2.7.18) is zero and  $\delta$  must remain ( $n\pi$ ) for all times. According to (2.7.15) the intrinsic frequencies are unaltered i.e. as if the waves were solitary. Moreover  $\delta = n\pi$  creates a perfect phase lock between the interacting waves.

A significantly less restrictive condition is to satisfy (2.7.20) but  $\delta \neq n\pi$  ( $n=0,1,2,\dots$ ). Consequently,  $\sin(\delta)$  cannot change sign and this restricts  $\delta$  exclusively in the interval  $(0, \pi)$  or  $(\pi, 2\pi)$ .

According to (2.7.15) the actual radian frequencies remain below or above their natural ones for solitary waves. Yet the sign of the energy transfer, described by (2.7.16), may oscillate. Indeed the analytical solutions to (2.7.10) show this behaviour: a part of the total energy is flowing from one wave mode to the others and vice versa. Therefore, the condition (2.7.20) is called "resonant interaction" because two waves excite the third one in its natural intrinsic frequency with its wavenumber satisfying the dispersion relation (2.7.8).

The so-called off-resonance condition holds if (2.7.20) is not fulfilled and Ripa introduces the following measure for "detuning" of the resonance condition:

$$\Omega' = \frac{\Omega}{2\mu_0} \quad ; \quad \left(\frac{3}{4}\right)^{1/4} |\sigma_a^{bc} \sigma_c^{ab}| E \leq \mu_0^2 \leq (\sigma_b^{ca})^2 E \quad (2.7.21)$$

In (2.7.21) we have used the ordering in (2.7.13) to define the largest absolute value of the interaction coefficient. According to (Ripa, 1981, eq. (5.24)), for  $\Omega' \geq 1$  effectively the off-resonance condition holds. The larger the ratio in (2.7.21) the faster  $\sin(\delta)$  and  $\cos(\delta)$  oscillate and the more the energy transfer between the modes is prohibited. Nevertheless, if the energy levels are large enough these off-resonance waves are excited and this tends to create a more continuously filled energy density spectrum.



Vaguely speaking the "mean intrinsic frequency"  $\Omega'_i$  ( $i=a,b,c$ ), given by (2.7.15), of the off-resonant waves remain as if the waves were solitary but their instantaneous frequencies are shifted by an amount of  $O(\mu_0)$  (Ripa, 1981, p. 111). With increasing total energy  $E$  and/or increasing wavenumber differences  $|K_a - K_c|$  the near-resonance condition  $\Omega' < 1$  is achieved for a larger "volume" in wavenumber space. By "volume" we mean here the set of points  $P$  in Fig. 2.7.1 with fixed  $k_a$ . In the weak resonance theory this set is only one point for which exactly holds  $\Omega' = 0$ .

Moreover, for  $\Omega' < 1$  the energy transfer between at least two waves in a triad approaches the effectiveness of this transfer at resonance. In other words, for growing energy levels, so that  $\Omega' < 1$  is achieved in a larger "volume" of wavenumber space, the energy transfer between waves may be large enough to create a notable energy cascade.

We rewrite the evolution equation (2.7.16) for the energy per wave mode to gain more insight in the rate of its energy transfer and the mechanism controlling this transfer. For this purpose we keep in mind the ordering given in (2.7.13) and we assume the temporal mean of  $E_c$  is the largest one of the energies involved in the triad.

In addition, it is straightforward to express the ensemble-averaged square of the strain rate (2.6.13) for a wave with energy at one distinct wavelength into  $K$  and  $E$  as:

$$\langle \tilde{\gamma}^2 \rangle = \langle \tilde{d} : \tilde{d} \rangle = K^2 E . \quad (2.7.22)$$

Using the first expression in (2.7.11) for the interaction coefficient we can rewrite (2.7.16) readily into the following nondimensional form for the relative energy changes of wave "b":

$$\frac{1}{E_b} \frac{dE_b}{d\Omega_b t} = \frac{2c_{abc}}{\cos\theta_b} \left( \frac{K_a}{K_c} - 1 \right) \left( \frac{E_a}{E_b} \right)^{1/2} Fr_\gamma^{(c)} \cos\delta(t) ; \quad Fr_\gamma^{(c)} \equiv \frac{|\tilde{\gamma}_c|}{N} . \quad (2.7.23)$$

This equation now presents the relative change in energy of wave  $b$  per radian in the phase of this wave. This change in energy depends on the strain-rate Froude number  $Fr_\gamma$  which uses the rms strain rate of the most energetic wave "c". The energy of wave "b" changes in proportion to the rms strain rate imposed by the most energetic wave and nearly proportional to the "bandwidth"  $K_a/K_c$  provided this ratio largely exceeds unity. In virtue of the wavenumber triangle (2.7.8),  $K_b$  approaches  $K_a$  if the ratio  $K_a/K_c$  is much larger than unity. Thus the energy exchange between two short waves in a triad are amplified by the third long wave. Conversely, the energy level of the long wave will hardly be affected by short ones. Earlier we demonstrated this notion by means of the conservation laws for energy and for pseudo-momentum (2.7.19) and exemplified it in Fig. 2.7.2.

In Chapter 3 we will bluntly generalize this notion which is actually based on three interacting waves only. There we will assume the probability for breaking as a result of overly strong energy levels (saturation) is larger for short than for long waves in a spectrum of internal waves.

Moreover, from (2.7.23) we infer that for large enough wavenumbers the energy changes per cycle of the waves is too fast to classify them as "waves". On the other hand if the motions satisfy (2.7.10) then no mixing of mass occurs and thus the description as "turbulence" is neither appropriate.

### *Nonlinear interaction between two internal waves in a tidal shear flow*

Another important application of the presented exact and nonlinear theory is to regard the longest wave "c" as one of the Fourier modes of the tidal motion. This connection is somewhat hampered because we initially assumed an infinite fluid domain. However, we may avoid this requirement by the addition of symmetry or anti-symmetry planes as well as waves but we will not pursue this further.

Instead, we consider the particular wavenumber triangle in Fig. 2.7.3 with the wavenumber of wave "c" practically vertical. For convenience, we imagine a very long wave with horizontal group velocity in the positive x-direction and we let  $k > 0$  decrease to zero and then  $K_c$  is positive but  $\theta_c = \frac{1}{2}\pi$ . Thus wave "c" now represents a quasi-steady mode and the theory is now applicable to the interaction between two internal waves by the presence of a steady stratified shear flow.

By means of Fig. 2.7.3 we imagine that waves "a" and "b" possess a vertical wavelength being one order of magnitude smaller than the typical stratified layer thickness  $H$  and  $K_c = O(2\pi/H)$ . Obviously, for small enough gradient Richardson number, wave "c" is now the most energetic wave of all triads. Hence, triads formed with wave "c" are the most dominant ones for small enough  $Ri$ , although presently we do not know a mathematical criterion for this statement.

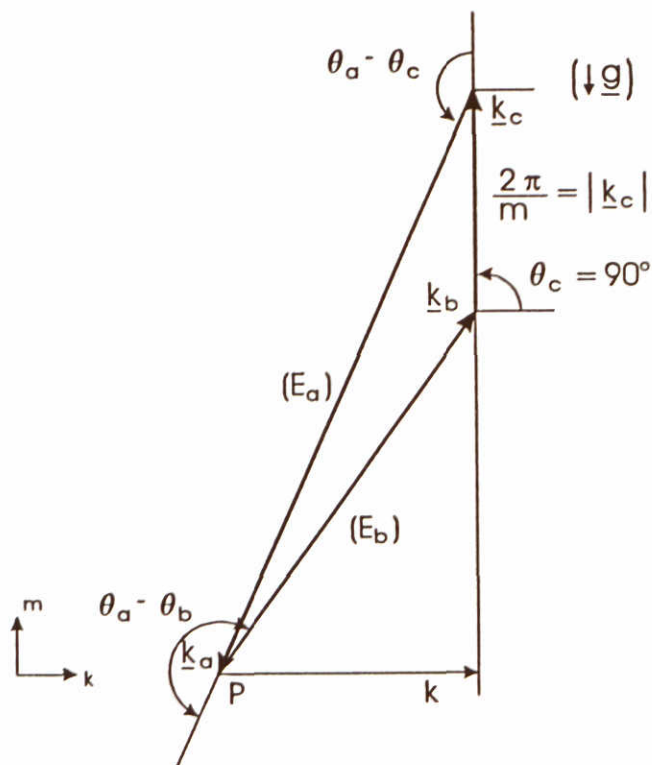


Fig. 2.7.3. Two shortwaves "a" and "b" interacting with mean flow component "c".

Based on these considerations and using (2.7.21) we can verify whether the interaction between waves "a" and "b" is of the near-resonance type i.e. whether  $\Omega' < 1$  holds. We find the following upper limit

$$\Omega' < \left( \frac{|K_c|}{2 |K_b|} Ri \right)^{1/2} \quad (2.7.24)$$



Thus for  $Ri \leq |2K_b/K_c|$ , which at least contains  $Ri \leq 2$ , the near-resonance condition is satisfied. Consequently, the energy perturbations given by (2.7.23) will include effective energy exchanges between waves "a" and "b" while leaving the energy of the wave "c" (mean flow) practically unaltered. Actually, a sequence of triads, similar to Fig. 2.7.3, can be constructed. This series of triads establish a "cascade" by which energy is transferred among internal waves at near-resonance condition and at equal horizontal wavenumber  $k$  but at different vertical wavenumbers  $m$ . This is an example of so-called induced diffusion of wave energy in wavenumber space by means of a long wave (McComas and Bretherton, 1977, Fig. 1a).

In Fig. 2.7.3 wave "b" has a group velocity oriented upwards and conversely wave "a" downwards. Thus the induced diffusion in the vertical plane containing the tidal shear flow induces waves at the same horizontal wavenumber with opposite signs in vertical momentum fluxes. The rate of energy exchange between wave modes is given by (2.7.23) and this rate is proportional to the Froude number of the tidal flow. Hence, with (2.7.23) we conjecture that also the net vertical momentum flux, averaged over many waves possessing the same horizontal wavenumber, are proportional to this Froude number. This argumentation yields the introduction of a wave-induced eddy viscosity, however, without mixing of mass.

This mechanism of shear-induced diffusion of wave energy may be one of the mechanisms to increase the turbulent Prandtl/Schmidt number as a function of gradient Richardson number. However, the level of wave energy plays a role in determining the wave-induced eddy viscosity and therefore we do not expect a universal damping function for  $\sigma_T$  defined in (2.3.4).

#### *Summary: contributions to a conceptual basis*

Prior to Ripa's study papers such as (McComas and Bretherton, 1977) and (Müller and Olbers, 1975) presented similar results, however, based on a 3D theory that assumed slow energy exchanges. In addition, Grimshaw (1988) applied nonlinear theory however limited to slow temporal and spatial changes of internal waves. He studied the energy exchange between three spatially limited wave groups. These groups pass through one volume at the same instant and each wave group possesses energy in one distinct wavenumber vector. Grimshaw found the same rules for mutual exchange of energy, of pseudo-momentum and of wave action were as described by, for instance, Ripa's theory. Instead, we preferred to summarize and analyze Ripa's 2D exact theory without the restrictions to slowness of energy exchange.

The analysis in this section is based on the study (Ripa, 1981), of a triad of internal waves is restricted to waves in a single vertical plane only whereas in reality a spectrum of waves in many vertical planes is expected. Nevertheless, this study creates a conceptual basis to interpret the field observations in terms of random internal waves in a stably-stratified shear flow.

For instance, the shorter the internal waves in a triad with a long wave become the more their properties as solitary waves are perturbed. However, the dispersion relation for solitary waves appears to hold "on the average" for off-resonance waves.

Hence, for large enough wavenumbers we anticipate a transitional bandwidth between 3D turbulence at much shorter wavelengths and a long-wavelength range with internal waves behaving more or less like an ensemble of solitary waves.



In this transitional bandwidth the wave-wave interactions are so strongly perturbed by waves with similar wavelengths as well as by longer waves that a decomposition into a set of solitary waves is no longer applicable. On the one hand, the ambiguous waves in this transitional bandwidth do not mix mass by their own action. On the other hand, the energy content of the waves may occasionally become so large that breaking occurs: then these waves have reached their saturation level. The wave breaking creates turbulence and consequently contribute to mixing of mass and of momentum.

Further, we base the following conclusion on three interacting waves in one vertical plane and in addition one wave that represents a stationary and spatially oscillatory flow. A stratified shear flow, with stratified layer thickness  $H$ , tends to homogenise the energy among upward and downward propagating internal waves with vertical wavelengths much shorter than  $H$  and horizontal wavelengths much larger than  $H$ . However, this a conclusion is limited to wave interaction in the vertical plane of the main flow.

Another contribution to a conceptual basis of criteria for wave breaking is the following. In a triad of interacting internal waves usually the shortest wave suffers the most energy variations. Equations (2.7.19) and the examples given made this clear. The intensity of the energy fluctuations of the shortest wave are controlled by the strain rate, actually the strain-rate Froude number, induced by the longer waves, see (2.7.23). Occasionally these energy fluctuations may exceed the "maximal" energy that can be stored in the internal wave at that particular wavenumber.

Although, the definition of maximal energy is a point of uncertainty as shown in the previous Section 2.6. Nevertheless, the point we want to make is the following when we consider wave breaking in a volume with random internal waves. We should integrate from the largest wavelength downwards to smaller wavelengths the ensemble-averaged strain rates induced by these waves and stop at some small wavelength where shear-rate-related instabilities will create wave breaking and produce turbulence.

This is in accordance with the intuitive notion that breaking of short waves will be promoted by the straining of the longer waves but not vice versa.

## 2.8 Review of observations of internal waves

### Observation of internal gravity waves in the field

Phillips (1980, Section 5.9, p. 252) reports "There is, perhaps, some uncertainty about the way in which energy is supplied to the internal wave field, not because of the lack of a suitable mechanism but rather because of a plethora of them".

Evidence of the occurrence of internal gravity waves in estuaries is given by e.g. West and Shiono (1985), New and Dyer (1988), Pietrzak et al. (1988) and Geyer (1987). They report different sources of production of internal gravity waves such as Kelvin-Helmholtz instabilities (Geyer, 1987), bottom topography (Pietrzak, 1988) or obstacles in the flow like bridge piles (New and Dyer, 1988).



In meteorology among others Kaimal et al. (1972), Finnigan and Einaudi (1981), Finnigan et al. (1984), Hunt et al. (1985), Finnigan (1987), Mobbs and Rees (1989) report the presence of waves in the lower atmosphere and the influence of these waves on turbulence. Other investigators, such as Townsend (1966), Carruthers and Hunt (1986), studied the loss of turbulent kinetic energy in the atmospheric boundary layer by excitation and subsequently radiation of internal gravity waves near the edge of a turbulent region.

#### **Observation of internal gravity waves in the laboratory**

In laboratory experiments on grid generated turbulence in a stratified fluid the decay of grid generated turbulence is reported to be less than under non-stratified conditions (Dickey and Mellor, 1981), (Stillinger et al., 1983a+b). This effect is attributed to the presence of waves. However, the picture is far from clear as noted by Itsweire et al. (1986).

Laboratory experiments on stratified shear flow have been reported by Pao (1973), Komori et al. (1983) and on the stably stratified mixing layer by Uittenbogaard (1988). As we will explain below, spectral analysis with respect to density and vertical velocity indicate the presence of internal gravity waves, following suggestions of Stewart, (1969). We considered some results of the stratified mixing layer experiments in (Uittenbogaard, 1993).

#### **Observation of internal gravity waves in numerical simulations**

Certain simple flow conditions allow for periodic continuation along computational boundaries and facilitate the application of fast pseudo-spectral solutions methods to solve the full Navier-Stokes equations. These so called Direct Numerical simulations (DNS) are actually limited to a Prandtl number of about unity so that the scales at which density variations dissipate are of the same order as the scale of velocity dissipation.

Flow geometries such as flows with a constant mean density gradients, a uniform or linear mean velocity profile or with more artificial symmetry conditions even a mixing layer have been computed with DNS. For instance, Riley, Metcalfe and Weissman (1981), Métais and Herring (1989), Staquet and Riley (1987) and many others.

Also with EDQNM, which is an accurate semi-analytical technique and a closure model, in 3D Fourier space Cambon (1989) the decay of homogeneous turbulence in a stratified fluid is analyzed.

These simulations, all based on 3D Fourier transforms, provide extensive data bases to analyze and to quantify the interactions between wave and quasi two-dimensional turbulence components (2.5.12).

#### **Quantification of Internal Wave Energy**

In all of the experimental researches known to us, the estimates of Internal Wave Energy (IWE) are only made if one distinct wave component dominates in the recordings of velocity, density, ground-pressure (atmospheric flow) or in the acoustic scattering images.

Pao (1973), Kaimal and Gaynor (1985) and Hunt et al. (1985) used quadrature-spectra (imaginary part of complex-valued cross spectra) derived from the vertical velocity and temperature or salinity to indicate the importance of internal waves vis. turbulence in the atmospheric boundary layer or in a laboratory channel flow. If waves dominate then these quadrature spectra are much larger than the coincidence spectra (real part of cross spectrum) hence a phase angle of  $\pm 90^\circ$  and usually a relatively large coherence. Hence, quadrature spectra and phase angles have been used as diagnostic tool to indicate internal waves, however, without further quantification.

The results of DNS and EQDNM simulations are split, mainly using Craya decomposition, into wave components and into two-dimensional turbulence components and thus a means of quantification is obtained. In particular the DNS of freely evolving turbulence in stably stratified fluids by Métais and Herring (1989) are of importance to our study. They also quantify length scales which are measurable in the field.

Surprisingly Gerz, Schumann, Elgobashi (1989) noted in their DNS of stably stratified shear flow the lack of a clear  $90^\circ$  phase angle between density and vertical velocity despite favourable stability conditions to create internal waves. These findings introduces quite a conceptual problem because this  $90^\circ$  phase angle was used as, and was found to be, an indicator of internal waves in experiments. Correspondingly, Yoon and Warhaft (1990) investigated experimentally, in grid generated temperature-stratified turbulence, the coherence and phase between density and vertical velocity fluctuations and conclude on p. 626:

"Presumably internal waves do exist since there is significant potential energy in the flow when the heat flux has collapsed but they are either masked by the active turbulence or, single-point measurements are insufficient to detect them".

This latter assertion may be valid because we assess that in DNS as well as in laboratory grid experiments a separation in terms of a bandwidth of internal waves and another one for turbulence is not achieved due to computer memory limitations or small flow facilities respectively. The next chapter will introduce such bandwidths and in Section 3.7 we will emphasise this assertion.



## 3 Some turbulence and internal wave estimators related to observations

### 3.1 Introduction

In this chapter we will exploit the theoretical considerations and the conceptual basis presented in Chapter 2 to formulate estimators for the state of internal waves and of turbulence. Appendices A provides additional details.

Section 3.2 is devoted to estimators for IWE and we do not comment on corrections for spurious platform motions (see Uittenbogaard (1993) for details on that matter).

Our considerations in Section 3.3 on saturation and the maximal energy contained in internal waves are new and they are directed to estimate the importance of internal waves for mixing. Saturation means that the wave field is so energetic that if more energy is fed into it an equal amount will be lost by wave breaking. Gibson (1981, 1986) obtained estimators for saturated internal wave spectra. Also Gibson (1981) successfully estimated the bandwidth in which the influence of buoyancy on the inertial turbulent motions is negligible. In Sections 3.3 and 3.4 we discuss the implications of Gibson's conclusions.

The estimators from microstructure observations are described by Ivey and Imberger (1991), and (CWR, 1993). We restrict ourselves to a brief introduction of the microstructure estimators derived from this technique. Some important dimensionless numbers for turbulence in stratified flows are repeated in Section 3.5 and the estimators for energy dissipation and for eddy diffusivity in Section 3.6. Apart from the mean density profiles all these turbulence state parameters may be derived from microstructure observations.

Section 3.7 contains an attempt to understand and to quantify the contradictory observations of internal waves in the laboratory, from DNS and in the field. We propose a dimensionless parameter that indicates the detectability of internal gravity waves and conclude that presently DNS is not able to compute a density stratified, turbulent flow at spatial scales large enough to observe internal waves and turbulence in non-overlapping bandwidth.

Finally, Section 3.8 is our attempt to formulate the energy transfer rate from internal waves to turbulence by critical layer formation and consequently wave breaking induced by the mean strain rate.

## 3.2 IWE estimators

Based on the theory presented in Chapter 2, our strategy to construct IWE estimators is as follows. First we express the kinetic IWE into mean flow variables and into the variance  $\langle \tilde{Z}^2 \rangle$  of the wave-induced vertical displacement. Under simplifications, which we will summarize below, the results yield

$$\frac{1}{2} \langle \tilde{\mathbf{u}} \cdot \tilde{\mathbf{u}} \rangle = \frac{1}{2} \langle \tilde{Z}^2 \rangle \left[ \frac{|\mathbf{k}|^2}{k^2 + \ell^2} \Omega^2 + \left( \frac{dU}{dz} \right)^2 \right]. \quad (2.4.31)$$

and this completes the first step. Next, we construct an upper limit and a lower limit spectral estimator for the variance  $\langle \tilde{Z}^2 \rangle$ ; these displacement estimators can be derived from our platform observations. Substitution into (2.4.31) provides the spectral energy density of the kinetic part of IWE.

We will assume:

- stationary or nearly stationary internal waves so that  $\beta = kc_i = 0$  holds in:

$$\hat{\mathbf{u}} \cdot \hat{\mathbf{u}}^{cc} = \frac{|\mathbf{k}|^2}{k^2 + \ell^2} (\beta^2 + \Omega^2) |\hat{Z}|^2 \left[ 1 + \left( \frac{1}{|\mathbf{k}| |\hat{Z}|} \frac{d|\hat{Z}|}{dz} \right)^2 \right] + \mathbf{k} \cdot \gamma |\hat{Z}|^2 \frac{dU}{dz} + |\hat{Z}|^2 \left( \frac{dU}{dz} \right)^2. \quad (2.4.30)$$

- The wave-induced displacement variance per wavenumber is spatially uniform or only weakly varying along the vertical.
- The vertical curvature of the streamwise velocity is small enough to neglect its contribution in the intrinsic angular frequency  $\Omega$  in (2.5.7) so that we apply (2.5.8).

Substitution of (2.5.8) into (2.4.31) yields our spectral energy density estimator for twice the Kinetic energy of IWE (KIWE):

$$\tilde{E}_u(\mathbf{k}) = \left[ N^2 + \left( \frac{dU}{dz} \right)^2 \right] \tilde{\Pi}_Z(\mathbf{k}), \quad (3.2.1)$$

where  $\tilde{E}_u(\mathbf{k}) \equiv \langle \tilde{\mathbf{u}} \cdot \tilde{\mathbf{u}} \rangle_{\mathbf{k}}$  and  $\tilde{\Pi}_Z(\mathbf{k}) \equiv \langle \tilde{Z}^2 \rangle_{\mathbf{k}}$ , the latter appeared before in (2.6.10).

By comparison, the mean of the fluctuating potential energy of the internal wave field at wavenumber  $\mathbf{k}$  is equal to  $\frac{1}{2} N^2 \langle \tilde{Z}^2 \rangle_{\mathbf{k}}$  and is unaffected by the mean shear rate. Hence, in Eulerian terms there is no equipartitioning between KIWE and potential IWE in a shear flow. However, cast in a Lagrangian framework the contribution of the mean shear rate in (3.2.1) disappears and then equipartitioning is recovered.

The estimator  $\tilde{E}(\mathbf{k})$  for the total IWE spectral energy density thus reads:

$$\tilde{E}(\mathbf{k}) = \left[ 2N^2 + \left( \frac{dU}{dz} \right)^2 \right] \tilde{\Pi}_Z(\mathbf{k}). \quad (3.2.2)$$

so that the total IWE becomes  $\frac{1}{2} \langle \tilde{\mathbf{u}} \cdot \tilde{\mathbf{u}} \rangle + \frac{1}{2} N^2 \langle \tilde{Z}^2 \rangle \equiv \frac{1}{2} \int \int \int \tilde{E}(\mathbf{k}) d\mathbf{k} d\ell d\mathbf{m}$ .

This completes the first step by which we have expressed IWE estimators into mean flow variables as well as into the 3D-energy density of wave-induced vertical displacement. Integration of (3.2.1) and of (3.2.2) over wavenumber space provides the KIWE and the total IWE respectively.



The second step is to construct estimators for the spectrum  $\tilde{\Pi}_z(\mathbf{k})$  defined in (3.2.1). The first estimator for this spectrum is closely related to the definition of the Ellison scale. This estimator for  $\tilde{\Pi}_z(\mathbf{k})$  simply implies that all observed density fluctuations are actually induced by internal waves. Usually, this assumption overestimates the variance of the wave-induced density fluctuations and thus we will designate this estimator as "upper-limit estimator" and it reads:

$$\tilde{\Pi}_z(\mathbf{k}) \leq \frac{E_p(\mathbf{k})}{\left\langle \frac{\partial \rho}{\partial z} \right\rangle^2}, \quad (3.2.3)$$

where  $E_p(\mathbf{k})$  is the energy density of density fluctuations observed by the instruments installed on the platform.

Uittenbogaard (1993) presented IWE-estimators for random linear internal gravity waves. His derivations motivates the introduction of what we will designate as "absolute quad-spectra" which are defined by

$$|Q|_{\rho u_i} = \left\langle |F_\rho(\mathbf{k})^{cc} F_{u_i}(\mathbf{k})| \right\rangle. \quad (3.2.4)$$

In (3.2.4)  $(\cdot)^{cc}$  is the complex conjugate,  $F_\rho(\mathbf{k})$  is the Fourier transform of the density  $\rho(\mathbf{x})$  and  $F_{u_i}(\mathbf{k})$  is the Fourier transform of the Cartesian velocity component  $u_i(\mathbf{x})$  ( $i=1,2,3$ ). The absolute quad-spectra reduce the cancellation, when averaged over separate records, of the energy contained in waves with wavenumber vector  $\mathbf{k}$  in one record and with opposite wavenumber vector  $-\mathbf{k}$  in another record. Actually, the application of the absolute sign in (3.2.4) is not necessary if indeed the 3D-Fourier transform of the relevant signals are available, like in Direct Numerical Simulations. However, in field observations only the time records of the relevant signals are given. Using Taylor hypothesis the frequency spectra are converted into approximations of the 1D energy spectra in streamwise wavenumber  $k$ . The latter implies averaging of the 3D energy density spectrum over planes  $k=\text{constant}$  such as shown in (2.6.10). Consequently, the sign of the transverse wavenumber  $\ell$  as well as the vertical wavenumber  $m$  is lost. However, this sign is essential in averaging the quadratures (2.4.27) and (2.4.29) and the absolute value in (3.2.4) attempts to avoid cancellation of contributions to quad spectra at opposite signs of  $\ell$  and of  $m$ .

Yet absolute quad-spectra cannot avoid such a cancellation when waves with equal wavelength, but propagating in opposite directions, occur in one record. Hence, the absolute quad-spectra provide a lower-limit estimator. However, this lower-limit estimator is biased by the addition of contributions from turbulent fluctuations. Uittenbogaard (1991) has shown theoretically that quadrature spectra of turbulent motions in a simple shear flow are negligible and this conclusion is supported by measurements of the phase angle  $\phi_{\rho w}$  which is either  $0^\circ$  or  $180^\circ$  according to Lienhard and Van Atta (1990) and according to Yoon and Warhaft (1990). However, taking the average of absolute quad spectra, instead of the absolute value of the averaged quadrature spectra, creates the addition of turbulence contributions and consequently a bias of our lower limit estimator.

Under the condition of stationary waves in a flow with negligible vertical curvature of the mean streamwise velocity we obtain after substitution of (2.4.24), (2.4.27) and (2.4.29) into (3.2.4):



$$\tilde{\Pi}_z(\mathbf{k}) = \chi \tilde{\Pi}_t(\mathbf{k}) , \quad (3.2.5)$$

$$\text{with } \chi = \left( N \left| \left\langle \frac{\partial \rho}{\partial z} \right\rangle \right| \right)^{-1} \text{ and } \tilde{\Pi}_t(\mathbf{k}) = \left( |Q|_{\rho u}^2 + |Q|_{\rho v}^2 + |Q|_{\rho w}^2 \right)^{1/2} . \quad (3.2.6)$$

In (3.2.6) use was made of absolute quad-spectra (3.2.4). We define  $\tilde{E}_t(\mathbf{k})$  as the lower-bound estimator of the 3D energy density of the wave-induced vertical displacement, although this lower bound may be biased by contributions from turbulence, as we discussed previously. Incidentally, to test the coding of the fairly complicated expressions (3.2.4) and (3.2.6), a generator of a random linear internal wave field was constructed. This generator and the tests are described in (Uittenbogaard, 1993).

Further, the observations are made from a moving suspended platform and the necessary correction procedures are described and tested in the first report of the Rotterdam Waterway field campaign (Uittenbogaard, 1993).

In view of the derivations in Section 2.4 the brackets  $\langle \dots \rangle$  in (3.2.1), (3.2.4) and (3.2.6) actually represent time averaging per wavenumber  $\mathbf{k}$ . In practice, spectral analysis is based on time series obtained with fixed instruments and the flow passing through the measuring volumes. Mean spectra are obtained by subdivision of the registration into partly overlapping records and subsequently averaging over each spectrum derived from a record.

With reference to spectral analysis there is an additional problem when comparing (3.2.1) with the total kinetic energy defined in the usual manner. First we quote Tennekes and Lumley (1983, p. 250). "Often, the velocity components  $u$ ,  $v$  and  $w$  are measured separately. However, for spectral analysis we need a spectrum that represents all of the kinetic energy at a given wavenumber. Therefore, the spectra of  $u$ ,  $v$  and  $w$  are commonly added together; it is the spectrum of the total energy which is always referred to as the three-dimensional spectrum."

In general this procedure is also followed when three orthogonal turbulence velocity components are measured simultaneously. The summation is proportional to the first invariant of the spectral representation of the Reynolds stress tensor (2.2.4) and in this respect the result is an objective measure, independent of the possible wavenumber-dependence of the principal directions. However, the summation neglects the possibility that the components ( $u, v, w$ ) are interrelated for instance in a way that their magnitude is preserved. Then the square root of the sum of the squares of the spectral energy densities of ( $u, v, w$ ) would be a better spectral representation of the kinetic energy.

This point is hidden in the IWE estimator (3.2.1) because it first relates the KIWE to the wave-induced vertical displacement spectrum, which is a scalar quantity. In Chapter 2 we have derived that for linear waves in a stably stratified shear flow the wave-induced velocity components all refer to a single scalar. In particular the estimator (3.2.6), originating from (2.4.30) and the text line preceding (2.4.30), shows the summation in terms of magnitude per wavenumber.

In the test program with generation of 3D internal waves, mentioned earlier, we checked that (3.2.6) is indeed the correct definition to compare the results with the total kinetic energy obtained by summation of spectra of each velocity component.



### 3.3 Upper limits for spectra of internal wave fields

In Section 2.6 we discussed criteria for the breaking of a monochromatic internal wave either by gravitational instability or by a wave-induced Kelvin-Helmholtz instability. The discussion concluded that the upper limit of the wave-induced vertical gradient  $\partial\tilde{\rho}/\partial z$  enters both criteria. In addition, we can imagine a wave field consisting of spatially separated wave groups or conversely an internal wave field consisting of interfering, overlapping wave groups. In the latter situation we expect a broad-banded spectrum in every temporal record made at a fixed location.

Anticipating our observations in the Rotterdam Waterway Estuary, we will derive an upper limit for IWE based on the presence of internal waves with such a continuous spectrum. In view of (2.6.9) we will assume that the rms  $|\partial\tilde{\rho}/\partial z|$  of the wave-induced vertical density gradient still remains the essential parameter for estimating the energy of internal waves close to the limit of breaking. In Chapter 4, this assumption will be checked against observations.

To arrive at such a criterion we will consider the wave-induced vertical displacement  $\tilde{Z}$  induced by a broad-banded internal-wave field. In accordance with field observations and with dimensional analysis we took the shape of its 1D-spectral energy as a function of the vertical wavenumber  $m$  proportional to  $m^{-3}$ , see (2.6.12) and the text accompanying it. We start with the Fourier-Stieltjes integral (Batchelor, 1953, p. 32) or (Phillips, 1980) for vertical displacement  $\tilde{Z}$ :

$$\tilde{Z}(\mathbf{x}, t) = \int \exp(i\mathbf{k} \cdot \mathbf{x}) dF_Z(\mathbf{k}, t), \quad (3.3.1)$$

The integral (3.3.1) in wavenumber space extends over all feasible wavenumber components  $\mathbf{k}, \ell \in (0, k_+)$  where  $k_+$  is the upper limit of horizontal wavenumbers to be determined in Section 3.4. Moreover, the vertical wavenumber is restricted to  $m \in (M, m_+)$  where  $M = 2\pi/H$  and  $H$  the typical thickness of the stratified layer under consideration. Further, the wave field is considered random and stationary so that for fixed  $\mathbf{k}$ :

$$\lim_{d\mathbf{k} \rightarrow 0} \langle dF_Z(\mathbf{k}, t) dF_Z^\infty(\mathbf{k} + d\mathbf{k}, t) \rangle = \tilde{\Pi}_Z(\mathbf{k}) d\mathbf{k}, \quad (3.3.2)$$

where  $\tilde{\Pi}_Z(\mathbf{k})$  is the spatial density function defined in (3.2.1). This formulation excludes the occurrence of a modal structure for which waves at different wavenumbers are mutually coupled. We motivate this assumption by the conceptual basis formed by means of the analysis in Section 2.7 on wave-wave interactions. There it appears that decoupling or detuning of modal structures is probable. In other words, before a wave group with a short vertical wavelength returns to its initial position, after reflection, it has suffered so many phase perturbations that the formation of a modal structure is prohibited.

The wave-induced density gradient is derived from mass conservation and the perturbation of a locally-linear vertical background density profile and yields:

$$\frac{\partial\tilde{\rho}}{\partial z} = \left\langle \frac{\partial\rho}{\partial z} \right\rangle \frac{\partial\tilde{Z}}{\partial z} = \left\langle \frac{\partial\rho}{\partial z} \right\rangle \int (im) \exp(i\mathbf{k} \cdot \mathbf{x}) dF_Z(\mathbf{k}, t). \quad (3.3.3)$$

From (3.3.3) and (3.3.2) follows the variance of the density gradients induced by a random and broad-banded wave field. This variance reads

$$\left\langle \left( \frac{\partial\tilde{\rho}}{\partial z} \right)^2 \right\rangle = \left\langle \frac{\partial\rho}{\partial z} \right\rangle^2 \int m^2 \tilde{\Pi}_Z(\mathbf{k}) d\mathbf{k} = \left\langle \frac{\partial\rho}{\partial z} \right\rangle^2 \int_M^{m_+} m^2 \tilde{E}_Z(m) dm, \quad (3.3.4)$$

where by definition  $\tilde{E}_Z(m) = \int_0^{k_+} \int_0^{k_+} \tilde{\Pi}_Z(k, \ell, m) dk d\ell$  is the one-dimensional spectrum discussed in Section 2.6, see (2.6.10)

The integration in (3.3.4) extends over a bandwidth of vertical wavelengths with the maximal wavelength  $H = 2\pi/M$  and the minimal wavelength  $\lambda_+ = \lambda/m_+$  to be determined later. Substitution of (2.6.12) into (3.3.4) yields the ratio  $\alpha$ , defined through (2.6.9). This gives the following estimator for the coefficient  $c$  appearing in the spectrum (2.6.12):

$$c = \frac{\alpha^2}{\ln(b_z)}, \quad (3.3.5)$$

with bandwidth  $b_z = H/\lambda_+$ .

The quantity  $\ln(b_z)$  is proportional to the number of decades at the vertical wavenumber bandwidth occupied by internal gravity waves. Given some value for  $\alpha$ , the wider the bandwidth in vertical wavelengths the lower is the spectral energy density of the internal wave field:

$$\tilde{E}_Z(m) = \frac{\alpha^2}{\ln(b_z)} m^{-3}; \quad \alpha^2 = \left\langle \left( \frac{\partial \tilde{Z}}{\partial z} \right)^2 \right\rangle. \quad (3.3.6)$$

Until this point we did not assume the nature of the motions. However, in the following we rely on linear theory. Using (2.6.13) the variance of the wave-induced shear rate can be converted into

$$\langle \tilde{\gamma}^2 \rangle = \frac{1}{2} N^2 \int_0^{k_+} \int_0^{k_+} \left[ \int_M^{m_+} (k^2 + \ell^2 + m^2) \left( 1 + \frac{\sin^2 \phi(k, \ell)}{Ri} \right) \tilde{\Pi}_Z(k) dm \right] dk d\ell; \quad \sin \phi = \frac{\ell}{k^2 + \ell^2} \quad (3.3.7)$$

Observe that the factor  $1/2$  in (3.3.7) originates from the connection between the strain rate variance and the internal wave enstrophy. The formation of critical layers, the trapping of internal waves with small enough horizontal wavelengths in wave guides and the subsequent growth of internal waves by shear production promotes the assumption that the 3D-spectral energy density is concentrated around  $|\Theta| = 90^\circ$  with  $\ell \approx 0$  so that (3.3.7) may be approximated by:

$$\langle \tilde{\gamma}^2 \rangle \approx \frac{1}{2} N^2 \int_M^{m_+} m^2 \tilde{E}_Z(m) dm, \quad (3.3.8)$$

or using (3.3.4) and (2.6.9) and repeating the definition (2.6.13) for strain rates

$$\langle \tilde{\gamma}^2 \rangle = \langle \tilde{\underline{d}} : \tilde{\underline{d}} \rangle \approx \frac{1}{2} \alpha^2 N^2. \quad (3.3.9)$$

In (3.3.9) we have omitted multiplication with the factor  $\left\{ 1 + \frac{\langle \sin^2 \phi(k, \ell) \rangle}{Ri} \right\}$

because an estimate for  $\langle \sin^2 \phi(k, \ell) \rangle$ , weighted by  $\tilde{\Pi}_Z$ , is not known. Finally, the assumptions made to arrive at this point, is of random linear and stationary waves superimposed on a stratified shear flow and that most of the potential energy of the waves is concentrated in waves with  $|\Theta|$  near  $90^\circ$  forming relatively long and thin horizontally layered velocity structures.



Expression (3.3.9) allows us to assess whether the wave-induced shear, rather than the wave-induced vertical density gradient, significantly promotes the occurrence of the Kelvin-Helmholtz instability. In view of the conceptual basis formulated at the end of Section 2.7 we should integrate the wave-induced strain rates as they contribute to straining and possibly breaking of short internal waves. Then a relevant criterion may be an alternative Richardson number  $\langle \tilde{Ri} \rangle$  which equals the background Ri corrected for the increase of only strain rate and it reads:

$$\langle \tilde{Ri} \rangle = \frac{N^2}{\langle \gamma \rangle^2 + \langle \tilde{\gamma}^2 \rangle} \leq \frac{1}{4} ; \quad \frac{1}{2} \alpha^2 \geq 4 - \frac{1}{Ri} . \quad (3.3.10)$$

To obtain the second inequality we have substituted (3.3.9) into the first inequality of (3.3.10). Of course (3.3.10) is a crude step because it is borrowed from linear stability analysis for a steady stratified flow rather than the time-dependent wave-induced straining we consider here. Hence, we can only make the following conjecture. For  $Ri \geq 1$  the last inequality of (3.3.10) would require  $\alpha \geq 2.4$  to make the wave-induced shear intense enough to reduce the momentary Richardson number occasionally below  $\frac{1}{4}$ . However, in view of the definition of  $\alpha$  through (2.6.9), either gravitational instability or the hydrodynamic instability due to a reduced stratification would already have occurred at lower values of  $\alpha$ .

Hence, an upper limit of  $\alpha$  determined by (2.6.9) for the reduction of stratification or even overturning appears more restrictive than one determined by the enhancement of the total strain rate only. This suggests that (2.6.9) with the upper limit (2.6.5) derived from Orlandi's standing wave experiments is the most restrictive criterion to define saturation of the internal wave spectra. Observe that (2.6.9) does not rely on the linear wave theory which we needed to derive (3.3.10).

We will call the 1D spectral energy density of the vertical displacement "saturated" if an increase in spectral energy is equally reduced by immediately loss by wave breaking. Appendix A is devoted to Gibson's definition (Gibson, 1986) of a saturated internal wave spectrum. The upper limit, of what we call, Gibson's constant of proportionality  $G_i$  in the 1D spectrum for the transverse-shear defined as

$$\Phi_{\partial u / \partial z} = G_i \cdot N^2 m^{-1} \quad (3.3.11)$$

equals  $2c/3$  with  $c$  defined in (3.3.5). Gibson (1986) derives  $G_i = 6.7$  which would yield  $c = 10$  and in our opinion grossly overestimates the upper limit of  $\alpha^2$ . However, this tentative conclusion is based on linear wave theory. Nevertheless, breaking internal waves were observed during the Rotterdam Waterway field campaign and the arrangement of instruments in this campaign allowed the determination of  $\alpha$  as discussed before.

Another interesting feature of (3.3.9) is the ratio between the variance of the wave-induced strain rate and the one for the horizontal mean flow:

$$\frac{\langle \tilde{\gamma}^2 \rangle}{\langle \gamma \rangle^2} \approx \frac{1}{2} \alpha^2 Ri . \quad (3.3.12)$$

We may add the variance of wave-induced strain rate to the turbulence production  $P$  which we defined in (2.2.21) and which appears in the transport equation (2.2.26) for turbulent kinetic energy. In this respect the ratio (3.3.10) indicates the importance of turbulence production by wave straining versus turbulence production by the mean flow. However, in addition to a large ratio in (3.3.12) there must also be a sufficiently fast response of the turbulence stresses to the wave-induced strain rate. In Chapter 4 we will assume such a fast response to assess the additional turbulence production using the  $q^2$ - $\epsilon$  turbulence model.

A ratio comparing the typical time scale of energetic turbulent eddies versus the time scale for internal waves is the turbulent Froude number  $Fr_T$ , also called activity parameter:

$$Fr_T = \frac{|\bar{u}^*|}{NL_c} . \quad (3.3.13)$$

In (3.3.13) is  $|\bar{u}^*|$  the rms value of turbulent velocity fluctuations and  $L_c$  an observable length scale representing the typical size over density overturning (turbulent) eddies. The next section presents estimators for these turbulence parameters, given  $N$  and estimates for the rate of energy dissipation  $\epsilon$ .

We conclude here by estimating the upper limit of the so-called Ellison length scale  $\tilde{L}_E$  due to a continuous spectrum of internal waves:

$$\tilde{L}_E = 2 \frac{|\bar{\rho}|}{\left\langle \frac{\partial \rho}{\partial z} \right\rangle} \equiv 2 |\bar{Z}| \equiv \left( \frac{\alpha H}{\pi \sqrt{2}} \right) \ln^{-1/2}(b_z) (1 - b_z^{-2})^{1/4} , \quad (3.3.14)$$

with bandwidth  $b_z = H/\lambda_+$ .

Please note that for an internal wave field without statically unstable density profile,  $\tilde{L}_E$  can be significant while for the overturning length scale holds  $L_c=0$ . In (3.3.14) we introduced the factor of 2 to indicate typical wave heights. Fortunately, the estimator (3.3.14) depends only weakly on the difficult to estimate bandwidth  $b_z$  of internal gravity waves provided  $b_z$  is about 10 or larger. For instance, compare

$$\tilde{L}_E = 0.11(\alpha H) \text{ for } b_z = 50 \text{ against } \tilde{L}_E = 0.09(\alpha H) \text{ for } b_z = 500 . \quad (3.3.15)$$

For reference with other published estimators of spectral energy density, usually for  $Ri \rightarrow \infty$ , the expression (3.3.6) is converted into the 1D-spectrum  $\tilde{E}_u(m)$  of KIWE:

$$\tilde{E}_u(m) = \frac{\alpha^2}{\ln(b_z)} \left[ N^2 + \left( \frac{\partial U}{\partial z} \right)^2 \right] m^{-3} , \quad (3.3.16)$$

with  $\langle \tilde{u} \cdot \tilde{u} \rangle = \int_{\mathbf{M}}^{\mathbf{m}_*} \tilde{E}_u(m) d\mathbf{m}$  and using (3.3.5).

Apart from  $\alpha$  all other quantities entering (3.3.14) are observable through our mutual microstructure and timescale measurements. The buoyancy frequency and the typical stratified layer thickness  $H$  follow from the vertical finescale measurements or from averaging over microstructure drops. In addition, the instruments on the platform record, among other signals, the streamwise density variations and, combined with the mean vertical density profile, it yields the wave-induced Ellison length scale  $\tilde{L}_E$ .



The definition of the minimal vertical wavelength  $\lambda_+$  of internal waves is presented in the next section. It will be related to an averaged (vertical) overturning length scale, whereas (3.3.15) shows that the estimator for  $\tilde{L}_B$  is not very sensitive to the particular bandwidth  $b_z$ . Hence,  $\alpha$  or  $(\alpha.H)$  can be estimated from experiments and the assertion (2.6.9) can be checked provided breaking waves are observed. In addition, the ratio (3.3.12) follows from these observations because  $Ri$  follows from the finescale measurements.

In the next section we introduce other parameters which will classify and partially quantify turbulence in stratified flows. Most of these parameters follow from microstructure experiments and exploit empirical laws which were obtained from laboratory experiments of grid-generated stratified turbulence.

### 3.4 Bandwidth of inertia-dominated turbulent motions

Before we enter our analysis in terms of wavenumbers and length scales we will define their interrelation when we consider spatially random processes. We begin with length scales and conclude with the relation to wavenumbers/wavelengths.

In turbulence the common approach is to compare "typical length scales" of different turbulence processes such as turbulence production, viscous dissipation of turbulence etc.. Grossly speaking, the following three methods exist to define typical length scales of turbulence processes.

- First, length scales are geometrically related to, or restricted by the flow geometry. For instance, "the most energetic eddy has a size proportional to the distance to the nearest rigid wall or interface with a strong density difference". An example is the so-called Prandtl mixing length scale for transverse momentum and concentration exchange in a turbulent boundary layer with Von Kármán constant  $\kappa=0.40$  as factor of proportionality.
- Second, the length scales are mathematically well defined by the relevant normalized spatial correlation functions of velocity, scalar quantity, first or higher order derivatives of velocity and of scalar etc.. Integration of the spatial correlation function along a preferred direction or over the entire fluid volume provides a mathematically well defined "integral" length scales if the turbulence properties approximate homogeneity well enough, which actually is a requisite for the proper application of spatial correlation functions.
- Third, the length scales are mathematically well defined through scaling arguments in terms of turbulence state parameters and to some extent resembles the first method. An example is the definition (2.2.25) of the Kolmogoroff length scale.

In this report we will mainly use length scales following from the third method and occasionally by means of the first strategy. The question is what typical wavenumbers belong to these typical length scales? Hinze (1975, section 3-2, p. 224-225) has shown, for various mathematical approximations to the observed energy density spectra, that the proper connection between typical wavelength  $\lambda_L$  or the typical wavenumber  $k_L$  belonging to length scale  $L$  simply reads:

$$k_L \approx \frac{1}{L} ; \lambda_L \approx 2\pi L .$$

Examples, based on grid-generated turbulence, are found in Hinze (1975, p.253, fig. 3-16). In this report we will apply this translation from length scales into wavenumbers also for length scales defined by the third method.

We define active turbulence when its inertial forces overcome the buoyancy forces. For an estimate of length scales involved we define an locally centred displacement scale  $\bar{s}^*$ .

Fig. 3.4.1 indicates that the centred displacement  $|\bar{s}^*|$  is an observable quantity. A probe, falling or rising fast enough through the water column, can record the momentary density profile. Following appropriate criteria, a series of stationary sections of this profile are selected. The entire profile is reordered into a monotonous profile so that  $|\bar{s}^*(z)|$  is known. According to Imberger and Boashash (1986, fig. 6) the centred displacement  $|\bar{s}^*(z)|$  is defined in the centre of eddy in Fig. 3.4.1. Finally, all available  $|\bar{s}^*(z)|$  are averaged per section to obtain the centred displacement scale  $L_C(z)$ . This scale still depends on  $z$  but is a mean value of  $|\bar{s}^*(z)|$  per stationary section.

Observe that  $L_C$  is indeed a signature of turbulence because of the reordering into a monotonous profile. In other words, it indicates sections where  $\alpha$  in (2.6.9) is large enough to create overturning. However, if only non-breaking internal waves without turbulence are present then  $L_C = 0$  whereas the Ellison scale  $L_E$  (3.3.14) indicates internal waves (Caldwell, 1982). Fortunately,  $L_C$  is expected to depend only weakly on the internal wave straining of the density profile (Itsweire, 1984). We may expect that holds  $L_E \geq L_C$ .

Another feature of the definition of  $L_C$  is the following. Consider low-pass filtering of the momentary vertical density profile  $\rho(z)$  with a variable bandwidth  $\lambda \geq 2\pi L_C(z)$  into profile  $\rho(z; L_C)$ . Then it is unlikely that  $\partial\rho(z; L_C)/\partial z$  of the smooth profile becomes positive (gravitational instability).

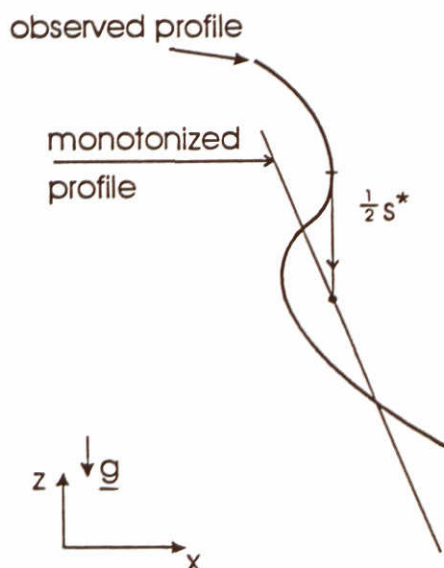


Fig. 3.4.1. Definition of locally centred displacement  $\bar{s}^*$ .



For convenience we will summarize parts of the studies (Ivey and Imberger, 1991), Gibson (1981) and others referred to in the following text. These and other studies were devoted to define the state of turbulence in stably stratified fluids.

According to Fig. 3.4.1,  $\bar{s}^*$  equals twice the momentary vertical centred displacement and at the largest scales we put  $\bar{u}^* \approx \frac{1}{2}\Delta\bar{u}^*$  wherein  $\Delta\bar{u}^*$  is the velocity difference over length  $\bar{s}^*$ . Then the reader may easily follow the steps below, starting with the notion that inertial forces must exceed buoyancy forces:

$$\bar{\rho}^* = \frac{1}{2}\bar{s}^* \left\langle \frac{\partial \rho}{\partial z} \right\rangle ; \langle \rho \rangle (\bar{u}^* \cdot \bar{\nabla} \bar{u}^*) \geq \bar{\rho}^* g ; \langle \rho \rangle (\bar{u}^* \cdot \bar{\nabla} \bar{w}^*) \geq -\bar{\rho}^* g ; \bar{u}^* \cdot \frac{\Delta \bar{u}^*}{\bar{s}^*} \geq N^2 (\frac{1}{2}\bar{s}^*) ; \quad (3.4.1)$$

$$\langle (\Delta \bar{u}^*)^2 \rangle \geq N^2 L_C^2 \quad \text{with } L_C = |\bar{s}^*| .$$

The last comparison may be regarded as the statement that the vertical contribution to the turbulent kinetic energy must exceed the required potential energy necessary to overcome the vertical displacement. Alternatively, the last comparison in (3.4.1) may be view in terms of turbulence strain rates:

$$\frac{\langle (\Delta \bar{u}^*)^2 \rangle}{L_C^2} = \iota \left| \frac{\partial \bar{u}^*}{\partial z} \right|^2 , \quad (3.4.2)$$

where  $\iota \leq 1$  from turbulence statistics.

Combining the last comparison in (3.4.1) with (3.4.2) results into an equivalent Richardson number  $Ri_\iota$  for active turbulence:

$$Ri_\iota = \frac{N^2}{\left| \frac{\partial \bar{u}^*}{\partial z} \right|^2} \leq \iota . \quad (3.4.3)$$

Actually, (3.4.3) has been the starting point for Ozmidov (1965) and for Gibson (1981) to estimate the upper limit of turbulence length scales. As a matter of fact, Gibson (1981) quantified turbulence length scales by assuming  $\iota = \frac{1}{4}$  in (3.4.3). We used a similar criterion in (3.3.10). Although Gibson's results parallel laboratory observations we argue in Section A.2 of Appendix A that his estimates have quite some tolerance.

From dimensional considerations and from grid-generated experiments e.g. (Stillinger et al., 1983b) follows for turbulence in a stably-stratified uniform flow:

$$|\bar{u}^*| = a(\epsilon L_C)^{1/3} , \quad (3.4.5)$$

and  $a = (2.0)^{2/3} = 1.6$  (Ivey, Imberger, 1991, fig. 1).

According to (Itsweire, 1984)  $L_C$  is twice (2) the so-called rms-value  $(L_T)_{rms}$  of the so-called Thorpe displacement scale  $L_T$  and  $L_T$  is the momentary displacement from the centre of the eddy in Fig. 3.4.1. Unfortunately, from our experience this ratio 2 is a source of ambiguity in quantitative analysis. Incidentally, we have defined in (3.3.14) the wave-induced Ellison length scale accordingly. Substitution of (3.4.5) into the last comparison of (3.4.1) gives the range for  $|\bar{s}^*|$

$$|\dot{s}^*| \leq C_1 L_O ; C_1 = a^{3/2} ; L_O = \left( \frac{\epsilon}{N^3} \right)^{1/2} . \quad (3.4.6)$$

In (3.4.6) is  $L_O$  called the Ozmidov length scale, however, Ozmidov (1965) himself notes that Monin and Obukhov (1953) and Obukhov (1959) already understood the significance of  $L_O$  as an indicator of the maximal scale of isotropic turbulence in a stably stratified fluid. From (3.4.6), with empirical constant "a" given in (3.4.5), follows that the upper limit of  $|\dot{s}^*|$  practically equals twice the Ozmidov length scale or that  $L_R \approx (L_T)_{rms}$ . Actually, Itsweire (1984) summarizes from laboratory observations:  $L_R \approx (L_T)_{rms}$ . In view of the preceding arguments and the laboratory observations Itsweire (1984, fig. 4)  $|\dot{s}^*|$  grows after generation of turbulence from a value much smaller than  $L_O$  to its upper limit of about  $2.5 L_O$  which has also been observed in the ocean by Dillon (1982). The interested reader is referred to the discussion at the end of section A.2 of Appendix A where  $C_1 = 2.0$  is obtained instead of Gibson's estimate  $C_1 = 1.2$ .

The so-called inertial subrange of vertical wavelengths  $\lambda_t$  over which turbulence is inertial and turbulence is not directly affected by buoyancy nor by viscous damping is defined as:

$$\mu_K L_K < \frac{\lambda_t}{2\pi} < \mu_O L_O , \quad (3.4.7)$$

with  $\mu_O = 2$  and the lower limit  $\mu_K = 15$ .

Observe that we applied the connection, introduced in the begin of this Section 3.4, between typical wavelengths and typical length scales. Condition (3.4.7) is a save requirement that in the bandwidth of vertical wavelengths with the Ozmidov scale as upper limit turbulence is barely hindered by buoyancy effects. However, because the variance of the turbulent strain rates are involved we interpret (3.4.7) as follows. The part of the inertial subrange of turbulent motions satisfying (3.4.7) is hardly affected by buoyancy. In that range we may treat turbulence as if the flow is unstratified. Hence, the energy dissipation  $\epsilon$  based on turbulence in that inertial range is not (directly) influenced by buoyancy.

Consequently, assume isotropic turbulence in the range of small length scales where viscous dissipation occurs. Then, following Gibson (1981),

$$\epsilon = \nu |\dot{\gamma}^*|^2 = \frac{15\nu}{2} \left| \frac{\partial \tilde{u}}{\partial z} \right|^2 . \quad (3.4.8)$$

and substitution of (3.4.8) into (3.4.3) reveals for Gibson's choice  $\nu = 1/4$ :

$$\frac{|\dot{\gamma}^*|}{N} \geq 30^{1/2} . \quad (3.4.9)$$

Section A.2 of Appendix A discusses the tolerance in the criterion  $\nu = 1/4$ . The ratio (3.4.9) is the small-scale or strain-rate Froude number and it compares the strain rate of turbulence with the rate of adjustment by buoyancy, see (Imberger and Boashash, 1986) and (Ivey and Imberger, 1991). With the wave-induced strain rate estimate (3.3.9) from Section 3.3 we may compare equivalent Richardson numbers:

$$Ri_{\dot{\gamma}} = \frac{N^2}{|\dot{\gamma}^*|^2} \leq \frac{1}{30} ; Ri_{\dot{\gamma}} = \frac{N^2}{|\dot{\gamma}|^2} \approx \frac{2}{\alpha^2} \quad (3.4.10)$$

and the ratio between viscous dissipation by turbulence and viscous dissipation by internal gravity waves:



$$\frac{|\tilde{\gamma}^*|^2}{|\tilde{\gamma}|^2} \geq \frac{60}{\alpha^2} \quad (3.4.11)$$

For values of  $\alpha$  smaller than unity (3.4.11) shows that the major part of energy dissipation by work against viscous forces in a stratified flow is due to turbulence strain rates.

Still the question on the minimal vertical wavelength  $\lambda_+$  of internal waves must be answered. The upper limit of vertical gradients in the low-pass filtered density profile  $\rho(z; L_C)$  has been discussed in the text preceding equation (3.4.7). This points to a lower limit  $\lambda_+$  comparable or larger than half of the centred displacement scale of overturning motions:

$$\lambda_+ > \pi L_C \quad (3.4.12)$$

In view of the conceptual basis formulated at the end of Section 2.7 we expect that small-scale internal waves with vertical wavelengths approaching  $L_C$  break. The argument is that that a short internal wave breaks because it is strained by longer waves. Hence, for the purpose of stability analysis the integration of spectral energy to estimate the variance of vertical density gradients and of velocity gradients should start at the minimal wavenumber  $M$  and the integration must end where small-scale waves create overturning.

As indicated above, Gibson's estimate for  $c$  defined in (3.3.5) is much larger than ours if we use  $\alpha^2 < 1$ . Gibson based his estimate on a matching of transverse strain-rate spectra of isotropic turbulence to the one for internal waves. However, with  $\alpha$  about 1 we will find a mismatch in spectral energy density for velocity gradients. Hence, there may an intermediate range of vertical wavelengths where, for wavelengths increasing from  $L_C$ , turbulence becomes more and more anisotropic with typical horizontal particle excursions larger than vertical centred displacements. In this intermediate range the velocity pattern induced by anisotropic turbulence may indistinguishably match the pattern of small scale internal waves with  $|\Theta|$  near  $90^\circ$ . For more background we refer to Section 2.7 and the energy exchange between wave modes given in Figure 2.7.3.

### 3.5 Some existing dimensionless numbers

In view of (3.4.7) and the possible straining of turbulence by internal gravity waves, the following three dimensionless numbers all related to the dissipation  $\epsilon$  indicate the state of turbulence:

$$Re_T = \frac{\epsilon^{1/3} L_C^{4/3}}{\nu} ; Fr_\gamma = \frac{\epsilon}{\nu N^2} ; Fr_T = \left( \frac{\epsilon}{N^3 L_C^2} \right)^{1/3} \quad (3.5.1)$$

For  $Re_T \geq 100$  the so-called high-Reynolds number turbulence models are applicable in which the energetic part of the turbulent fluctuations are not directly affected by viscous dissipation (Launder, 1984). Turbulence exists if  $Re_T \geq 15$  (Ivey and Imberger, 1991, table 1). If  $Fr_\gamma \geq 5$  and  $Re_T \geq 15$  then an inertial subrange/bandwidth of 3D-turbulent eddies exist. With  $Fr_T$  and  $Re_T$  as descriptive state parameters an impressive summary of the types of turbulence in various flow regimes is presented in (Imberger and Ivey, 1991, fig. 3).

If  $Re_T$  is large and  $Fr_T \geq 2$  then turbulence is very active and its slow part may excite and thus transfer energy to internal waves (Uittenbogaard and Baron, 1989), (Zic and Imberger, 1993). If  $Fr_T \geq 1$  turbulence interacts with internal waves and turbulence may even excite internal waves but conversely also consume internal wave energy.

Finally, if  $Fr_T$  is about 1 as well as  $(L_B/L_C)^2 \gg 1$  holds then we postulate that turbulence is mainly the consequence of interacting and possibly breaking internal waves.

Ivey and Imberger (1991) define the following dimensionless numbers which can be obtained from drops with a temperature-conductivity probe:

$$Re_T = \left( \frac{L_C}{L_K} \right)^{4/3} ; Fr_Y = \left( \frac{L_O}{L_K} \right)^{2/3} ; Fr_T = \left( \frac{L_O}{L_C} \right)^{2/3} . \quad (3.5.2)$$

The dimensionless numbers (3.5.2) are inspired by (3.5.1), however, the numbers in (3.5.2) are not based on assumptions of inertial subranges or empirical data. The definitions (3.5.2) contain three independent length scales and the three dimensionless numbers are interrelated as follows

$$Fr_T = Re_T^{-1/2} Fr_Y . \quad (3.5.3)$$

$Fr_T$  is called the turbulence Froude number because it is related to turbulence parameters only. This overview is not complete and dimensionless numbers for other hydrodynamic processes may be added. For instance, recently Imberger (1994) proposed to add a turbulent Grashof number

$$Gr_T = \frac{N^2 L^4}{\nu^4}$$

to classify natural convection. Except for the latter, we will present in Chapter 4 these numbers derived from field observations in the Rotterdam Waterway Estuary.

### 3.6 Rate of energy dissipation and eddy diffusivity

The Ozmidov and Kolmogoroff length scales require, among other parameters, the rate of viscous dissipation  $\epsilon$  as input. This rate is estimated from temperature gradient spectra disregarding whether the flow is temperature or salinity stratified. The temperature fluctuations dissipate mostly near the so-called Batchelor scale for temperature (Tennekes and Lumley, 1983, ch. 8) and in water this scale practically equals the Kolmogoroff scale. Further, the Batchelor scale for temperature dissipation is about 20 to 30 times larger than the Batchelor scale where salt fluctuations dissipate. Provided the flow is not too turbulent, i.e.  $\epsilon$  is not too large, then the temperature gradient spectrum is observable with the present size of thermistors. This is not the situation for salt because the size of conductivity probes is too large in comparison with the relevant Batchelor length scale.



The shape of the relevant spectra are given in (Gibson and Schwartz, 1963). References to the measurement of temperature fluctuations along the water depth with a free falling probe go back to Caldwell et al. (1975). Presently, the method is well established, extensively tested in the laboratory as well as in the field, see e.g. (Dillon and Caldwell, 1980).

In this field campaign a microstructure profiler was used to obtain temperature and conductivity profiles. In the nose of the profiler two groups of sensors are located next to each other and about 30 mm apart. Each sensor group consists of a small and fast responding temperature and conductivity sensor with a typical length scale for their measuring volume of about 1 mm. Their signals, including the water pressure, were sampled at 100 Hz while the probe sinks at about 0.1 m/s. The high frequency roll-off of the temperature probe was partly corrected for to maximize its small-scale sensitivity. The raw data was stored digitally and later, on shore, processed to obtain  $\epsilon$ ,  $L_C$ ,  $N^2$  and other parameters of the flow field.

From analytical as well as experimental observations on grid-generated stratified turbulence Ivey and Imberger (1991) derive  $R_f$ , a generalized flux Richardson number, from the Froude number (3.5.2):

$$R_f = R_f(Fr_T) \quad (3.6.1)$$

$$\text{with the definition : } R_f = \frac{\epsilon}{B + \epsilon} , \quad (3.6.2)$$

$$\text{using buoyancy flux : } B = \Gamma_T N^2 , \quad (3.6.3)$$

$$\text{with eddy diffusivity: } \Gamma_T . \quad (3.6.4)$$

The essential inputs to estimate  $\Gamma_T$  are  $L_C$ ,  $N^2$  and  $\epsilon$  from records with the microscale profiler. The procedure to estimate the eddy diffusivity from the observed parameter  $L_C$ ,  $N$  and  $\epsilon$  is as follows. First  $Fr_T$  using (3.5.2) is estimated and with the calibration (3.6.1)  $R_f$  is estimated next. Then from (3.6.2) follows the buoyancy flux  $B$  and finally, given  $\epsilon$ , the eddy diffusivity  $\Gamma_T$ . The assumption of uniform flow underlying (3.6.1) instead of a tidal shear flow may be a weakness in this procedure.

### 3.7 A new dimensionless number: wave-detectability parameter

In this section we propose an internal wave-detectability parameter  $W$ . For that purpose we define the mean fluctuating potential energy  $\frac{1}{2}N^2 \langle Z'^2 \rangle$  with vertical fluctuation displacement  $Z'$  induced by waves and by turbulence. We compare this energy content with the kinetic energy  $\bar{q}^2(k_C)$  of isotropic turbulent motions confined in the inertial subrange with maximal wavelength  $\pi L_C$  ( $k_C = 2/L_C$ ) based on the centred displacement scale  $L_C$ :

$$\bar{q}^2(k_C) = \int_{k_C}^{\infty} A \epsilon^{2/3} k^{-5/3} dk ; A \approx 1.7 . \quad (3.7.1)$$

Based on our arguments that internal waves may induced large density variations without necessarily breaking we argue that if  $\frac{1}{2}N^2\langle Z'^2 \rangle$  largely exceeds  $\bar{q}^2(k_C)$  then there exists a wavenumber range  $k < k_C$  wherein turbulence becomes anisotropic and internal wave motions prevail. Hence, we define

$$W = \frac{\frac{1}{2}N^2\langle Z'^2 \rangle}{\bar{q}^2(k_C)} \approx 0.07 \frac{L_E^2}{(L_O^2 L_C)^{2/3}}, \quad (3.7.2)$$

$$\text{because } \frac{2^{2/3}}{12A} \approx 0.07.$$

If the turbulence is active enough to occupy the entire inertial subrange then  $L_C = C_1 \cdot L_O$  with  $C_1 = 2.5$ . The ratio  $C_1$  follows from (Itsweire, 1984, fig. 4) with  $L_O \approx 0.8 \langle L_T \rangle_{\text{rms}}$  and  $\langle L_T \rangle_{\text{rms}}$  is the rms of Thorpe's displacement scale, see Section 3.4 for further comments on this and other scales. Consequently, (3.7.2) yields:

$$W \approx \left( \frac{L_E}{2L_C} \right)^2. \quad (3.7.3)$$

For  $W \leq 1$  the internal wave motions, if they exist, are submerged into or overwhelmed by turbulence and the waves are at least poorly detectable. Actually, this assertion is encouraged by observations in grid-generated stratified turbulence where  $L_E \approx L_C$  according to (Itsweire, 1984, fig. 3). In the experiments he refers to, as well as experiments performed more recently, no apparent internal waves have been detected in terms of a 90° phase shift and a large coherence between fluctuations of density and of the vertical velocity component.

In the following we estimate the required bandwidth  $b_{\text{DNS}}$  for DNS (Direct Numerical Simulations) to make  $W$  larger than unity. We apply our assumption that the centred displacement scale  $L_C$ , rather than the Ozmidov scale  $L_O$ , determines the bandwidth of 3D turbulence. Hence, we develop the bandwidth as follows:

$$b_{\text{DNS}} = \frac{H}{L_K} = \frac{H}{L_E} \frac{L_E}{L_C} \frac{L_C}{L_K}. \quad (3.7.4)$$

We estimate the ratios in (3.7.4) as follows. Using (3.3.15)  $(H/L_E) \approx 10/\alpha$  and for turbulence to exist  $(L_C/L_K) \geq 15$  and for waves to be detectable  $(L_E/L_C) \geq O(2)$ . Hence,

$$b_{\text{DNS}} \geq O\left(\frac{300}{\alpha}\right). \quad (3.7.5)$$

Observe that the lower bound (3.7.5) is (i) without an inertial subrange which would require at least one order of magnitude more i.e.  $(L_C/L_K) \geq 150$  instead of  $(L_C/L_K) \geq 15$  and (ii) the lower bound implies  $W = 0.6$  instead of our preference  $W \geq O(10)$ . However, the present computer limitations limit  $b_{\text{DNS}} \leq 256$  with maximal  $512^3$  grid points for three dimensional flow and therefore with DNS internal gravity waves have not been clearly observed or detected yet. We refer to the relevant part of Section 2.8 for a brief literature survey on this matter.



### 3.8 Energy flux of internal waves breaking in a shear flow

In this section we attempt to estimate the rate of energy transfer from internal waves to turbulence by breaking. Essentially, we assume that wave breaking is promoted by the strain rate of the main flow rather than by wave-wave interactions described in Section 2.7. Hence, the following derivations are not meant for very high Richardson number flows such as practically stagnant stratified water bodies.

We repeat the refraction equation (2.5.20) for stationary internal waves or solitary wave groups:

$$\left. \frac{dm}{dt} \right|_{\text{group}} = c_{gz}^* \frac{dm}{dz} = -k \frac{dU}{dz} + \cos\theta \frac{dN}{dz} \quad (3.8.1)$$

In (3.8.1) we have added the time derivative ( $dm/dt$ ) which implies: the temporal change of the vertical wavenumber "m" while following the same wave group. Division of (3.8.1) by the constant horizontal wavenumber  $(k^2 + \ell^2)^{1/2}$  yields

$$\left. \frac{d \tan\theta}{dt} \right|_{\text{group}} = -\cos\phi(k, \ell) \frac{dU}{dz} + \frac{1}{|k|} \frac{dN}{dz} \quad (3.8.2)$$

Equation (3.8.2) shows that for  $\ell=0$  the increase in  $\tan\theta$  is greatest i.e. the critical layer formation of waves travelling in the vertical plane of the main flow is fastest.

For small vertical wavelengths as well as for gradual vertical changes in buoyancy frequency the last term in (3.8.2) is insignificant.

Hence, the typical time scale  $\tau_c$  to increase the magnitude of  $\tan\theta$  by an amount  $\Delta_\theta$  simply follows from (3.8.2):

$$\tau_c \approx \frac{\Delta_\theta}{\left| \frac{dU}{dz} \right|} \quad (3.8.3)$$

Expression (3.8.3) shows the time interval  $\tau_c$  before the wave group is deformed into a critical layer. Theoretically, it would take an infinite time to obtain the exact (linearized) critical layer condition  $|\theta| = 90^\circ$  (Booker and Bretherton, 1967). Practically, an increment  $\Delta_\theta = 5-10$  would already bring  $\theta$  from  $0^\circ$  to about  $79^\circ$  to  $84^\circ$ .

With reference to our discussion in Section 2.6 on criteria for breaking of a monochromatic internal wave or a solitary wave group we conjecture the following. After the time interval  $\tau_c$  we assume that the wave group is deformed by such an extent that  $\mu$ , defined by (2.6.2), passes its critical value and either the gravitational instability ( $Ri < 0$ ) or the Kelvin-Helmholtz instability ( $Ri < 1/4$ ) occurs. Through numerical computation of internal waves near a critical level, Fritts (1976, fig. 5) indicated that the difference between these two instabilities is marginal. Further, in Section 2.5 we summarized internal wave theory from which followed that the irreversible conversion of internal wave energy is by means of turbulence production and viscous damping.

If the internal wave breaks, a part of its potential and kinetic energy is irreversibly transferred into turbulence. We exploit the observable centred displacement scale  $L_C$  to estimate the loss of IWE by the following assumption.

$L_C$  is twice the typical distance over which fluid parcels irreversibly fall and therefore we assume  $L_C$  is the mean reduction of the wave height of the internal wave group.

Consequently, the loss  $E^{br}$  of the sum in potential and kinetic wave energy (2.4.37) or (3.3.16) reads:

$$E^{br} = L_E L_C \left( 1 - \frac{1}{2} \frac{L_C}{L_E} \right) \left[ N^2 + \frac{1}{2} \left( \frac{dU}{dz} \right)^2 \right], \quad (3.8.4)$$

provided  $L_C \leq L_E$ .

In (3.8.4) we have substituted the Ellison length scale  $L_E$  instead of  $\tilde{L}_E$  defined in (3.3.14) under the assumption  $L_E$  entirely represents wave-induced density fluctuations.

After the loss (3.8.4) of energy, the wave group may gain energy from the main flow and thus create a sequence of breaking waves at time intervals  $\tau_c$  estimated by (3.8.3). Hence, the ensemble averaged effect of this process of growing and breaking waves equals the following (rate of energy) transfer  $T_{i-t}^{br}$  from IWE to TKE, solely by wave breaking:

$$T_{i-t}^{br} = \frac{E^{br}}{\tau_c} = \left\{ \frac{L_E L_C}{\Delta_\theta} \left( 1 - \frac{1}{2} \frac{L_C}{L_E} \right) \left[ N^2 + \frac{1}{2} \left( \frac{dU}{dz} \right)^2 \right] \right\} \cdot \left| \frac{dU}{dz} \right|, \quad (3.8.5)$$

with  $\Delta_\theta = 5-10$  and provided  $L_C \leq L_E$ .

Actually, in (3.8.5) the expression between the brackets  $\{.. \}$  may be interpreted as a lower bound estimate of the net wave-induced shear stress. Here we carefully use the adjective "net" to indicate that there may also exist a wave-induced shear stress. However, in view of the reversible energy transfer between mean flow and waves (Section 2.5) this stress does not contribute to loss of the total energy stored in the mean flow and in the waves.

The net shear stress is necessary to compensate for the loss of IWE by wave breaking.

In addition, microstructure observations provide estimates for the rate of energy dissipation  $\epsilon$ . Consequently, an upper limit of  $L_E$  follows from the inequality:

$$T_{i-t}^{br} < \epsilon. \quad (3.8.6)$$

In (3.8.6) the "<" sign has been applied because the mean strain rate will also directly produce TKE which must be dissipated as well. Substitution of (3.8.6) into (3.8.3), while remembering the definition of the turbulent Froude number (3.5.2), yields:

$$1 < \frac{L_E}{L_C} < \frac{1}{2} + \left( \frac{2 \Delta_\theta Fr_T^3 Ri^{3/2}}{1 + 2 Ri} \right), \quad (3.8.7)$$

with  $\Delta_\theta = 5-10$ .



For  $Ri = 1/4$ ,  $Fr_T = 1$  and  $\Delta_0 = 5$  we find as upper limit for  $(L_E/L_C) \leq 1.3$ . Hence, for the range  $Ri \geq 1/4$ , where stationary internal waves can exist the Ellison scale  $L_E$  may exceed the centred displacement  $L_C$  substantially provided  $Fr_T \geq 1$  and  $\Delta_0 \geq 5$ . Unfortunately, both  $Ri$  as well as  $Fr_T^3$  are overly sensitive to observational errors and this prohibits reliable experimental verification.

We end with the following discussion. For vanishing mean strain rate the gradient Richardson number tends to infinity and so does our upper limit of the ratio  $L_E/L_C$ . However, we must emphasize the restriction made in the introduction to this section: we have limited ourselves to critical layer formation induced by the mean shear flow only.

In view of the definition of  $\alpha$  in (2.6.9) or (3.3.6) we have actually combined three steps in (3.8.3) and (3.8.5). We have combined the probability of exceeding  $\partial \tilde{Z}/\partial z > 1$ , weighted the energy released by breaking and the third step is to estimate the typical cycle period between subsequent wave breaking events. Here we have assumed that the cycle period is proportional to the mean shear ( $dU/dz$ ).

For breaking of surface waves a similar but more thorough analysis has been made, see e.g. (Phillips, 1980, p. 196). For breaking surface waves the Rayleigh distribution of wave maxima is used to compute the probability of exceeding the maximal allowable wave height to weigh the energy released by breaking; in absence of surface drift the mean wave period gives the cycle period.

Similarly, for breaking of internal waves in absence of a dominant shear rate, we should consider wave-wave interactions leading to convection and straining of short waves by orbital motions of longer waves instead of flow-induced critical layer formation. Then the cyclic periodicity tends to become proportional to  $N$  rather than to  $(dU/dz)$ . Therefore, the restriction, mentioned in the introduction to this section about the application of (3.8.5), to not very large Richardson numbers. Presently we do not know the transition  $Ri$  criterion but we based on the wave-wave interaction considerations in Section 2.7 we expect this transitional  $Ri$  number to be much larger than unity.

This concludes the definition of criteria, dimensionless numbers and scales that are observable with the instrumentation used in our field campaign. In this Chapter 3 we have attempted to exploit the theoretical considerations as well as the conceptual basis formulated in Chapter 2. The next Chapter 4 applies the quantities and notion to interpret the finescale timeseries and microprofiles in terms of internal waves, overturning, energy transfer, 3D turbulence etc..

## 4 Analysis of the observations

### 4.1 Reference time, data, sites and measurement procedures

For a clear and brief reference to each measurement, we will abbreviate the start time as a combination of local time (M.E.T.) and Julian day as follows. For example, instead of the local time 12 h 53 min at Julian day 156 1992 (Thursday, June 4, 1992) we write "12:53/156". We will refer to Thursday June 4, 1992 as "day 156" and likewise "day 157" is Friday June 5, 1992. Further, several figures will possess a horizontal time axis in minutes past a certain reference time. For day 156 the reference reads 12:27/156 (747 minutes after midnight) and likewise for day 157 the reference time has been determined at 08:54/157 (534 minutes after midnight).

All finescale and microstructure measurements on day 156 were made simultaneously at approximately the same location in the Rotterdam Waterway. Fig. 1a gives an impression of the vertical finescale in the Rotterdam Waterway at the site. Fig. 1a consists of 15 profiles made with the Elmar instrument deployed from the anchored Rijkswaterstaat vessel "Pavo" measuring the finescale as we defined in Chapter 1. Fig. 1b to 1g show the underlying vertical finescale profiles (see (Uittenbogaard, 1993) for sites, detailed figures including measuring points as well as tables, details of signal correction etc.). During the afternoon of day 156 the increasing flood current is indicated by the increase of  $|U|$  as well as the increase of the density difference ( $\rho - 1000$ ) with time. In addition, the magnitude of  $|U|$  has been given a positive sign for flood currents: after 300 minutes (past reference time) the current along the observed water column was directed landwards i.e. a flood current. Observe that the Richardson number was rather noisy because of its sensitivity to small changes in the velocity and density profiles in particular near a local maximum in the velocity magnitude. Consequently, the Richardson number is quite sensitive to the smoothing applied to the observations.

On day 157 all measurements were made at a nearly fixed location in the stably stratified Caland channel which runs parallel to the Rotterdam Waterway but has smaller currents and larger Richardson numbers compared with our observations on day 156 in the Rotterdam Waterway. Fig. 2a displays an overview of the flow as we observed it through 7 profiles made with the Elmar instrument deployed from the anchored Rijkswaterstaat vessel Pavo. Fig. 2b to 2e show the underlying profiles.

During the morning of day 157 the tidal flow in the top 10 m is directed towards the North Sea. Further, for plotting purposes we have truncated in Fig. 1 and 2 the maximal Richardson number at 10. Finally, the buoyancy frequency  $N$  on day 157 is nearly constant along the part of the water column that we have observed.

Table 1 to 3 summarizes much of our data processing. The ordering in Table 2 and 3 is related to the successful time series finescale observations from the suspended platform, each measurement of essentially ( $u, v, w, \rho$ ) took 30 minutes and the sampling frequency was 20 Hz.



The numbers of the columns in Table 2 and 3 correspond to the intervals of the time series finescale observations which indicated in Fig. 1a and 2b, as well as in other figures, by rectangles.

We emphasize that the signals  $(u, v, w, \rho)$ , which are essential to finescale internal wave observations were obtained by subtracting the platform motions from the measured parameters.

In addition, the fourth row in Table 3 presents the start time of each of the platform tests in minutes past the previously defined reference time. In Fig. 1b to 1g as well as Fig. 2b to 2e the time interval of the vertical finescale measurement is indicated. Those profile numbers are transferred to the sixth row in Table 3 and are used to provide information on the flow during the time series observations were made. The third row in Table 3 contains the depth of the platform below the actual water level. Most of the platform data on day 156 were collected at a depth between 10-12 m whereas on day 157 the platform was positioned at 6 m depth and during one series at 9 m and during another series at 3 m below the actual water level.

A total of 13 measurement series were made with the platform of which 10 were successful. However, 2 series were discarded due to suspected fauling of the instruments in the flood current of the late afternoon on day 156 e.g. sea weed or jelly fish. In addition, a third measurements was expelled because the platform was directionally unstable at currents smaller than 60 mm/s near tidal slack at the end of the morning of day 157.

The microstructure profiles were recorded from the Rijkswaterstaat vessel "Hinder". During a drop of the MicroProfiler the Hinder drifted freely for a distance of approximately 50 m near the anchored vessel Pavo from which the vertical finescale observations were made. Each drop took about 3 minutes with a typical drop velocity of 100 mm/s to a safe depth of about 15 m. As a consequence, a total of 44 drops were successfully made during 6 hours in the afternoon of day 156 and another 18 during 3 hours in the morning of day 157.

## 4.2 Microstructure density profiles combined with vertical finescale stability numbers

With reference to the discussion in Section 3.3 on the upper limit of density gradients, we first consider some microstructure density profiles obtained with the MicroProfiler. In addition, we return to the upper limit estimates of Gibson (1986) and show that his estimates for saturated spectra are too large.

Some example profiles are selected from the data report (Malatt, 1992). Fig. 3a shows a profile (12:51/156) during an increasing flood current in the Rotterdam Waterway whereas Fig. 3b presents the simultaneously observed finescale profiles. In Fig. 3b " $\rho/\rho_0$ " attempts to indicate the relative density defined as  $(\rho - \rho_{\min})/(\rho_{\max} - \rho_{\min})$  with the minimal and maximal densities occurring in that particular profile. In addition, Fig. 3b displays the gradient Richardson number  $Ri$  and the buoyancy frequency  $N$  derived from 3rd order Aussgleich spline fits to the experimental data.

Fig. 3a demonstrates that at a depth of 11.5 m one of the largest overturning events (1.5 m centred displacement scale  $L_c$ ) was recorded (see Fig. 11 and 12). The local Richardson number was about unity at 11.5 m depth.



For later reference to the observation from the platform we note the instant the MicroProfiler during measured the depth of 11.5 m. The drop velocity, averaged over the first 10 m of its vertical path, was about 100 mm/s. Hence, the time of arrival at the breaking wave at 11.5 m was about 12:53/156.

Note, near 10 m depth the steplike structures are shown, which are typical of many microstructure records, not only in this field campaign but also in lakes, seas and oceans. From our observations we conjecture that the density steps are remnants of earlier breaking events or measurement of a strained gradient region and are likely well-mixed pancake-shaped volumes vertically interspersed between layers possessing the stratified density gradient. Unfortunately, the horizontal extend of these well-mixed regions is difficult to assess; each subsequent drop with intervals of 5 to 10 minutes did not reproduce the same step structure.

Fig. 4a is another example of a microstructure density profile, taken at 13:50/156. (in the meantime 4 other drops were made in the interval 12:53-13:50/156). At a depth of about 9 m both sensor groups observed small overturns while the gradient Richardson number was about 1 to 2 (Fig. 4b). Fig. 5 shows the microstructure profile

16:13/156 with an entire staircase of density steps while the finescale flow possessed a  $Ri \geq \frac{1}{4}$  (Fig. 5b). Moreover, the second sensor on the MicroProfiler displays in Fig. 5a a spurious peak which was not observed by its neighbour. Such peaks are expelled from computing the centred displacement scale  $L_C$  defined in Section 3.4 and they are due to contamination.

Finally, Fig. 6a displays the steplike structure in the microstructure profile 16:13/157 taken in the Caland channel at large Richardson numbers of 5 or more (Fig. 6b). Incidentally, the Richardson number is computed according to its precise definition (2.3.3) using the vertical gradients of each of the horizontal and orthogonal velocity components. Hence, the computation of the Richardson number includes the recorded compass reading of the velocity measuring instrument. Fig. 6 is representative of many drops and finescale observations on day 157. Observe in Fig. 6a that sensor no. 1 may have again encountered ramsoms and kept it for a few seconds while its neighbour, sensor 2, only displays a small density spike.

From visual inspection of Figures 3 to 6 we may infer the following. The occurrence of the steplike density structure appears to be independent of the gradient Richardson number derived from finescale observations. Moreover, for most of the records this rules out that the steps originate exclusively from the Kelvin-Helmholtz instabilities of the mean flow. The step like structure is most likely only the result of initial wave straining, K-H billowing, critical layer absorption and the temporary formation of interactions.

#### **4.3 Centred displacement scale, Ellison scale and vertical finescale observations**

Figures 7 and 8 show the density difference  $(\rho-1000)$  kg/m<sup>3</sup> and  $\rho$  has been obtained from the monotonised profiles. In particular, in Fig. 7 the hump in the density profile at about 12 m depth and at 40 minutes past reference time exhibits the large breaking event observed in drop 13:11/156.



The "path" of the suspended platform during each timeseries measurement is indicated by rectangles in these figures and the numbers refer the columns in Table 2 and 3. From these monotonised profiles also follows the buoyancy frequency: its square is shown in Fig. 9a for day 156 and likewise for day 157 in Fig. 10a where  $M^2$  is used to differentiate the buoyancy frequency computed from the monotonized profiles. Until 200 minutes past reference time the fresh water upper layer is practically unstratified to a depth of about 8 m. Fig. 10a (day 157) shows that the bed layer up to a depth of about 15 m is practically unstratified.

Along the path of the platform on day 156 holds  $N=0.12-0.18$  rad/s (Table 1) and correspondingly the minimal periods ( $2\pi/N$ ) were 52 s to 35 s respectively. For day 157 holds along the path of the platform  $N=0.06-0.09$  rad/s (Table 1) with corresponding periods of 105 s and 70 s.

Fig. 9b is composed of 16 vertical finescale profiles measured from the vessel Pavo anchored in the Rotterdam Waterway on day 156, see also Fig. 1 for the average instant of profiling. Typically, for the gradient Richardson number  $Ri=0.4-3.0$  in the stratified layer below 8 m depth whereas  $Ri \approx 0.2 \div 1.0$  in the brackish-fresh water top layer. Despite the smaller buoyancy frequency (Fig. 10a) in the Caland channel on day 157  $Ri=2.0-10.0$ , see Fig. 10b. Occasionally  $Ri$  exceeded our upper limit of 10 used for plotting. With the exception of the first finescale profile on day 157 all other profiles went to 10 m depth while the platform was located at a depth of 6 m.

With reference to Fig. 3.4.1 in Section 3.4, we presented the definition of the centred displacement scale  $L_C(z,t)$  as the displacement averaged over stationary sections in each drop. Fig. 11 exhibits  $L_C$  on day 156 near the anchored Pavo and thus near the suspended platform.

The scale in Fig. 11 is linear in metres and shows that along the trajectory of the platform in this depth-time diagram that  $L_C=0.05-0.20$  m (Table 1). This plot and subsequent plots have been obtained after smoothing with an anisotropic Gaussian filter with widths that differ along the time axis and along the depth direction. Therefore the large overturning event at 12 m depth and 40 minutes past reference time artificially influenced its "region" in this diagram although this large overturning event was only observed in one drop.

For turbulence modelling the reduction of the mixing length, compared with its unstratified counterpart, is of interest. The damping effect of the stratification on  $L_C$ , which we can regard as twice the mixing length, is clearly demonstrated in Fig. 11. On day 156 the stratification was significant at depths exceeding 8 m and there  $L_C$  is reduced to less than 100 mm in the Rotterdam Waterway where the depth was about 18 m.

Alternatively, at a depth of 4 m we frequently see  $L_C=1$  m in Fig. 11 whereas the Bakhmetev profile for the mixing length in an unstratified and steady channel flow would yield:

$$L_{\text{mix}} = \kappa z \left( 1 - \frac{z}{D} \right)^{1/2} \approx 2.7 \quad [\text{m}] \quad (4.3.1)$$

with  $\kappa=0.40$ , depth  $D \approx 18$  m and level  $z=14$  m above the bed.



Hence,  $L_C$  in the unstratified upper layer is smaller than his estimate (4.3.1) for unstratified channel flow. With reference to Fig. 9 it appears that the maximal value for  $L_C$  was observed halfway between the free surface and the level where stratification becomes notable. For instance, Fig. 9 shows during the first 200 minutes past reference time on day 156 that the 8 m depth level acted as the transition between stratified and unstratified water bodies. Fig. 11 gives  $L_C$  maximal at 4 m depth and apparently the transition at 8 m depth acted as an artificial bed. This underestimation of  $L_C$  in the unstratified fresh water layer is an indication that turbulence models of the algebraic type and based on local stability parameters, usually  $Ri$ , cannot predict this  $L_C$ -profile.

After 200 minutes the flood current elevated the stratified-unstratified transition level to about 4 m depth. Correspondingly, also the maximal value of  $L_C$  is now shifted to 2 m depth in Fig. 11 near 300 minutes past reference time.

Fig. 11 provides a further important conclusion, namely that along the trajectory of the platform  $L_C$  was smaller than the smallest observable wavelength of the electromagnetic current meters (EMS) mounted on the suspended platform. The smallest observable wavelength of the EMS was determined by either (i) their size of 40 mm (ii) the roll-off of their frequency response above 10 Hz and (iii) the sampling frequency of 20 Hz in currents of 700 mm/s or less. Consequently, we cannot expect to observe, with the instruments on the suspended platform, turbulent velocity fluctuations belonging to the 3D-turbulence inertial subrange! Hence, the microstructure observations were essential to assess the (turbulent) flow phenomena at wavelengths below 100 mm.

Among many other signals, the conductivity and the temperature were also recorded by the the suspended platform. In addition, these signals were linearly and frequency-dependent corrected for platform motions to obtain the fluctuating density  $\rho'$  uncorrelated with the recorded platform motions. Further, the temperature and the conductivity sensors, installed on the platform, were only suitable to observe finescale density fluctuations in salinity stratified flows.

Per platform measurement of 1800 s duration the rms  $|\rho'|$  is computed from 50% overlapping records, each 410 s (8192 samples/20 Hz) long and  $\rho'$  follows from  $\rho$ , corrected for platform motions, after subtraction of its least square fit over the relevant record. From  $|\rho'|$  follows the Ellison scale defined in Chapter 3 and its value is added to Table 1 and 2.

Along the platform trajectory in the depth-time diagrams also the centred displacement scale  $L_C$  and several state parameters were selected and plotted logarithmical in Fig. 14 for day 156 and day 157 respectively. Unfortunately, the time origins in Fig. 14 are taken at midnight and 746 minutes equals the time 12:26 and 533 minutes the time 8:53. Since the minimal wavelength observable with the electromagnetic current meters was 100 mm Fig. 14 shows that the sensors could not detect 3D-turbulence in the inertial subrange.

Except for the large breaking event (drop 13:11/156) at 12 m depth and 40 minutes past reference time on day 156,  $L_E = (2-10)L_C$ , see Table 2 and 3 (columns 1 to 6 for time series on day 156, columns 7 to 10 for day 157). In Fig. 11 we have added these values for  $L_E$ , derived from the time series. With this Figure 11 the reader may verify that the representative values of  $L_C$  are copied to Table 2 and 3.



Moreover, in anticipation of Section 4.12, we computed in Table 2 an alternative Ellison length scale by means of the integral

$$\int_0^{\infty} (|Q|_{\rho u_1} |Q|_{\rho u_2})^{1/2} df$$

given in Table 3, based on absolute quad spectra and using the one dimensional versions of (3.2.5) and (3.2.6). This estimate resembles better the wave-induced density variations than  $L_E$  derived from  $\langle \rho'^2 \rangle$  directly. Nevertheless, both estimates for the rms internal wave height are (much) larger than the centred displacement scale. Inspection of columns 7 to 10 in Table 2 show that for day 157 the ratio  $L_E/L_C$  is even larger and ranges from 15 to 30. Thus the wave-detectability parameter  $W$  (3.7.3) is larger than unity, except for the timeseries 16:15/156, and we may expect to detect internal gravity waves. The parameter  $W$  in Table 2 and 3 is computed by means of  $L_E$  based on the density variances observed in time series. In Section 4.12 we will exploit more detailed signatures of (linear) internal waves.

In Section 2.6, eq. (2.6.5) and (2.6.9) we defined  $\alpha$  as the ratio between the rms slope of wave-induced density isolines and the mean vertical density gradient. Using the parameters developed in Section 3.3, we can now estimate  $\alpha$  and  $c$ , the latter has been defined in (3.3.5) and related to the assumed shape of the vertical displacement spectrum (3.3.6). The uncertainty in estimating  $\alpha$  lies primarily in the assessment of the largest vertical wavelength  $H$  of random internal waves. Based on the vertical finescale observations in the Rotterdam Waterway (Fig. 1a to 1g) we estimate  $H \approx 8$  m and mainly from the microstructure recordings in the Caland channel we infer  $H \approx 15$  m. We believe that the product  $(\alpha H)$  is more reliable than  $\alpha$  itself. Table 2 summarizes the results; bluntly averaging over all successful platform measurements (see Table 1) indicates  $\alpha \approx 0.45$  with a large range of variability, although  $\alpha < 1$ , there are two cases where  $\alpha$  approaches 0.7. For  $\alpha \approx 0.45$  and assuming a strictly sinusoidal density perturbation, the instantaneous vertical density gradient  $\partial \rho / \partial z$  would not become positive and could induce gravitational overturning. This last conjecture comes from the comparison of the standing and breaking wave experiments of Orlanski (1972) which we summarized in Section 2.6. There we found  $\alpha = \mu / \sqrt{2} \leq 0.45$  in (2.6.5) which is indeed in the range of the values for  $\alpha$  we derived from our field observations. The similarity between  $\alpha$  derived from Orlanski's experiments and our results is a rather fortunate coincidence. Earlier, we have argued that the product  $(\alpha H)$  is more reliable than  $\alpha$  itself because for the latter we must assess the stratified layer thickness  $H$  and that is a rather crude and subjective procedure.

Related to our assessments of  $\alpha$  we close this section with a discussion. Now the following discussion is devoted to the relatively large value of  $\alpha$ , with  $\alpha \gg 1$ , that we derived from Gibson (1986) and given below (3.3.11). For the latter we have used linear internal wave theory to convert the strain rate spectrum into one for density variance. Nonlinear effects, expected near internal wave saturation (Gibson, 1994, personal communication), may provide arguments to explain our much lower estimates for  $\alpha$  than those derived from the shear spectrum (3.3.11). Incidentally, our derivation of  $\alpha$  from the Ellison length scale observed in time series did not rely on linear theory but, on the other hand, required an assumed  $m^{-3}$  vertical wavenumber spectrum for the wave-induced density variance as well as a typical stratified layer thickness  $H$ .

We obtained the values for  $\alpha$ , summarized in Table 1 and 2, from our Eulerian finescale time series i.e. with reference to horizontal rather than vertical density fluctuations.

Besides the nonlinear effects not accounted for, there may be another explanation for large values of  $\alpha$  when derived from vertical velocity shear profiles. Our explanation is based on the microstructure recordings of the step like structure that we mentioned in Section 4.2.

Consider the schematic density profile in Fig. 4.3.1 which, by definition, does not exhibit overturns. In principle we can obtain such a vertical density profile after spatially low-pass filtering of the microstructure density profile  $\rho(z)$  with a variable vertical wavelength cut-off at about  $L_C(z)$  to create the output  $\rho(z;L_C)$ . In accordance with the definition of centred displacement scale, it is unlikely that the filtered profile  $\rho(z;L_C)$  exhibits "on the average" overturns. Consequently, such a smoothed density profile and its associated gradient profile would be similar to the schematic one given in Fig. 4.3.1. Yet we can derive from this profile values for  $\alpha > 1$  which erroneously would infer breaking internal waves.

We show this as follows. In the well-mixed intersections of Fig. 4.3.1 we have  $\partial\rho(z;L_C)/\partial z=0$  and in between  $\partial\rho(z;L_C)/\partial z=-|r|$  with some constant  $r$ ; its magnitude is irrelevant in the following. If the fraction  $\delta$ , ( $0 \leq \delta \leq 1$ ), of this profile would belong to the well-mixed intersections then, with reference to (2.6.9), it is straightforward to compute:

$$\alpha^2 = \frac{\delta}{1-\delta} \quad \text{for } \alpha \text{ in } \left| \frac{\partial \bar{\rho}}{\partial z} \right| = \alpha \left| \left\langle \frac{\partial \rho}{\partial z} \right\rangle \right|. \quad (4.3.2)$$

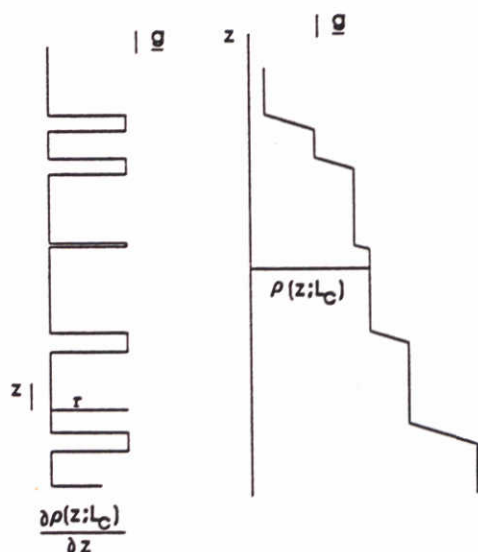


Fig. 4.3.1 A schematic spatial low-pass filtered, steplike density profile with its vertical gradient.

Hence, if more than 50% of the stratified water column consists of well mixed intersections then  $\alpha > 1$ . Nevertheless, by definition of  $L_C$  and the low-pass filtering of  $\rho(z)$  we made it unlikely that the density gradient  $\partial\rho(z;L_C)/\partial z$  becomes positive (overturns). Reversely, this implies that if a ratio  $\alpha > 1$  has been observed in a range of wavelengths well above the centred displacement scale  $L_C$  then this ratio  $\alpha$  may belong to profiles such as shown in Figures 3 to 6.



Incidentally, in (4.2.2) we have exploited the observation of the temperature gradient spectra against vertical wavenumber  $m$  proportional to  $m^{-1}$  in range of relatively large wavelengths exceeding the Ozmidov length scale. Thus the next question may be whether the observed spectra as a function of the vertical wavenumber  $m$  are equally influenced by the step like structures? The schematic jumps of  $\partial\rho(z;L_c)/\partial z$  with random duration resemble the so-called random telegraph signal (Papoulis, 1965, p. 290) and its autocorrelation decreases exponentially with separation in  $z$ -direction so that for large enough vertical wavenumbers  $m$  the power energy density spectrum of the block shaped  $\partial\rho(z;L_c)/\partial z$  decreases proportional to  $m^{-2}$  (Papoulis, 1965, p.341) and (V.d. Boogaard, 1994). Thus, fortunately, the energy density spectrum of random density gradient blocks produce a spectrum that decreases faster than the  $m^{-1}$  of wave-induced vertical density gradient.

## 4.4 Dimensionless numbers

In this section we verify by means of several dimensionless numbers derived from microscale observations, whether the high Reynolds number  $q^2$ - $\epsilon$  turbulence models is applicable.

As we argued in Section 3.5, the existence of an inertial subrange of 3D turbulence depends on the turbulence Reynolds number  $Re_T$  and the small-scale Froude number  $Fr_\gamma$ . For convenience, their definition is repeated below together with the definition of the turbulence Froude number  $Fr_T$ :

$$Re_T = \left( \frac{L_c}{L_K} \right)^{4/3} ; Fr_\gamma = \left( \frac{L_o}{L_K} \right)^{2/3} ; Fr_T = \left( \frac{L_o}{L_c} \right)^{2/3} . \quad (4.4.1)$$

The numbers in (4.4.1) are obtained by, among others, estimates for the energy dissipation rate  $\epsilon$  and centred displacement scale  $L_c$ .

Fig. 15 and 16 show for day 156 that both  $Re_T$  as well as  $Fr_\gamma$  ( $Fr_g$  in the figures) are large enough to expect an ordering of scales below  $L_c$ . Moreover, Fig. 17 shows that the turbulence Froude number  $Fr_T$  was about 1 in the stratified flow. In accordance to (4.4.1), this implies that  $L_c$  equals the large-scale buoyancy limit of the inertial subrange and the turbulence was active. For the flow recorded by drops on day 157 in the Caland channel,  $L_c$  appears to be about  $L_o$  in the first 6 m below the free surface (Fig. 20).

Hence, this indicates that both in the Rotterdam Waterway as well as in the Caland channel during our observations  $L_c/L_o$  is about unity at levels where the gradient Richardson numbers exceeds unity.

We conclude from these numbers that the turbulence at our sites is active and possesses a well-developed range of scales probably on the inertial subrange. Hence, we may apply the high Reynolds number  $q^2$ - $\epsilon$  turbulence model.

Before we go into the matter of internal waves, we are interested in the performance of the  $q^2$ - $\epsilon$  turbulence model in predicting, among other parameters, the eddy diffusivity. This is the subject of the next two Sections 4.5 and 4.6. Here we shall check whether the turbulence conditions are suitable for the application of the  $q^2$ - $\epsilon$  turbulence model. In addition, the small-scale Froude number is large enough so that there is not a direct effect of the buoyancy on the energy cascade within the inertial subrange of 3D turbulence.



This implies the important assertion that buoyancy in the  $\epsilon$ -equation should not be incorporated. The next Section 4.5 continues to inspect the results from the turbulence modelling point of view.

## 4.5 Energy dissipation rate and eddy diffusivity derived from microstructure profiles

For validation of turbulence models, applied to the stratified tidal flow in the Rotterdam Waterway Estuary, the centred displacement scale  $L_C$ , the rate of energy dissipation  $\epsilon$  and the eddy diffusivity are essential. In Section 4.3 we have already indicated the strong suppression of the mixing length in comparison with the unstratified estimate.

Further, in the previous Section 4.4 we concluded the following. The turbulence Reynolds number and the small-scale Froude number indicate that the rate of viscous dissipation  $\epsilon$ , derived from fits to the so-called Batchelor spectrum for the temperature gradient, has been obtained with the correct estimator. Section 3.6 and the references therein give more information on the estimator for  $\epsilon$  and the procedure to obtain the eddy diffusivity.

Next, we continue to interpret the estimates for rate of energy dissipation and for the eddy diffusivity. On a log-scale Fig. 21 displays  $\epsilon$  in  $\text{m}^2/\text{s}^3$  for day 156. The reader may appreciate the following translation of  $\epsilon$  into the Kolmogoroff length scale  $L_K = (\nu^3/\epsilon)^{1/4}$  with kinematic viscosity of water  $\nu = 10^{-6} \text{ m}^2/\text{s}$ : if  $\epsilon = 10^{-6} \text{ m}^2/\text{s}^3$  then  $L_K = 1 \text{ mm}$  whereas if  $\epsilon = 10^{-4} \text{ m}^2/\text{s}^3$  then  $L_K = 0.5 \text{ mm}$ . The observed relatively large values of  $\epsilon$  imply a very turbulent flow. The resolved estimate for  $\epsilon$  about  $10^{-4} \text{ m}^2/\text{s}^3$  approaches the observation limit owing to the response time of the thermistors.

Despite the rather vigorous viscous energy dissipation, the eddy diffusivity on day 156 in the stratified region at the depth of 10 m remains very small, namely about 10 to 30  $\text{mm}^2/\text{s}$  (see Fig. 22 where "ez" equals the eddy diffusivity  $\Gamma_T$  defined in Section 3.6). This low value for the eddy diffusivity is due to the limited centred displacement scale  $L_C$  of the order of several centimetres instead of meters. Typically, an eddy diffusivity of about  $1 \cdot 10^{-4} \text{ m}^2/\text{s}$  (100  $\text{mm}^2/\text{s}$ ) is observed in the logarithmic boundary layer of laboratory channel flows at a mean velocity comparable with the velocity in the Rotterdam Waterway, see e.g. (Uittenboogaard, 1986). In contrast, in the unstratified region near the free surface, Fig. 22 shows an eddy diffusivity of about 1000  $\text{mm}^2/\text{s}$  and is typically two orders of magnitude larger than in the deeper and more stratified region.

From the estimates for  $\epsilon$  (Fig. 21) and using the observed mean strain rate  $\langle \partial u / \partial z \rangle$  we can assess the turbulent shear stress assuming local equilibrium of turbulent kinetic energy:

$$R_{xz} \leq \frac{\epsilon}{\left| \left\langle \frac{\partial u}{\partial z} \right\rangle \right|} ; R_{xz} \leq 50 \text{ mm}^2/\text{s}^2 . \quad (4.5.1)$$

In (4.5.1) fluxes due to diffusion, advection and buoyancy have been neglected. We have computed the upper limit of 50  $\text{mm}^2/\text{s}^2$  in (4.5.1) for  $\epsilon \leq 1 \cdot 10^{-5} \text{ m}^2/\text{s}^3$  and an observed mean strain rate  $\langle \partial u / \partial z \rangle \approx 0.2 \text{ s}^{-1}$ . We may compare this result with the bed shear stress  $R_{bed}$  using a Chézy coefficient of 60  $\text{m}^{1/2}/\text{s}$  and a typical velocity of 500  $\text{mm}/\text{s}$  to obtain:



$$R_{bed} \approx \frac{g}{C^2} |U|^2 ; R_{bed} \approx 700 \text{ mm}^2/\text{s}^2 \quad (4.5.2)$$

If the flow were unstratified and steady then halfway the water depth  $R_{xz} \approx \frac{1}{2}R_{bed}$  would have been observed (Nezu and Rodi, 1986) whereas the estimated shear stress (4.5.1) in the stratified region is one order of magnitude smaller than the bed stress (4.5.2). A similar comparison between the investigated stratified tidal flow and an unstratified steady channel flow can be made for  $\epsilon$ . For an unstratified and steady channel flow with a logarithmic velocity profile holds

$$\epsilon = \frac{\kappa R_{bed}^{3/2}}{z} \approx 1.10^{-5} \text{ m}^2/\text{s}^3 \quad (4.5.3)$$

for Von Kármán's constant  $\kappa \approx 0.4$ ,  $z = 10 \text{ m}$  upwards from the bed and  $R_{bed}$  given by (4.5.2). Remarkably, the unstratified estimate (4.5.3) for  $\epsilon$  is of the same order of magnitude as  $\epsilon$  in the stratified region of Fig. 21. This comparison amplifies our previous statement that according to  $\epsilon$  the flow is very turbulent. Consequently, the strong reduction in centred displacement scales under stratification at  $Ri \approx 0.5-2$  in the Rotterdam Waterway appear to be responsible for the small eddy diffusivity.

According to Fig. 23 on day 157 in the Caland channel the rate of energy dissipation was  $\epsilon$  about  $1.10^{-8} \text{ m}^2/\text{s}^3$  and is two to three orders of magnitude smaller than at our Rotterdam Waterway site on day 156. Consequently, the Kolmogoroff length scale  $L_K$  was 1 to 5 mm at the Caland channel site. Further, the eddy diffusivity is only about  $10 \text{ mm}^2/\text{s}$  at the depth of 6 m of most of the platform observations on day 157. However, the rate of energy dissipation values of this stratified tidal flow were similar to an unstratified flow.

We noted before that the energy dissipation rate in the Caland channel is two orders of magnitude smaller than in the Rotterdam Waterway. Hence, either the internal waves in the Caland channel were less energetic than those in the Rotterdam Waterway or the comparatively small mean strain rate in the Caland channel promotes less frequently critical layer formation and wave breaking than the Rotterdam Waterway. We will come back to this subject, the essence of this report, after the actual analysis and quantification of IWE.

## 4.6 Indications of the performance of the $q^2$ - $\epsilon$ turbulence model

In Chapter 1, under the subtitle "Essential points of view taken in this study", we promised the following. We will use microscale measurements instead of numerical simulations as input to a one-dimensional and vertical (1DV) version of the complete  $q^2$ - $\epsilon$  turbulence model, the latter is implemented in TRISULA of DELFT HYDRAULICS (Uittenbogaard et al., 1992).

In the following we will and must omit advection as well as the horizontal derivatives in the contribution to the mean strain rate. This neglect, therefore, slightly weakens our validation into "indications" of the performance of the  $q^2$ - $\epsilon$  turbulence model. On the other hand, the sites in the Rotterdam Waterway Estuary were selected to avoid as much as possible the topographic generation of internal waves and of internal wakes. In the flow direction several kilometres of smooth bed were available so that it would be difficult to argue that horizontal derivatives and/or advection of turbulence played a dominant role in our observations.



We have chosen the  $q^2$ - $\epsilon$  turbulence model for the following reasons. In Chapter 1 we argued that turbulence models of the eddy viscosity/diffusivity type are feasible for large scale computations. Moreover, of the classes of eddy-viscosity type turbulence models the  $q^2$ - $\epsilon$  model is the best objective model in the sense that it does not use case-calibrated damping functions and/or a case-calibrated formulation for the mixing length. Instead, the  $q^2$ - $\epsilon$  turbulence model contains coefficients calibrated against experiments with simple geometries and recently the coefficients were extensively checked against DNS (Rodi and Mansour, 1993).

Nevertheless, in the  $q^2$ - $\epsilon$  model there are at least two coefficients that may be subjected to changes for stably stratified flows. Later, in Section 4.7, we will pay attention to these particular coefficients. Now we will present the 1DV version of the high-Reynolds-number  $q^2$ - $\epsilon$  turbulence model. With reference to Fig. 15 and 19 we concluded in Section 4.4 that the high-Reynolds-number turbulence models are in principle applicable to the tidal stratified flow under investigation. However, the 1DV version only retains vertical gradients and the partial time derivative, the latter is used here as a convenient iteration step towards a (quasi) steady state.

Consequently, the 1DV version of the model for the  $q^2$ -equation (2.2.32) reads

$$\frac{\partial q^2}{\partial t} = \frac{\partial}{\partial z} \left\{ \left( v_a + \frac{v_T}{\sigma_k} \right) \frac{\partial q^2}{\partial z} \right\} + P - \epsilon - B, \quad (4.6.1)$$

$$\text{with } v_T = c_\mu \frac{q^4}{\epsilon}; \quad P = v_T \left[ \left\langle \left( \frac{\partial u}{\partial z} \right)^2 \right\rangle + \left\langle \left( \frac{\partial v}{\partial z} \right)^2 \right\rangle \right]; \quad B = \frac{v_T}{\sigma_\rho} N^2.$$

In comparison with (2.2.32), the Reynolds shear stresses appearing in the production term  $P$  in equation (4.6.1) are expressed in the mean strain rate using the eddy viscosity  $\nu_T$ . Further, the first term in the RHS of (4.6.1) represents the diffusion of turbulence by its own advective and pressure fluctuations. Hence, the diffusion term has been modelled by Launder and Spalding (1974) by an eddy diffusivity which actually equals the eddy viscosity,  $\sigma_k = 1$ , see below the summary (4.6.3) of the model coefficients. To this diffusion of TKE we have added an artificial contribution  $v_a$  to slightly smooth the results while conserving TKE. The 1DV version of the model equation for transport of the rate energy of dissipation is similar to (4.6.1) and it reads:

$$\frac{\partial \epsilon}{\partial t} = \frac{\partial}{\partial z} \left\{ \left( v_a + \frac{v_T}{\sigma_\epsilon} \right) \frac{\partial \epsilon}{\partial z} \right\} + P_\epsilon - B_\epsilon - \epsilon_\epsilon, \quad (4.6.2)$$

$$\text{with } P_\epsilon = c_{1\epsilon} \left( \frac{\epsilon}{q^2} \right) P; \quad B_\epsilon = c_{1\epsilon} \left( \frac{\epsilon}{q^2} \right) (1 - c_{3\epsilon}) B; \quad \epsilon_\epsilon = c_{2\epsilon} \left( \frac{\epsilon}{q^2} \right) \epsilon.$$

Observe the "scaling" of the source, sink and buoyancy terms in (4.6.2) by  $(\epsilon/q^2)$  times the equivalent terms in (4.6.1) and the introduction of additional calibration coefficients. We took the standard series of model coefficients as follows (Launder and Spalding, 1974):

$$c_\mu = 0.09; \quad \sigma_q = 1.0; \quad \sigma_\rho = 0.7; \quad \sigma_\epsilon = 1.3; \quad c_{1\epsilon} = 1.44; \quad c_{2\epsilon} = 1.92; \quad c_{3\epsilon} = 1.0. \quad (4.6.3)$$

We refer to (Rodi and Mansour, 1993) for a motivation that these values are optimal choices. The boundary conditions for  $q^2$  and for  $\epsilon$  at the free surface are as prescribed in (Uittenboogaard et al., 1992) for 3D computations without significant influence of wind:



$$\frac{\partial q^2}{\partial z} \Big|_{z=D} = 0 ; \quad \epsilon(D - \frac{1}{2} \Delta z, t) = \frac{q^{3/2}(D - \frac{1}{2} \Delta z, t - \Delta t)}{\kappa(D - \frac{1}{2} \Delta z)}, \quad (4.6.4)$$

where  $z=D$  is the free surface.

The homogeneous Neumann condition for  $q^2$  prevents unphysical transfer of  $q^2$  through the free surface. The mixing length, on which the  $q^2$ - $\epsilon$  turbulence model is based, reads

$$L_{\text{mix}} = c_\mu^{3/4} \frac{q}{\epsilon}. \quad (4.6.5)$$

The second condition in (4.6.4) couples  $\epsilon$  to  $q^2$  with the purpose to force  $L_{\text{mix}}$ , defined in (4.6.5), to be proportional with distance  $\frac{1}{2}\Delta z$  below the free surface where the first level of  $q^2$  and  $\epsilon$  is defined. The time lag in this near surface condition for  $\epsilon$  is within the resolution of the time integration.

In absence of measurements near the bed and its roughness, the original bed conditions are replaced by the following artificial conditions at the lowest computational point  $z=z_1$

$$q^2(z_1, t) = q^2(z_1 + \Delta z, t - \Delta t) ; \quad \epsilon(z_1, t) = \epsilon(z_1 + \Delta z, t - \Delta t) \quad (4.6.6)$$

which resembles downward propagation of  $\epsilon$  and of  $q^2$  with vertical velocity  $\Delta z/\Delta t$ . In the limit of integrating (4.6.1) and (4.6.2), the conditions (4.6.6) correspond to the homogeneous Neumann condition. Because the set of partial differential equations is non-linear the effectively two-sided application of homogeneous Neumann conditions still appear to produce unique solutions, independent of the initial conditions. However, we don not have a mathematical proof for this assertion.

This set of equations was solved on a possibly non-equidistant mesh with  $u$ ,  $q^2$ ,  $\epsilon$  and  $\rho$  defined in the centre point of vertical grid boxes. The equations were transformed into  $\sigma$  coordinates i.e. scaling of  $z$  by the total computational height. The time integration is performed with the  $\Theta$ -method but usually  $\Theta=1$  was set i.e. Euler implicit. For each of the 22 profiles the input, in terms of  $u(z)$ ,  $v(z)$  and of  $\rho(z)$ , was provided by 3rd-order Aussgleich-spline fits to the vertical finescale observations such as shown in Fig. 3b to 6b. Despite the smoothing of the measured profiles the splines still produced short-wavelength oscillations in their first-order and their second-order derivatives. Consequently, these variations resulted in small amplitude oscillations of  $q^2$  and of  $\epsilon$ . These small-scale variations were removed by adding the artificial diffusivity  $\nu_a = 10^{-4} \text{ m}^2/\text{s}$  solely to the diffusion terms in (4.6.1) and (4.6.2). Apart from the removal of the oscillations the results did not change.

A total of 40 or 80 equidistant layers were applied and we investigated the sensitivity of  $q^2$ ,  $\epsilon$  etc. to the number of layers and to the time step. In particular, we checked the sensitivity to the artificial conditions (4.6.6). Instead of (4.6.6) we also applied several variants of bed boundary conditions corresponding to a logarithmic boundary layer flow over a rough bed. Apart from the two or three lowest levels of grid points the results were shown to independent of a fair choice of boundary conditions at level  $z=z_1$ . This observation is similar to computations of the stratified mixing layer (Simonin et al., 1989). We have found that under strong stratification the contribution of diffusion of turbulence from the bed upwards were insignificant. Hence, (4.6.6) appeared to be as good as the alternative conditions for this stratified flow and the measured profiles.



However, (4.6.6) did not create irrelevant local maxima or minima near the lowest computational levels and was therefore selected for the final computations, which we will present below.

The computations which we will present were made with 40 equidistant layers and a time step of one minute. Further to ensure good convergence, 200 time steps were taken. However, this equivalent 200 minutes is not representative for the typical timescale of adjustment of the  $q^2$ - $\epsilon$  turbulence model to gradual changes in flow conditions. Incidentally, the artificial condition (4.6.6) would be equivalent with a downward transport velocity of 4 mm/s for 10 meters of computed water column.

Figures 25 to 28 display the results, in terms of  $L_{\text{mix}}$  defined in (4.6.5) and of  $\epsilon$ , obtained with the previously described diagnostic 1DV  $q^2$ - $\epsilon$  turbulence model. To our opinion these two output parameters allow a fair comparison with the equivalent parameters derived from the microstructure observations. For that matter we refer to Figures 12 and 13 for the centred displacement scale  $L_C$  and for the estimates of  $\epsilon$  to Figures 21 and 23. The computational results in Fig. 25 to 28 have been smoothed and plotted logarithmical at CWR in a similar way as the field observations. Given the simplifications to obtain the 1DV  $q^2$ - $\epsilon$  turbulence model obtained results comparable to the field data within a factor of 10. However, comparing Fig. 12 with Fig. 25 immediately reveals that  $L_{\text{mix}}$  is about 1 mm or even less. Hence,  $L_{\text{mix}}$  is two orders of magnitude smaller than the observed  $L_C$  in the Rotterdam Waterway, likewise for the Caland channel (Fig. 13 and Fig. 27). A similar underestimation of the rate of energy dissipation  $\epsilon$  is observed when comparing Fig. 21 with Fig. 26 for the Rotterdam Waterway. Slightly better, however still underestimated, is the computed dissipation rate  $\epsilon$  (Fig. 28) with respect to  $\epsilon$  estimated from microstructure observations in the Caland channel (Fig. 23). The previous comparison between the estimates from the field and from the computations shows that during all our observations at the two sites the  $q^2$ - $\epsilon$  turbulence model underestimates the typical turbulence intensity characteristics. Hence, it is unlikely that the neglect of advection would have increased the computed turbulence state (always) by at least one order and usually two orders of magnitude.

#### 4.7 Discussion on two model coefficients in the $q^2$ - $\epsilon$ turbulence model

For stably stratified flows the values of the two coefficients  $\sigma_\rho$  and  $c_{3\epsilon}$  are disputable. Below we comment on these coefficients and we start with  $c_{3\epsilon}$ .

##### *The buoyancy coefficient $c_{3\epsilon}$ in the $\epsilon$ equation*

The value of the model coefficient  $c_{3\epsilon}$  is disputable if the  $q^2$ - $\epsilon$  model is applied to stably stratified flows. For instance, if we put  $c_{3\epsilon} = 1.0$  in (4.6.2) then we actually assume that buoyancy does not reduce the dissipation forming shear rates in the high wavenumber part of the 3D turbulence inertial subrange. With reference to Section 3.4 a significant influence of the buoyancy on the strain rates in the inertial subrange is expressed by small values ( $\leq 5$ ) of the small-scale Froude number  $Fr_\gamma$  defined by (4.4.1). Actually, these arguments form the basis Gibson's derivation which we repeated in Sections 3.4 and in Appendix A.



Moreover, with reference to Fig. 16 and 19 we have concluded in Section 4.4 that in the present terminology  $c_{3\epsilon}$  should be unity. Instead, we also ran the 1DV  $q^2$ - $\epsilon$  turbulence model with  $c_{3\epsilon}=0.5$ .

However, the results did not improve, actually, in some less stratified regions  $\epsilon$  decreased by a factor of about 3 and in severely stratified locations  $\epsilon$  became zero and created real number underflow. In particular, the gradually ascending  $10^{-8} \text{ m}^2/\text{s}^3$  line in Fig. 26 obtained with  $c_{3\epsilon}=1.0$  was reproduced for  $c_{3\epsilon}=0.5$ . This result can be explained by the following argumentation. In locations of strong stratification the difference (P-B) between turbulence production P by the mean flow and the buoyancy flux B is negative. Hence, a decrease in  $\epsilon$  will only enhance the magnitude of this negative difference and decreased the computed  $q^2$  even more.

#### *The turbulent Prandtl/Schmidt number $\sigma_\rho$ in the $q^2$ equation*

The ratio between the mixing of mass and the mixing of momentum, especially along the vertical direction, is a point of discussion and of controversy. For instance, turbulence models of the algebraic type, also called zero-equation models, assume the dependence  $\sigma_\rho = \sigma_\rho(\text{Ri})$ . The functional dependence of  $\sigma_\rho$  on the gradient Richardson number Ri is made such that with increasing Ri  $\sigma_\rho$  also increases by using some "damping" functions F(Ri) and G(Ri) for eddy viscosity and eddy diffusivity respectively. The damping functions F(Ri) and G(Ri) are usually based on the discussion presented in Section 2.3, see among others Karels (1974) for a review of damping functions. On one hand, the large scatter in the observed damping effect of Ri on mixing as well as the variety of proposals for the damping functions F(Ri) and G(Ri) indicate a lack of universality. On the other hand, the small and therefore poorly detectable values of mixing parameters may significantly contribute to the scatter.

Based on (Uittenbogaard and Baron, 1989) we will present our arguments for an increase of  $\sigma_\rho$  in the  $q^2$  equation with increasing stratification conditions. It must be pointed out that our review on wave-induced momentum and on wave-induced buoyancy fluxes in Chapter 2 does not directly apply here to motivate changes of  $\sigma_\rho$  in the transport equation (4.6.1) for turbulent kinetic energy. However, some arguments were discussed in Section 2.7 where turbulence-like wave-wave interactions may diffuse momentum without mixing of mass. Based on solely the mean wave-induced strain rate (3.3.9), i.e. without wave breaking, we should add the following transfer term  $T_{i-t}^Y$  of IWE to TKE to the  $q^2$  equation:

$$T_{i-t}^Y = \text{def} = \langle \tilde{\mathbf{R}} : \tilde{\mathbf{d}} \rangle, \quad (4.7.1)$$

with  $\tilde{\mathbf{R}}$  the wave-induced Reynolds stress tensor and  $\tilde{\mathbf{d}}$  the wave-induced strain rate tensor. Similar expression can be found in (Finnigan and Einaudi, 1981). In addition, by introducing an internal-wave related and effective eddy viscosity  $\tilde{\nu}_T$  we may formulate (4.7.1) as:

$$T_{i-t}^Y = 2 \tilde{\nu}_T \langle \tilde{\mathbf{d}} : \tilde{\mathbf{d}} \rangle = 2 \tilde{\nu}_T \langle \tilde{\gamma}^2 \rangle \equiv \tilde{\nu}_T \alpha^2 N^2. \quad (4.7.2)$$

For the last step of (4.7.2) we have substituted (3.3.9). The transfer term  $T_{i-t}^Y$  is similar to the buoyancy term B in (4.6.1). If the wave-induced strain rates vary slow enough in comparison with the most energetic turbulent eddies then  $\tilde{\nu}_T = \nu_T$  else  $\tilde{\nu}_T < \nu_T$ . The turbulence Froude number  $\text{Fr}_T$  in (4.4.1) is indicative for the following ratio between the relevant frequencies:



$$\frac{\text{turbulence freq.}}{\text{int. wave freq.}} = \frac{1}{N} \left( \frac{\epsilon}{L_C} \right)^{1/3} = \left( \frac{L_R}{L_C} \right)^{2/3} = Fr_T. \quad (4.7.3)$$

For the range of depths with significant stratification, we have estimated from Fig. 17 and 20 that  $Fr_T = 0.2-5$ . Hence, (4.7.3) shows comparable time scales of turbulence and of internal wave motions and for internal waves with intrinsic frequency close to  $N$  thus it is likely that  $\tilde{\nu}_T < \nu_T$ . However, for internal waves near the critical layer  $|\Theta| \rightarrow 90^\circ$  and the intrinsic frequency ( $N \cos \Theta$ ) tends to zero so that  $\tilde{\nu}_T \approx \nu_T$ . Moreover, near a critical layer the wave-induced strain rate is maximal and this would suggest  $\tilde{\nu}_T = \nu_T$  which we will apply in (4.7.2).

Next, we continue with the influence of the energy transfer flux  $T_{i \rightarrow t}^y$  from internal wave energy towards turbulence. Subtracting  $T_{i \rightarrow t}^y$  from the buoyancy term  $B$  in (4.6.1) results in an effective buoyancy flux  $B_{\text{eff}}$  and effective Prandtl/Schmidt number  $\sigma_{\text{eff}}$  defined as:

$$B - T_{i \rightarrow t}^y = B_{\text{eff}} = \frac{\nu_T}{\sigma_{\text{eff}}} N^2 \quad (4.7.4)$$

By virtue of (4.7.2) and of (4.7.4) the effective turbulent Prandtl/Schmidt number  $\sigma_{\text{eff}}$  thus reads

$$\sigma_{\text{eff}} = \frac{\sigma_\rho}{\left[ 1 - \sigma_\rho \alpha^2 \left( \frac{\tilde{\nu}_T}{\nu_T} \right) \right]} \leq \frac{\sigma_\rho}{1 - \sigma_\rho \alpha^2}. \quad (4.7.5)$$

Simply averaging  $\alpha^2$ , with the mean  $\alpha$  given in Table 1, for both sites at all times yields  $\alpha^2 \approx 0.2$  and thus  $(\sigma_{\text{eff}}/\sigma_\rho) \leq 1.2$  for  $\sigma_\rho = 0.7$ . Accordingly, we effectively increased  $\sigma_\rho$  in the  $q^2$ - $\epsilon$  turbulence model to  $\sigma_\rho = 1.5$  which is an overestimation for  $\sigma_{\text{eff}}/\sigma_\rho \leq 1.2$ . However, this did improve the model results notably. Incidentally, (4.7.5) shows with  $\tilde{\nu}_T = \nu_T$  that only if  $\alpha \rightarrow \sigma_\rho^{-1/2}$  and  $\sigma_\rho \approx 5$  the effective turbulent Prandtl/Schmidt number  $\sigma_{\text{eff}}$  tends to infinity and this tendency would effectively yield the turbulence state belonging to an unstratified flow i.e.  $B_{\text{eff}} = 0$ . From the previous point of view  $\alpha$  is a rather dominant parameter for the turbulence intensity computed with the  $q^2$ - $\epsilon$  turbulence model. On the other hand, wave breaking will prevent  $\alpha^2$  to become unity so that the effective Prandtl/Schmidt number is barely increased.

### Conclusions

From the diagnostic 1DV simulations with the  $q^2$ - $\epsilon$  turbulence model with vertical finescale observations as input we infer the following. Within a fair variation of the turbulence model coefficients  $c_{3\epsilon}$  and  $\sigma_\rho$  we were not able to increase the computed  $L_{\text{mix}}$  and  $\epsilon$  to the observed magnitudes. In the adjustment of  $\sigma_\rho$  we only took into account the transfer of energy from waves to turbulence  $T_{i \rightarrow t}^y$  induced by wave-induced strain rates alone. In addition, we overestimated this transfer by taking the maximal eddy viscosity  $\tilde{\nu}_T = \nu_T$  but this did not increased the computed turbulence level.

In our opinion the remaining source of turbulence production, not yet accounted for, is internal wave breaking as well as the horizontal strain rate induced by (quasi) 2D-turbulence (circulation). In the next section we will estimate the contribution from wave breaking.



## 4.8 Transfer of wave energy to turbulence by wave breaking

In Section 3.8 we have derived the following rate of energy transfer  $T_{i-t}^{br}$  from internal waves to turbulence by critical layer formation due to the mean shear rate ( $dU/dz$ ):

$$T_{i-t}^{br} = \frac{L_o}{\tau_c} = \left\{ \frac{L_E L_C}{\Delta_\theta} \left( 1 - \frac{1}{2} \frac{L_C}{L_E} \right) \left[ N^2 + \frac{1}{2} \left( \frac{dU}{dz} \right)^2 \right] \right\} \cdot \left| \frac{dU}{dz} \right|, \quad (4.8.1)$$

with  $\Delta_\theta = 5-10$  and provided  $L_C \leq L_E$ .

Apart from the coefficient  $\Delta_\theta$  all other entries to the RHS of (4.8.1) were observable in the field campaign. Hence, we isolate from (4.8.1) the following expressions where, for convenience, we have put  $|dU/dz| \equiv (NRi^{-1/2})$  so that

$$Br = L_E L_C \frac{N^3}{Ri^{1/2}} \left( 1 + \frac{1}{2} \frac{1}{Ri} \right) \left( 1 - \frac{1}{2} \frac{L_C}{L_E} \right), \quad (4.8.2)$$

so that

$$T_{i-t}^{br} = \frac{Br}{\Delta_\theta}. \quad (4.8.3)$$

With reference to Tables 2 and 3 we commented on the large ratios  $L_E/L_C$  at the platform level. From Table 2 we derived the following mean values along the depth-time path of the suspended platform:

$$\text{day 156: } Br \approx 310 \text{ mm}^2/\text{s}^3 \quad (4.8.4)$$

$$\text{day 157: } Br \approx 5 \text{ mm}^2/\text{s}^3$$

The large difference in the magnitude of  $Br$  is also reflected in the estimates for  $\epsilon$  of about 10 and  $0.1 \text{ mm}^2/\text{s}^3$  derived from our microstructure observations on day 156 and 157 respectively along the path of the platform in Figures 21 and 23. The typical value of  $\Delta_\theta$  to match the observed values for  $\epsilon$  would be about 20 to 70. Hence, our first assessment  $\Delta_\theta = 5-10$  is too low and that would overestimate the transfer i.e.  $T_{i-t}^{br} > \epsilon$ .

From these coarse estimates we conclude that energy transfer to turbulence due to internal wave breaking appears to be an important contribution to turbulence production during our observations in the Rotterdam Waterway and in the Caland channel. Presently we do not have knowledge of the importance of quasi-2D turbulence.

For that reason we must first assess its energy content as the difference between total kinetic energy and kinetic internal wave energy. Thus the assessment of the importance of quasi-2D turbulence on  $\epsilon$  is a byproduct of Section 4.12 where we compare the estimates for the kinetic part of IWE with the total kinetic energy of finescale fluctuations. First, in the following Section 4.9 we investigate in a qualitative way the spatial and temporal wave patterns from echosounder observations along the water depth.

## 4.9 Echosoundings

Simultaneously with the other observations, echosoundings were made from the anchored vessel Pavo using its standard equipment at 33 kHz and at 210 kHz echosounders but without the electronic filters that cancel the weak echoes we are interested in. Actually, Pietrzak et al. (1988) compared the echosoundings with transects of conductivity measurements in the Rotterdam Waterway. They concluded that an echosounder can detect isopycnals. Although still subjected to discussion, the physical explanation for the echosounder sensitivity to density changes appears to be the following. Relatively strong acoustic reflectors such as fish, sea weed and particles act as Lagrangian density markers by having a preference to remain in water with constant salinity and constant temperature. Yet, in absence of these reflectors also acoustic backscattering from refractive index variations induced by density as well as by turbulence appears observable, see e.g. (Torpe and Bruhaker, 1983) and (Colbourne, 1987).

For day 156, Fig. 1 shows that the upper part of the stratified layer moved upward from about 8 m at 13:00 hours (34 min. past reference time) below the free surface to about 4 m at 18:00 hours (334 minutes past reference time). Similarly, the echosounder recorded the growing thickness of the denser, lower layer by patterns that produced more reflections below these levels. Moreover, within that denser region wavy patterns with an amplitude of about 1 m and horizontal wavelengths of about 10 m or more are vaguely visible on the echosounder recordings. However, the sharpest and strongest reflections originate from levels slightly above the region with maximal density gradient.

For instance, we attempt to show through Fig. 29 the typical patterns in echosounding on day 156 between 45 to about 62 minutes past reference time. Not only the free surface but also the bed is indicated in this figure. The slow variations in bed level actually are the motions of the anchored vessel Pavo with respect to the bed. In addition, the black bar between 1.5 to 2 m below the free surface is either the near field response of the acoustic emitter or the reflection from the fuselage of the Pavo. The level of the platform at 11 m depth during this period of observation is indicated in Fig. 29 as well as the upper part of the dense lower layer at 8 m. Actually, the acoustic reflection was strongest from the upper part of this dense layer. Moreover, the insert in Fig. 29 shows the accompanying finescale measurements 13:22/156. The insert shows the ebb current which, at about 14 m, created a critical level for bed generated waves, however, without detectable wave breaking. We tried to follow some visible wave patterns on the paper recordings by hand with a thick pen, Fig. 29 shows our trials. However, in attempting to do this it became clear that the patterns changed rather quickly or the patterns were only distinguishable during a few cycles and then faded away. Similar observations were made in the Caland channel on day 157. The acoustic reflections on paper were very faint and so are not reproduced here.

During the measurements on the afternoon of day 156 many ships of different sizes passed and their passage was noted in the logbooks. As much as we could, we selected our platform measurements during quiet intervals in the Rotterdam Waterway. During our observations on day 157 only a few and relatively small ships travelled in the Caland channel. By contrast, in the Rotterdam Waterway some large ships clearly produced internal waves of about 100 m wavelength.



For instance Fig. 30, recorded on day 156 at 349 minutes past reference time (18:05 hours), shows the best example of ship-induced internal waves obtained during our observations. This ship past the Pavo at a distance of about 200 m. During that period the upper part of the stratified lower layer was located at about 3 to 4 metres below the free surface. The ship-induced internal wave took about 90 seconds to reach the water column below the Pavo. This particular wave had an estimated amplitude of about 2 metres and a wavelength of about 200 metres. During the observation shown in Fig. 34 the velocity at 4 metres depth was about 0.9 to 1.0 m/s and directed upstream.

From our echosounder observations in the Rotterdam Waterway on day 156 and in the Caland channel on day 157 we conclude the following. Ship traffic in the Rotterdam Waterway may excite large amplitude internal waves of horizontal wavelengths of about 100 m or more. The flow-generated internal waves appear as random internal waves of amplitudes of about 1 m and wavelengths of about 10 m. These waves appeared in short groups or as contiguous series but with a coherence over only a few wavelengths. Moreover, no obvious coupling of the patterns i.e. a modal structure along the water column was visible. Hence, the recordings indicated a dense field of random waves in which individual groups of waves can not be isolated. With this conclusion in mind we derived in Chapter 3 an upper limit for a field of non-modal random internal waves. We may thus adopt the absolute quad spectra for the lower-limit estimator of IWE.

#### 4.10 Inspection of time series of finescale observations

To familiarize ourselves with the typical finescale recordings we will inspect a few sections of the  $(u, v, w, \rho)$  finescale signals observed from the platform. This platform was suspended from the crane of the anchored vessel Pavo. For instance, Fig. 31 shows the first 100 seconds of the measurement 12:53/156. The velocity and density signals shown in Fig. 31 were obtained after linear correction for platform motions. Moreover, the signals were filtered with a cosines-shaped 1 Hz low-pass filter in frequency space.

Finally, for a convenient presentation each signal has been normalized by twice its respective rms value which is based on the displayed time interval. The transverse velocity component  $v'$  usually is more "noisy" than  $u$  and  $w$ . This may be due to the incomplete correction of  $v$  against platform motions because only the transverse accelerations at the rear of the platform were observed. In addition, the streamwise velocity component  $u$  and the vertical component  $w$  still appear to contain small oscillations related to platform motions.

However, the energy content in such oscillations with a period of about 5 seconds was of the same order as the fluid motions induced by surface waves and thus the signals represent most likely real fluid motions.

A chance coincidence in observations appears to be the wave breaking phenomenon in Fig. 3a at 11 m depth and the large density peak in Fig. 31 at about 50 seconds after the start of platform measurement 12:53/156. The estimated time of arrival of the MicroProfiler (drop 12:51/156) at 11 m depth coincides with the occurrence of the large density peak in Fig. 31. In addition, details of the response of the velocity components are expanded in Fig. 32. The low-pass filtering slightly reduced the amplitude of the displayed oscillations at 50 s. The velocity magnitude was 600 mm/s and the streamwise wavelength was approximately 800 mm.



Another example of internal wave activity on the fine scale is given in Fig. 33 for platform measurement 12:53/156. At 360 s after the start of the platform measurement a depression of  $\rho$  is notable. In addition, with a phase shift, also the vertical velocity component  $w$  as well the transverse component  $v$  responded equally, however, not the streamwise component  $u$ . Fig. 34 is a later section of the same 30 minutes of measurement with short oscillations in vertical velocity  $w$  which were not observed in density. This is in contrast with Fig. 35 of test 13:32/156 where both  $w$  and  $\rho$  show responses to fluctuations of about 2 m streamwise wavelength. We conclude the following.

### *Conclusion*

The time signals of the platform instruments show no clear, long lasting patterns of internal waves passing through our instruments. This conclusion supports the echosounding observations presented in Section 4.9.

We conclude from the time series as well as from the echosoundings that the assumption of random internal waves appears to be valid and that the waves seem to travel in groups that contain only a few of the dominant wavelengths.

## **4.11 Analysis of short groups of internal waves**

The previous conclusion bares an important consequence for the spectral analysis dealt with in the next sections. For instance, suppose we are interested in the phase angle  $\phi_{\rho w}(\lambda)$  between density and vertical velocity fluctuations induced by waves at a particular streamwise wavelength  $\lambda$ . If we know these waves belong to one group with distinct direction of propagation as well as a distinct intrinsic frequency then analysis over a long time window is appropriate. However, if the waves at the wavelength of interest belong to different wave groups then analysis over a long time window will actually destroy or diminish the observed properties of one group with respect to properties of another group. In particular this is important if the different groups of internal waves possess phase angles of opposite signs. Such changes in the sign of  $\phi_{\rho w}$  depend on the direction and the magnitude of the streamwise component of the group velocity and the streamwise velocity that transports the wave pattern through a fixed point of observation, see e.g. (Uittenbogaard, 1993).

Hence, for a given streamwise wavelength  $\lambda$  we should "close" the initially too long time window to some shorter duration  $T$  such that only a limited number, say  $n$ , of wavelengths is included. On this short time series spectral analysis was performed and subsequent averaging over many contiguous sections increased the reliability of the results. This is a well-known dilemma in non-stationary time series analysis.

Together with the window a suitable taper, which suppresses the signals near the start and the end of a record, is needed to avoid contributions due to the Gibbs phenomenon (Bendat and Piersol, 1971). However, this tapering increases the variance of the spectral estimates. Conversely, 90% of this increase in variance can be reduced by taking 50% overlapping records.

In view of the preceding discussion we will present in the following Section 4.11 results obtained with only two streamwise wavelengths per record by means of convolution of the spectra with the so-called Hanning taper of width  $\Delta f$  proportional to the frequency  $f$  of interest:



$$W(f; \Delta f) = \frac{1}{2} \left[ 1 + \cos \left( \frac{\pi f}{\Delta f} \right) \right] ; \quad |f| \leq \Delta f , \quad (4.11.1)$$

$$W(f) = 0 ; \quad |f| > \Delta f .$$

Transformed into time, the Hanning taper (4.11.4) has a width  $8/\Delta f$  and oscillates with a diminishing amplitude outside this interval.

## 4.12 Spectra derived from time series observations

The power spectra, the phase angle  $\phi_{\rho w}$  as well as the coherence between density and vertical velocity of the finescale observations were already presented in (Uittenbogaard, 1993). However, that report contained rather noisy spectra and also strong variations in phase angles. Actually, only the first 3 lowest frequency points exhibited a  $90^\circ$  phase shift. If the time-window was reduced to a quarter of its previous size then again the first lowest frequency points beyond the previous 3 frequency points showed the  $90^\circ$  phase shift.

These trials demonstrate the need to apply (4.11.1) to avoid destruction of the phase relation between density and vertical velocity by averaging over wave groups which differ in propagation direction as well as in magnitude of phase velocity relative to the mean flow. Hence, all spectra presented in this section were treated by the window closing procedure described in Section 4.11 and by using (4.11.1).

Fig. 36 to 45 are the energy density spectra, phase angle and coherence processed according to the progressive convolution in frequency space. For instance, Fig. 36 contains the spectral energy density for total KE, the upper-limit estimate (3.2.3) as well as the lower-limit estimate (3.2.5) and (3.2.6) both substituted into (3.2.1). This figure represents the first measurement 12:53/156 (12 hours, 53 minutes on day 156 in the Rotterdam Waterway). Down to streamwise wavelengths of about 5 m the phase shift between density and vertical velocity is within the interval  $\pm(90^\circ \pm 10^\circ)$  and possesses a significant coherence. Moreover, this figure also displays a change in the sign of the phase angle of about  $180^\circ$  magnitude. The phase angle of  $+90^\circ$  belongs to waves that have a phase speed component opposite to the flow but with a relative phase velocity smaller than the advection speed. Hence, these waves are viewed "from the rear".

The  $-90^\circ$  phase angle either belongs to waves travelling against the current but with relative phase speed faster than the current velocity or waves that travel along with current. The finescale time series observation 16:15/156 (Fig. 41) also exhibits such a change in phase angle.

In this and subsequent figures, two lines with slopes proportional to  $\lambda^3$  and  $\lambda^{5/3}$  are added to the power spectra diagram for reference. The hump at a wavelength of about 3 m is the contribution due to velocity fluctuations induced by surface waves (Uittenbogaard, 1993). The hump is slightly widened by the progressive smoothing operation described in Section 4.11.

Table 1 presents the mean values for day 156 with the mean of the upper limit estimate for KIWE is about 102% and the mean of the lower estimate approx. 74% of the total KE. Our largest ratios of 216% (upper) and 104% (lower) for the are both found for the finescale observation 15:36/156 (Fig. 40) in the Rotterdam Waterway.

For clarity and easy reference we repeat some of the definitions used in Chapter 3 and in (Uittenbogaard, 1993) concerning spectral analysis. The Fourier transform (here a FFT) of variable  $x(t)$  is defined as  $F_x$  and its argument actually is frequency  $f$ . However, we will convert this frequency into the number of cycles per m (cpm) or inverse streamwise wavelength by:

$$\lambda^{-1} = \frac{f}{U}, \quad (4.12.1)$$

with  $U$  the observed streamwise velocity during the interval of the measurement. Further we define:

- $G_{xy}$  as the complex cross spectrum,
- $\Pi_{xy}$  as the normalized complex cross spectrum,
- $C_{xy}$  as the real coincidence-spectrum or co-spectrum,
- $Q_{xy}$  as the real quadrature-spectrum or quad-spectrum,
- $|Q|_{xy}$  as the real absolute quad-spectrum,
- $\phi_{xy}$  as the phase angle and
- $\gamma_{xy}$  as the real coherence.

Their interrelations read as follows:

$$G_{xy} = \langle F_x^c F_y \rangle = C_{xy} - i Q_{xy}; \quad \phi_{xy} = \arctan\left(\frac{Q_{xy}}{C_{xy}}\right), \quad (4.12.2)$$

$$|Q|_{xy} = \langle |\text{Im}(F_x^c F_y)| \rangle, \quad (4.12.3)$$

$$\Pi_{xy} = \frac{G_{xy}}{G_{xx}^{1/2} G_{yy}^{1/2}}; \quad \gamma_{xy}^2 = |\Pi_{xy}|^2. \quad (4.12.4)$$

Here the ensemble brackets, applied to Fourier transforms, imply averaging of spectra over all obtainable records, with 50% overlap, from one 30 minutes finescale measurement. The Fourier transforms are actually FFT and linearly corrected for platform motions, see (Uittenbogaard, 1993) for details.

Further, we have defined and derived in Chapter 3 the lower-bound IWE estimator for twice the kinetic energy of internal gravity waves in terms of 3D energy density spectra using the absolute quad-spectra (3.2.4). By means of (4.12.1) we will make the desired connection between the 3D wavenumber spectra and frequency spectra observed from in a fixed point in horizontal flow with velocity magnitude  $U$  m/s. For instance, the Eulerian frequency spectrum  $E(f)$  is connected to the 3D-vertical displacement spectrum  $\Pi_z(\mathbf{k})$  by

$$E_z(f) \equiv \int_0^\infty \int_0^\infty \Pi_z\left(\mathbf{k} \equiv \frac{2\pi f - N \cos \theta}{U}, \ell, m\right) + \Pi_z\left(\mathbf{k} \equiv -\frac{2\pi f - N \cos \theta}{U}, \ell, m\right) d\ell dm. \quad (4.12.5)$$

Conversely, (4.12.5) demonstrates the ambiguity to estimate  $\lambda$  given frequency  $f$  due to the Doppler shift by the intrinsic frequency of internal waves. Below we will analyze this problem. We translate the ambiguity in streamwise wavenumber  $k$  into half the bandwidth of streamwise wavelength by means of the following steps:



$$\Delta k = \frac{2N \cos \theta}{U} ; \Delta k \equiv \frac{2\pi}{\lambda - \Delta \lambda} - \frac{2\pi}{\lambda + \Delta \lambda} ; \frac{\frac{\Delta \lambda}{\lambda}}{1 - \left(\frac{\Delta \lambda}{\lambda}\right)^2} = \frac{N \lambda \cos \theta}{U} ; \tan \theta = \left| \frac{\lambda \cos \phi}{\lambda_z} \right| \quad (4.12.6)$$

In (4.12.6) we assume a horizontally isotropic energy distribution so that we set  $\phi = 45^\circ$ . Further, the magnitude of  $\cos \theta$  is maximal when the magnitude of  $\tan \theta$  is minimal. However, the largest vertical wavelength  $\lambda_z$  is limited by the stratified layer thickness  $H$  and we take  $\lambda_z \leq H$ . Consequently, for typical values summarized in Table 1 follows from (4.12.6):

$$\frac{\Delta \lambda}{\lambda} \leq 0.5 . \quad (4.12.7)$$

The upper limit of (4.12.7) holds for  $\lambda$  at least one order of magnitude larger than  $H$ . The ambiguity slightly reduces to about 0.30 for  $\lambda = H$ . The estimate (4.12.7) shows that besides the problem of summation over different wave groups, dealt with in Section 4.11, we also average over a wavenumber interval. Uittenbogaard (1993) constructed a series of 3D linear internal waves and analyzed them as if this pattern was advected through an imaginary observation point and recorded as time series. Then he found that the coherence, as a measure of linear response (Bendat and Piersol, 1971), between density and vertical velocity, which should be unity for the idealised linear wave field, reduced because of averaging over a bandwidth of  $k$  and averaging over intrinsic frequencies as well.

Hence, in view of (4.12.7) the reader is warned to take the wavelength  $\lambda$  in the plots too exact. In addition, the reader should be aware of the consequences of summing over a bandwidth and over a range of intrinsic frequencies on coherence, phase angles etc..

For notational convenience, we indicate the frequency dependence of Eulerian absolute quad-spectra as

$$|Q|_{\rho u_i}^{(f)} \equiv \int_0^\infty \int_0^\infty |Q|_{\rho u_i} \left( k \equiv \frac{2\pi f - N \cos \theta}{U}, \ell, m \right) + |Q|_{\rho u_i} \left( k = -\frac{2\pi f - N \cos \theta}{U}, \ell, m \right) d\ell dm .$$

By means of the previous definitions while using (3.2.5) and (3.2.6) the lower-bound estimator for twice the kinetic IWE derived from Eulerian frequency spectra now reads:

$$\langle \tilde{u} \cdot \tilde{u} \rangle = \left( N^2 + \left( \frac{dU}{dz} \right)^2 \right) \int_0^\infty \chi E_t(f) df \quad [m^2 s^{-2}], \quad (4.12.8)$$

with

$$\chi = \left( N \left| \left\langle \frac{\partial \rho}{\partial z} \right\rangle \right| \right)^{-1} \quad [m^4 s kg^{-1}] \quad (4.12.9)$$

and

$$\chi \tilde{E}_t(f) \equiv \chi \left[ \left( |Q|_{\rho u}^{(f)} \right)^2 + \left( |Q|_{\rho v}^{(f)} \right)^2 + \left( |Q|_{\rho w}^{(f)} \right)^2 \right]^{1/2} \quad [m^2 s^{-1}] . \quad (4.12.10)$$

Equivalent to (3.2.3) the upper-bound IWE-estimator expressed in Eulerian frequency spectra yields

$$\langle \tilde{u} \cdot \tilde{u} \rangle = \left( N^2 + \left( \frac{dU}{dz} \right)^2 \right) \int_0^\infty E_z(f) df \quad [m^2 s^{-2}], \quad (4.12.11)$$

with the energy density for the upper limit of vertical displacement  $Z$  similar to the definition of the Ellison scale:

$$E_Z(f) \equiv \frac{E_p(f)}{\left\langle \frac{\partial \rho}{\partial z} \right\rangle^2} \quad [\text{m}^2 \text{s}^{-1}] . \quad (4.12.12)$$

Strictly speaking, we should replace the infinity in the upper limit of frequency into the one corresponding to the minimal streamwise wavelength of internal waves of the order  $(\pi L_c)$ , however, the difference appears to be negligible.

For the purpose of studying internal waves we have computed cross spectra between density  $\rho$  and the velocity components  $(u, v, w)$ . We will compare these observations with properties of equivalent spectra following from the Taylor-Goldstein equation for infinitesimal waves. For that purpose we will use the analytical expressions derived in Chapter 2 for solutions to the Taylor-Goldstein equation. In Chapter 2 we used the notation  $\langle \tilde{\rho} \tilde{u}^\infty \rangle$  for the complex-valued cross correlation at each wavenumber vector  $\underline{k}$ . Instead, we will write such a product as the cross spectrum  $\tilde{G}_{\rho u}$  where the tilde ( $\sim$ ) refers to the analytical wave-like solutions. The wavenumber vector is expressed into the following spherical coordinates

$$k = |\underline{k}| \cos \phi \sin \theta ; \ell = |\underline{k}| \sin \phi \sin \theta ; m = |\underline{k}| \cos \theta \quad (4.12.13)$$

and we can relate the observed temporal variation into spectra depending on  $k$  but averaged over all  $(\ell, m)$ . For convenience we will express the analytical spectra into the power spectrum  $\tilde{E}_Z$  of the wave-induced vertical displacement  $Z$ . Further, in the spirit of the Taylor-Goldstein equation applied to a flow with mean shear rate  $(dU/dz)$  and mean vertical gradient  $(d\rho_0/dz)$  with time-independent background density  $\rho_0(z)$  holds with complex-valued phase velocity  $c$ :

$$\frac{1}{2} \frac{D \tilde{\Pi}_Z}{Dt} = (kc_r) \tilde{\Pi}_Z \equiv \beta \tilde{\Pi}_Z . \quad (4.12.14)$$

The intrinsic, positive radian frequency reads  $\Omega = k(c_r - U)$ . In particular, the following analytical 3D-spectra are useful for comparison with those derived from observations.

We begin with the wave-induced shear stress spectrum:

$$\tilde{C}_{uw} = -\frac{1}{2} \frac{D \tilde{\Pi}_Z}{Dt} \frac{dU}{dz} - \frac{km}{k^2 + \ell^2} (\Omega^2 + \beta^2) \tilde{\Pi}_Z . \quad (4.12.15)$$

The analytical (complex) cross spectrum between the vertical velocity component and the density, which are solutions to the Taylor-Goldstein equation, reads:

$$\tilde{G}_{\rho w} = -\frac{1}{2} \frac{D \tilde{\Pi}_Z}{Dt} \frac{d\rho_0}{dz} + i\Omega \tilde{\Pi}_Z \frac{d\rho_0}{dz} . \quad (4.12.16)$$

The real part  $\tilde{C}_{\rho w}$  of  $\tilde{G}_{\rho w}$  is the buoyancy-flux spectrum and the imaginary part  $\tilde{Q}_{\rho w}$  is the quadrature spectrum for the vertical velocity component. Equation (4.12.16) shows that for growing waves the buoyancy flux is positive. The streamwise, wave-induced mass flux spectrum reads:

$$\tilde{C}_{\rho u} = \tilde{\Pi}_Z \frac{dU}{dz} \frac{d\rho_0}{dz} + \frac{1}{2} \frac{k\Omega}{k^2 + \ell^2} \frac{D \tilde{\Pi}_Z}{Dt} \frac{d\rho_0}{dz} - \frac{1}{2} \frac{km}{k^2 + \ell^2} \frac{D \tilde{\Pi}_Z}{Dt} \frac{d\rho_0}{dz} . \quad (4.12.17)$$



The second term in (4.12.17) represents the streamwise component of the Stokes drift if the wave energy is unevenly distributed along the vertical. This is a well known phenomenon for surface waves on a uniform flow. These surface waves induce vertical displacements increasing from zero at the bed to the wave amplitude near the surface. Then the second term in (4.12.17) gives a Stokes drift of density in the direction of surface wave propagation and projected on the x-direction.

However, if the wave field is practically stationary and, in addition, if the wave field depends only weakly on  $z$  then the first term in the RHS of (4.12.17) dominates. Actually, this term is the spectral contribution, at wavenumber  $\underline{k}$ , to the streamwise Stokes drift

$$\tilde{C}_{\partial \rho \partial u} = \tilde{\Pi}_z \frac{dU}{dz} \frac{d\rho_o}{dz} \quad (4.12.18)$$

for mass due to internal wave motions in a shear flow. We continue with the wave-induced quad-spectrum between density and streamwise velocity. It reads:

$$\tilde{Q}_{\rho u} = \frac{1}{2} \frac{k}{k^2 + \ell^2} \frac{\overline{D}}{Dt} \left( \frac{d\tilde{\Pi}_z}{dz} \right) \frac{d\rho_o}{dz} - \frac{km\Omega}{k^2 + \ell^2} \tilde{\Pi}_z \frac{d\rho_o}{dz} \quad (4.12.19)$$

Similarly for the real and imaginary part of the cross spectrum related to the transverse velocity component:

$$\tilde{C}_{\rho v} = \frac{1}{2} \frac{\ell\Omega}{k^2 + \ell^2} \frac{d\tilde{\Pi}_z}{dz} \frac{d\rho_o}{dz} + \frac{1}{2} \frac{\ell m}{k^2 + \ell^2} \frac{\overline{D}\tilde{\Pi}_z}{Dt} \frac{d\rho_o}{dz} \quad (4.12.20)$$

$$\tilde{Q}_{\rho v} = \frac{1}{2} \frac{\ell}{k^2 + \ell^2} \left( \frac{\overline{D}}{Dt} \frac{d\tilde{\Pi}_z}{dz} \right) \frac{d\rho_o}{dz} - \frac{\ell m\Omega}{k^2 + \ell^2} \tilde{\Pi}_z \frac{d\rho_o}{dz} \quad (4.12.21)$$

The first term of (4.12.20) is the y-component of the Stokes drift vector for unevenly distribution of wave energy along the vertical. We already pointed to the similar term in x-direction in (4.12.17).

The last term in (4.12.21) is the transverse contribution to the quad-spectrum of stationary or vertically uniform internal waves. We observe that the transverse mass flux component (4.12.20) possesses no mean-shear-induced Stokes drift and only depends on the vertical derivative and on the material derivative of the wave-induced displacement spectrum  $\tilde{\Pi}_z(\underline{k})$ .

For a steady and/or a vertically-uniform wave field the last term in (4.12.19) represents the streamwise contribution to the quad-spectrum of internal waves. This contribution to the streamwise quad-spectrum, together with the one for transverse and vertical velocity are summarized below, with  $\chi$  defined in (4.12.9):

$$\chi \tilde{Q}_{\rho u} = -[\cos\phi(\underline{k}) \sin\theta(\underline{k})] \tilde{\Pi}_z(\underline{k}) \quad (4.12.22a)$$

$$\chi \tilde{Q}_{\rho v} = -[\sin\phi(\underline{k}) \sin\theta(\underline{k})] \tilde{\Pi}_z(\underline{k}) \quad (4.12.22b)$$

$$\chi \tilde{Q}_{\rho w} = \cos\theta(\underline{k}) \tilde{\Pi}_z(\underline{k}) \quad (4.12.22c)$$

In the spirit of (4.12.22) we define the frequency-dependent angles determined from one time record as follows:

$$\phi(f) = \text{def} = \frac{180^\circ}{\pi} \arcsin \left( \frac{I_{\rho v}^{(f)}}{\sqrt{(I_{\rho u}^{(f)})^2 + (I_{\rho v}^{(f)})^2}} \right); \quad -90^\circ \leq \phi(f) < 90^\circ. \quad (4.12.23a)$$

$$\theta(f) = \text{def} = \frac{180^\circ}{\pi} \arctan \left( \frac{\sqrt{(I_{\rho u}^{(f)})^2 + (I_{\rho v}^{(f)})^2}}{I_{\rho w}^{(f)}} \right); \quad -90^\circ \leq \theta(f) < 90^\circ. \quad (4.12.23b)$$

These angles, determined from one time record only, are based on the following quadrature spectra derived per record:

$$I_{\rho u_i}^{(f)} = \text{def} = \text{Im} \left( F_{\rho}^{\infty}(f) F_{u_i}(f) \right) \quad (4.12.24)$$

Because of the averaging over the planes  $k = \pm 2\pi f/U$ , the ambiguity (4.12.7) as well as the nonlinear operations involved we cannot regard (4.12.23) as the angles appearing in (4.12.2-2). In view of (4.12.5) we cannot discriminate between wavenumbers opposite to each other and therefore we limited the magnitude of  $\phi(f)$  to  $90^\circ$ .

With the angles defined by (4.12.23) and averaged over the available 50% overlapping records of the 30-minutes measurements we intend to summarize the typical ratios between the quadrature spectral components. Actually, the mean values of the angles (4.12.23) represent a number counted average over wave groups rather than an average weighted by energy content.

With our choice of the intervals for the angles we can compute their mean values  $\langle \phi(f) \rangle$  and  $\langle \theta(f) \rangle$  as well as the mean of their absolute values  $\langle |\phi(f)| \rangle$  and  $\langle |\theta(f)| \rangle$ . These estimates may provide useful information about the variability of the angles. For instance, if  $\langle \theta(f) \rangle$  practically coincides with  $\langle |\theta(f)| \rangle$  or with  $-\langle |\theta(f)| \rangle$  then we infer that at this frequency/wavelength the angle  $\theta(f)$  kept the same sign among subsequent records. Another example may be that  $\langle \phi(f) \rangle \approx 0^\circ$  but  $\langle |\phi(f)| \rangle \approx 45^\circ$ , then we infer horizontal isotropy at that frequency/wavelength.

Armed with the previous definitions we have made the plots in Figures 36 to 45 for the finescale observations on day 156 and 157. The upper part of Fig. 36a displays the observed total kinetic energy as well as the lower and upper limit spectral estimates for KIWE. The legend of the upper part of Fig. 36a indicates "Total KE" which is the sum  $\frac{1}{2}(G_{uu}^{(f)} + G_{vv}^{(f)} + G_{ww}^{(f)})$  and  $G_{xy}$  defined in (4.12.2). Further, this legend notes "IWE- $\rho^2$ " and this is the upper bound estimate according to (4.12.11) in conjunction with (4.12.12) and corresponds to assuming the Ellison length scale is entirely wave-induced. Finally, the legend ends with "IWE- $\rho^2 u$ " and this the lower bound estimate (4.12.8) using (4.12.9) and (4.12.10) and it is based on quad-spectra only (in square power).

The middle part of Fig. 36a presents the phase  $\phi_{\rho w}$  between density  $\rho$  and vertical velocity  $w$  and the lower part of Fig. 36a displays the coherence between  $\rho$  and  $w$ , see (4.12.4). The straight dotted lines in the upper part of Fig. 36a belong to slopes of  $k^3$  and of  $k^{-3/2}$ . The dotted lines in the middle part of Fig. 36a are  $10^\circ$  intervals around  $\pm 90^\circ$  phase shift.

Fig. 36b is our attempt to indicate, per Cartesian component, the contribution of the estimates for internal wave velocity variances. With the discrete frequency  $f$  as intermediate parameter we have plotted along the vertical axes the value of the energy density spectra  $G_{uu}$ ,  $G_{vv}$  and  $G_{ww}$  for  $u, v$ , and  $w$  respectively. Along the horizontal axes we have plotted the internal wave estimate based on absolute quad-spectra.



However, for the streamwise internal wave velocity component ( $u$ ) we added  $G_{\partial u \partial u}^{(f)}$  defined by

$$G_{\partial u \partial u}^{(f)} = \text{def} = \chi E_t(f) \left( \frac{dU}{dz} \right)^2. \quad (4.12.25)$$

This is the contribution (2.4.33) to the streamwise velocity variance by wave-induced vertical displacement in a shear flow. Actually, in (4.12.25) we implemented the lower bound estimator for the energy density of the wave-induced vertical displacement. In Fig. 36b the full straight lines gives a 1:1 ratio whereas the dotted line indicate 2:1 i.e. 200% overestimation of the observed energy density. If the points, indicated by "+", lie above the full straight line than there is underestimation. For instance, from Fig. 36d we conclude that for the highest spectral energy levels the IWE estimates tend to a 100% prediction of the observed (total) energy density.

However, we must keep in mind the problem discussed at the end of Section 3.2. There we discussed the problem of relating the individual variances of the three vector components to estimators based on a single scalar quantity (displacement). Of course, summation yields the comparison between the full line in the upper part of Fig. 36a indicated in its legend by  $\{\text{IWE}-\rho'u'\}$ .

The upper part of Fig. 36c presents the normalized shear spectrum and the vertical mass flux spectrum, both defined by (4.12.4); the dotted line indicates zero. The middle part of Fig. 36b presents all phase angles between density and the three Cartesian velocity components ( $u, v, w$ ) and this part includes the  $10^\circ$  tolerances around  $90^\circ$  phase angles. Similarly, the lower part of Fig. 36c presents all coherences between  $\rho$  and ( $u, v, w$ ).

Finally, Fig. 36d shows the mean values and mean absolute values of angles  $\phi$  and  $\theta$  defined by (4.12.23) and inspired by (4.12.22) in wavenumber space. The straight dotted line in the top part of Fig. 36d represents  $\theta = 55^\circ$  corresponding to  $\tan \theta = \sqrt{2}$  for isotropic waves. For  $\theta$  exceeding  $55^\circ$  the energy density tends to be concentrated around vertically oriented wavenumber vectors  $\underline{k}$  and consequently the wave-induced velocity vector tends to horizontal motions. Similarly, the middle part of Fig. 36d presents  $\phi$  and the dotted line at  $45^\circ$  represents horizontally isotropic energy distribution. Finally, the lower part of Fig. 36d is our attempt to check how much of the spectral streamwise mass flux  $C_{\rho u}$  can be explained as second-order Stokes drift (4.12.18) for stationary waves, uniformly distributed in space. If the ratio

$$\text{St} = \frac{\tilde{C}_{\rho u}^{(f)}}{\tilde{C}_{\partial \rho \partial u}^{(f)}} \quad (4.12.26)$$

deviates from unity then a part of the streamwise mass flux must be the result of other hydrodynamical drift phenomena included by the second or third term in (4.12.17) or excluded by our analysis such as nonlinear waves, 2D turbulence etc.. From 3rd order Ausgleich spline fits to the vertical finescale observations underlying Fig. 1, we determined the mean shear rate ( $du/dz$ ) and the mean density gradient ( $d\rho_0/dz$ ). The latter is always negative (stable stratification), the former always positive except for the finescale observation 16:15/1-56 at the interval 228-258 minutes past reference time.

Now we will comment on the spectra derived from the finescale time series observations and we start with day 156 (Rotterdam Waterway).



*Finescale observations in the Rotterdam Waterway (Fig. 36 to 41)*

Fig. 36a shows that the estimates for KIWE follow closely the one for the total kinetic energy at large wavelengths. Below a streamwise wavelength of 5 m the IWE estimates are smaller by a factor of 10 than the total kinetic energy. In the wavelength range exceeding 5 m, both the coherence as well as the phase angle indicate the significance of linear internal waves. With respect to the coherence we again caution the ambiguity due to averaging over a bandwidth of wavenumbers as well as over a range of intrinsic frequencies. This ambiguity reduces the coherence even if the waves can be regarded as linear.

In conjunction with Fig. 36a, Fig. 36b confirms these descriptions for each velocity component separately: the highest energy density levels are fairly well approximated by the IWE estimates.

Fig. 36c shows that the coherences between density  $\rho$  and all velocity components ( $u, v, w$ ) behave similarly and virtually disappear for wavelengths smaller than approximately 10 m. Further, the top part of Fig. 36b shows that the normalized shear spectrum and normalized buoyancy flux spectrum have opposite signs and change their sign at approximately the same wavelength. In view of the first term in the analytical wave-induced shear stress spectrum (4.12.15) as well as the real part of the buoyancy-flux spectrum (4.12.16) this is an interesting signature of the dominance of the shear rate on the shear spectrum (4.12.15). Suppose internal waves at a particular wavelength grow, then the buoyancy flux in (4.12.16) is positive (note  $d\rho_0/dz$  is negative). In conjunction with growing waves, at the same wavelength the correlation  $\langle u'w' \rangle$  is negative implying a consumption of mean flow energy by the waves. Fig. 36c shows that the phase shift between density and horizontal velocity components is either  $0^\circ$  or  $180^\circ$  for wavelengths exceeding 5 m. A magnitude of  $180^\circ$  for the phase angle  $\phi_{\rho u}(f)$  supports the importance of the mean-shear-induced Stokes drift (4.12.18) which is directed opposite to the flow because the product  $(dU/dz) \cdot (d\rho_0/dz)$  is negative. The only observation where this product is positive, because  $(dU/dz) < 0$ , is measurement 16:15/156 and indeed Fig. 41c shows that  $\phi_{\rho u}(f)$  tends to  $0^\circ$  rather than  $180^\circ$  over the bandwidth where the coherence between density and streamwise velocity is maximal.

Fig. 36d shows that the wavenumber vector for the longest waves tend to the vertical and below a streamwise wavelength of about 30 m the mean of  $\theta$  tends to zero whereas the mean of the absolute values of  $\theta$  tend to isotropy in the vertical plane. This is accompanied by the horizontal isotropy depicted in the middle part of Fig. 36d.

In contrast with the nonlinear analysis in Section 2.7 we do not observe in Fig. 36d that  $\theta$  tends to  $0^\circ$  for very large horizontal wavelengths. Instead the general trend for all the finescale measurements is that  $\langle \theta(\lambda) \rangle$  is negative, usually smaller than  $-45^\circ$ , for streamwise wavelengths exceeding about 30 m and  $\langle \theta(\lambda) \rangle$  tends to zero for decreasing wavelengths.

The ratio  $St$ , defined in (4.12.26), drops to zero near  $\lambda=5$  m. However, more than 60% of the horizontal mass flux, oriented opposite to the mean flow, can be explained by (4.12.1-8) for  $\lambda \geq 30$  m.

In addition, the top part of Fig. 36d shows that only for the longest wavelengths the magnitude of  $\langle \theta(\lambda) \rangle$  approximately equals  $\langle |\theta(\lambda)| \rangle$ . For streamwise wavelengths  $\lambda < 30$  m we infer that the "number" of observed wave groups propagating upwards are nearly equal to the number of groups propagating downwards.



We deliberately mention the "number" of wave groups rather than wave energy because the averaging over angle  $\theta(f)$ , defined in (4.11.23b), is irrespective of the energy involved.

With less detailed explanations we continue with the essential points in the subsequent figures. Fig. 37a shows no sign reversal for the phase  $\phi_{pw}$  between density and vertical velocity component. The opposite signs and sign reversals of the normalized shear spectrum and the normalized buoyancy spectrum is again exhibited in the top part of Fig. 37b. The mean-shear-induced Stokes drift of density accounts for 50% or more the observed streamwise mass flux  $C_{pu}$  in the lower part of Fig. 37d. Moreover, the phase angle  $\phi_{pu}$  between density and streamwise velocity component coincides with the observed mass flux opposite to the flow.

The structure of the vertical finescale near the depth of 12 m of the platform during the finescale time series observation 16:15/156 is quite complicated. At a depth of about 10.5 m the flow changes direction and  $(dU/dz)$  is negative at the platform position and the flow curvature  $d^2U/dz^2$  is strong.

During the finescale observation the mean flow at the platform level yields 690 mm/s and is directed landinwards. The estimates for IWE are remarkable low at this point.

The estimates for IWE in Fig. 41a predict a small ratio of about 11% to 16% between KIWE and total kinetic energy. Nevertheless, the coherence as well as the phase angle between density and the vertical velocity component are of the same quality as for the higher energy ratios recorded in the previous observations. Despite the small IWE content, the vertical absolute quad-spectrum approaches the observed vertical energy density well for at least a decade in energy levels (right part of Fig. 41b).

Earlier we already alluded the notable change in this observation of the phase  $\phi_{pu}(\lambda)$  between density and the streamwise velocity component from the usual  $180^\circ$  to about  $0^\circ$ . This phase of nearly  $0^\circ$  reflects the negative mean-shear rate  $(dU/dz)$ . According to the lowest part of Fig. 41d most of the streamwise density flux can be explained by the shear-induced drift (4.12.18).

#### *Intermediate summary of finescale observations in the Rotterdam Waterway*

In general we infer the following from the comparison between relations satisfied by solutions to the Taylor-Goldstein equation and the field observations on day 156 in the Rotterdam Waterway.

- Based on a fairly large coherence and  $\pm 90^\circ$  phase between vertical velocity component and density and on the opposite sign changes of the vertical momentum flux spectrum versus the buoyancy spectrum it appears that a significant part of the motions with streamwise wavelengths exceeding 5 m can be designated as internal waves of random nature and fairly well describable with linear theory and as short wave groups.
- Between 5 and 30 m these waves tend towards isotropy in the horizontal as well as in the streamwise vertical plane.
- If we use  $\frac{1}{2}(L_E/H)$  as the upper limit between wave amplitude and vertical wavelength then data from Table 1 shows that this ratio is about 0.05. This result indicates that gravitational unstable density profile only occurs rarely. Although not entirely independent, this is supported by a mean value for the rms vertical slope of the density isolines:  $\alpha=0.43$  (Table 1).



- At streamwise wavelengths exceeding 30 m all observations indicate internal waves with a negative angle  $\langle \theta(f) \rangle < -45^\circ$  between their wavenumber vector and the horizontal plane and  $\langle \theta(f) \rangle$  defined according to (4.12.23b). In addition, in the same wavelength range the mean absolute value  $\langle |\theta(f)| \rangle$  yields values between  $60^\circ$  and  $80^\circ$ . A tentative conclusion is that for streamwise wavelengths larger than about 30 m the wavenumber triangle of Fig. 2.7.3 in Section 2.7 prevails with  $\theta_a$  and  $\theta_b$  ranging from  $100^\circ$  to about  $120^\circ$  in that figure.
- In the range  $\pi L_c < \lambda < 5$  m the spectral IWE estimates, based on linear theory, are one order of magnitude smaller than the observed spectral kinetic energy density. In this range we expect much stronger nonlinear wave-wave interactions and wave breaking as preluded in Section 2.7.
- The mean ratio between upper IWE estimate and total kinetic energy is 102 % and between lower IWE estimate and total kinetic energy 74 % .
- Of all the absolute quad-spectra estimates, the one for the streamwise velocity component, although augmented with the mean-shear-induced variance (4.12.25), strongly underestimates the observed variance  $\langle u'^2 \rangle$  (mean ratio 0.6). This is in contrast with the apparent overestimation (mean ratio 1.1 for  $\langle v'^2 \rangle$  and 1.3 for  $\langle w'^2 \rangle$ ) by the absolute quad-spectra of the remaining velocity components. This latter overestimation is not unexpected in view of the discussion, at the end of Section 3.2, about the problem of defining energy of a vector field if it is supposedly related to a scalar displacement field. Hence, we conclude that the unexpected and yet unresolved point is the severe underestimation of the streamwise velocity variance.

#### *Finescale observations in the Caland Channel (Fig. 42 to 45)*

The results of the spectral analysis of the data on day 157 in the Caland channel are shown in Fig. 42 to 45 and they differ in certain aspects significantly from those derived from the Rotterdam Waterway finescale observations.

According to Table 1 on day 157 the gradient Richardson number was large while the flow velocity was about 200 mm/s instead of 500 mm/s in the Rotterdam Waterway.

The influence of the mean shear rate ( $dU/dz$ ) on the horizontal shear-induced density flux is less marked as is demonstrated by the lower part of Fig. 42d to 45d as well as the phase  $\phi_{\rho u}$  in the middle part of these plots.

In addition, the opposite signs as well as the sign reversals of the normalized vertical momentum and buoyancy flux spectra in the top part of Fig. 42b to 45b is less distinctive, if notable at all.

Yet the phase angle  $\phi_{\rho w}(\lambda)$  between density and the vertical velocity component still exhibited a magnitude of about  $90^\circ$  for  $\lambda > 5$  m. Note that the largest streamwise wavelength  $\lambda$  in Fig. 45 is one order of magnitude smaller than in the previous observations on day 157. The reason is that during this observation the mean velocity had decreased to only 60 mm/s, see Fig. 2. Actually, the next finescale observation (not shown in this report) was discarded because the platform was not aligned with the mean flow direction any more.

In comparison with the spectral IWE estimates on day 156 those on day 157 more closely follow the  $\lambda^3$  power law. Despite the larger gradient Richardson numbers on day 157 the ratios between the lower and upper KIWE estimates and total kinetic energy are smaller: 42% and 60% respectively. Similar to day 156 this underestimation is mainly caused by the underestimation of the variance of the streamwise velocity (mean ratio 0.4) compared with the ratios 1.0 for  $\langle v'^2 \rangle$  and 0.9 for  $\langle w'^2 \rangle$ .



*Intermediate summary of finescale observations in the Caland channel*

- In comparison with the finescale observations in the Caland channel the relatively large mean-shear rate in the Rotterdam Waterway provided us with more (linear) signatures of internal waves.
- Beyond streamwise wavelengths of about 10 m the coherence and phase between density and the vertical velocity component indicate internal waves.
- Below a streamwise wavelength of about 10 m the angles defined in (4.12.23) indicate isotropy in horizontal as well in the streamwise oriented vertical plane.
- At large streamwise wavelengths of about 10 to 50 m the absolute mean  $\langle |\theta(f)| \rangle$  resembles triads such as shown in Fig. 2.7.3 which corresponds to a small streamwise wavenumber in comparison with their vertical wavenumbers.
- During the 4 successful finescale observations at gradient Richardson numbers  $Ri$  of 2 to 10 in the Caland channel we obtained a ratio between lower KIWE estimate and total kinetic energy of 42% whereas the ratio with respect to the upper KIWE estimate yields 60%.
- The mean amplitude vertical wavelength ratio  $\frac{1}{2}(L_E/H)$  is only about 0.03 while the rms of the wave-induced slope of density isolines  $\alpha$  remained 0.47. This indicates marginal wave breaking.
- Of the absolute quad-spectra estimates the one for the streamwise velocity component, although augmented with the mean-shear-induced variance (4.12.25), strongly underestimates the observed variance  $\langle u'^2 \rangle$  (mean ratio 0.4). This is in contrast with the apparent overestimation (mean ratio 1.0 for  $\langle v'^2 \rangle$  and 0.9 for  $\langle w'^2 \rangle$ ) by the absolute quad spectra of the remaining velocity components. In view of the discussion, at the end of Section 3.2, about the problem of defining energy of a vector field we conclude that the unexpected and yet unresolved point is the severe underestimation of the streamwise velocity variance.

*Discussion: what accounts for the difference between lower-limit IWE estimates and total kinetic energy?*

At this point the reader may appreciate first a brief review of the possible errors in the lower-limit IWE estimators before we continue to consider purely hydrodynamic phenomena that may fill the gap between the lower-limit IWE estimates and the total kinetic energy.

We favour the lower-limit IWE estimator based on absolute quad-spectra more than the power spectral estimator based on density fluctuations for the following reasons. On the one hand the lower-limit estimator may be biased by turbulence contributions if and only if turbulence contributes to streamwise wavelengths exceeding 5 m. From the numerous microstructure signatures we believe this cannot be the case at the level of the platform; we will come back to possible contributions from 2D turbulence.

On the other hand there still may be doubt about the (i) quality of the correction of the velocity density signals against platform motions and (ii) artificial correlations originating from electronic noise. However, the advantage of our usage of quad-spectra over power spectra is that our quad-spectra are composed of the density signal and the signal of each one of the velocity components separately. Such combinations reduce significantly or even cancel spurious correlations. For instance, electronic noise in the same two-component electromagnetic current meter (EMS) may create spurious correlations by cross talk, although careful towing tank tests did not reveal this but in the field this may have occurred.



In addition, the signal paths for the conductivity and for the velocity recordings followed separate amplification and entirely different electronic processing stages until the point where they were A/D converted.

Thus we are left with the option of spurious correlations by means of cross talk between density and velocity components through rigid platform motions. We found in a narrow frequency band around 0.2 Hz (apparent streamwise wavelength about 1 m in Fig. 36-45) an excellent coherence of 0.99 between the relevant estimator for the platform displacement induced in the instrument's position and the density or the velocity recordings. In Uittenbogaard (1993) we presented these coherence and transfer functions. However, this high coherence shows that corrections using linear transfer functions, on line calibrated, is the preferred procedure. Still we cannot exclude that the corrected signals contain, in some unknown non-linear fashion, a signature of the platform motions. This may be an argument to suspect cross correlations. However, the influence of nonlinear platform motions on density and separately on the velocity recordings are very unlikely combined to produce a contribution to quad-spectrum i.e. a cross correlation per frequency. So except for 2D turbulence the quad-spectra appear to be robust IWE estimators.

Then we must explain what hydrodynamic phenomenon can account for the remaining 26% difference between total kinetic energy and lower-limit IWE estimate on day 156 and the 58% on day 157?

With reference to the Craya decomposition (2.5.12) in Section 2.5 as well as the numerical simulations referred to, a proposal may be quasi-2D turbulence. Numerical simulations of grid-generated stratified turbulence showed that stacks of horizontal layers with different vertically oriented vorticity are created after the extinction of 3D turbulence. If these stacks of quasi-2D turbulence are indeed formed then we expect a horizontal isotropic contribution to the  $\langle u'^2 \rangle$  and  $\langle v'^2 \rangle$ . Instead, we observed that the variance of  $v'$  and  $w'$  are well estimated by quad-spectra and the main deficiency lies in the underestimation of the variance of the streamwise velocity component. Hence, this makes the contribution by quasi-2D turbulence in our finescale measurements most unlikely.

The only hydrodynamic phenomenon we can presently imagine and that may explain for underestimation of solely  $\langle u'^2 \rangle$  is the formation of a staircase profile for the streamwise velocity. For instance, consider the staircase of density jumps in Fig. 5 and 6. The strong suppression of vertical momentum transfer at the multiple levels of large density gradients may also produce similar patterns of decoupled velocity layers in a flow with a significant  $dU/dz$ . In absence of a transverse mean shear rate  $dV/dz$  no such velocity jumps are expected in transverse direction. At the high velocities the platform will align itself to the flow in such a way that with respect to its coordinate system  $dV/dz$  is either zero or very small. A non-zero  $dV/dz$  can be provided if the horizontal velocity vector veers but this is hardly observed in our vertical finescale observations.

Thus we conclude that the platform aligned itself in a vertical plane with  $dU/dz$  maximal and in this plane along the vertical the streamwise velocity may exhibit jumps corresponding to the observed density jumps. Then two effects may create a contribution to  $\langle u'^2 \rangle$ . The first argument may be that the layers with the assumed velocity jumps have a finite extend similar to a pancake. The velocity transition levels may change randomly between subsequent "pancakes" and thus contribute to  $\langle u'^2 \rangle$ . In addition, during the passage of one pancake the vertical motions of the platform itself may sample above and below the transition levels and this may be misinterpreted as streamwise velocity fluctuations.

However, we have no direct observational evidence to substantiate these arguments.



## Reference

- ABRAHAM, G. 1988 Turbulence and mixing in stratified tidal flows. In: *Physical Processes in Estuaries*, J. Dronkers & W. van Leussen (ed.), Springer-Verlag., pp. 150-180.
- ABRAHAM G. & R. SPANHOFF 1988 Middellang Termijn Plan Inhomogene Stromingen. DELFT HYDRAULICS, report Z162-10, Febr. (in Dutch).
- ANDREWS, D.G. & McINTYRE, M.E. 1978 An exact theory of nonlinear waves on a Lagrangian-mean flow. *J. Fluid Mech.*, 89, 609-646.
- BAKHMETEV, B.A. 1932 *Hydraulics of open channels*. Eng. Soc. Monograph McGraw- Hill.
- BATCHELOR, G.K. 1953 *The theory of homogeneous turbulence*. Cambridge University Press.
- BATCHELOR, G.K. & J.M. NITSCHKE 1991 Instability of stationary unbounded stratified fluid. *J. Fluid Mech.*, vol. 227, pp. 357-391.
- BENDAT, J.S. & A.G. PERSOL 1971 *Random data: analysis and measurement procedures*, Wiley-Interscience, New York.
- BENDER, C.M. & S.A. ORSZAG 1978 *Advanced mathematical methods for scientists and engineers*, McGraw-Hill Book Company.
- BREEDING, R.J. 1971 A non-linear investigation of critical levels for internal atmospheric gravity waves. *J. Fluid Mech.*, vol. 50, part 3, pp. 545-563.
- BRETHERTON, F.P. & GARRETT, C.J.R. 1968 Wavetrains in inhomogeneous moving media. *Proc. Roy. Soc. A.*, Vol. 302, 529-554.
- BOLGIANO, R. Jr. 1959 Turbulent spectra in a stably stratified atmosphere. *J. of Geoph. Res.*, Vol. 64, No. 12, pp. 2226-2229.
- BOOGAARD, V.D., H. 1994 Notes on the random telegraph signal, its probability distribution and spectrum. DELFT HYDRAULICS.
- BOOKER, J.R. & BRETHERTON, F.P. 1967 The critical layer for internal gravity waves in a shear flow. *J. Fluid Mech.*, Vol. 27, part 3, pp. 513-539.
- CALDWELL, D.R., S.D. WILCOX & M. MATSLER 1975 A relatively simple freely-falling probe for small-scale temperature gradients. *Limnol. Oceanogr.*, vol. 20, pp. 1035-1047.
- CAMBON, C. 1989 An EDQNM treatment of axisymmetric turbulence in a stratified fluid. *Ecole Centrale de Lyon, C.N.R.S. No. 263*, 1-23.
- CARRUTHERS, D.J. & J.C.R. HUNT 1986 Velocity fluctuations near an interface between a turbulent region and a stably stratified layer. *J. Fluid Mech.*, Vol. 165, pp. 475-501.
- CHOU, P.Y. 1945 On velocity correlations and the solution of the equations of turbulent fluctuation. *Quart. J. Appl. Math.*, 3, 1, pp. 38-54.
- COLBOURNE, E.B. 1987 An acoustic remote sensing study of an arctic submarine spring plume. M.Sc. Thesis, Mem. Univ. Newfoundland, Oct.
- CORSSIN, S. 1959 Progress report on some turbulent diffusion research. *Proceedings of Symposium on Atmospheric Diffusion and Air Pollution*, Oxford, 1958, Academic Press, Vol. 6, 161-164.
- CRAYA, A. 1958 Contribution à l'analyse de la turbulence associée à des vitesses moyennes. *Publications scientifiques et techniques du Ministère de l'air*, No. 345, Paris.

- DAVIES, A.M & H. GERRITSEN 1994 An intercomparison of three-dimensional tidal hydrodynamical modes of the Irish Sea. *Tellus*, vol. 46A, no. 2, pp. 200-221
- CWR 1993 MicroProfiler Instrument and analysis software. Centre for Water Research, Un. Western Australia, revision 3, March 10.
- DICKEY, T.D. & G.L. MELLOR 1980 Decaying turbulence in neutral and stratified fluids. *J. Fluid Mech.*, vol. 99, part 1, pp. 13-31.
- DILLON, T.M. & D.R. CALDWELL 1980 The Batchelor spectrum and dissipation in the upper ocean. *J. Geophys. Res.*, vol. 85, pp. 1910-1916.
- DILLON, T.M. 1982 Vertical overturns: a comparison of Thorpe and Ozmidov length scales. *J. Geophys. Res.*, vol. 87, no. C12, pp. 9601-9613.
- DRAZIN, P.G. & W.H. REID 1981 *Hydrodynamic stability*. Cambridge University Press.
- ELIASSEN, A. & E. PALM 1961 On the transfer of energy in stationary mountain waves. *Geofys. Publ. Oslo*, vol. 22, part 3, pp. 1-23.
- FINNIGAN, J.J. & EINAUDI, F. 1981 The interaction between an internal gravity wave and the planetary boundary layer. Part II: Effect of the wave on the turbulence structure. *Quart. J.R. Met. Soc.*, Vol. 107, pp. 807- 832.
- FINNIGAN, J.J. 1987 Kinetic energy between internal gravity waves and turbulence. *J. of the Atm. Sci.*, Vol 45, No. 3, pp. 486-505.
- FINNIGAN, J.J., F. EINAUDI, & D. FUA 1984 The interaction between an internal gravity wave and turbulence in the stably-stratified nocturnal boundary layer. *J. of the Atm. Sci.*, Vol. 41, No. 16, pp. 2409-2436.
- FISZ, M. 1963 *Probability theory and mathematical statistics*. J. Wiley & Sons, N.Y.-London. pp. 105-124.
- FRITTS, D.C. 1976 Viscous stabilization of gravity wave critical level flows. *J. Atmos. Sci.*, vol. 33, pp. 2276-2284.
- FRITTS, D.C. 1982a The transient critical level interaction in a Boussinesq fluid. *J. Geophys. res.*, vol. 87, no. C10, pp. 7997-8016.
- FRITTS, D.C. 1982b Shear excitation of atmospheric gravity waves. *J. Atmos. Sci.* vol 39, pp. 1936-1952
- GARGETT, A.E., T.R. OSBORN & P.W. NASMYTH 1984 Local isotropy and the decay of turbulence in a stratified fluid. *J. Fluid Mech.*, Vol. 144, 231-280.
- GARGETT, A.E., P.J. HENDRICKS, T.B. SANFORD & A.J. WILLIAMS III 1981 A composite spectrum of vertical shear in the upper ocean. *J. Phys. Ocean.*, vol. 11, pp. 1258-1271.
- GARRETT, C.J.R. 1968 On the interaction between internal gravity waves and a shear flow. *J. Fluid Mech.*, Vol. 34, part 4, pp. 711-720.
- GEYER, W.R. & J.D. SMITH 1987 Shear instability in a highly stratified estuary. *J. Phys. Ocean.*, Vol. 17, pp. 1669-1679.
- GERZ, T., SCHUMANN, U. & S.E. ELGHOBASHI 1989 Direct numerical simulation of stratified homogeneous turbulent shear flows. *J. Fluid Mech.*, Vol. 200, pp. 563-594.
- GIBSON, C. & W.H. SCHWARZ 1963 The universal equilibrium spectra of turbulent velocity and scalar fields. *J. Fluid Mech.*, vol. 16, pp. 365-384.
- GIBSON, C.H. 1981 Fossil turbulence and internal waves. In: *Proc. AIP Conference*, B.J. West (ed.), Am. Inst. of Physics, N.Y., No. 76, pp. 159-179.



- GIBSON, C.H. 1986 Internal waves, fossil turbulence, and composite ocean microstructure spectra. *J. Fluid Mech.*, Vol. 168, pp. 89-117.
- GILL, A.E. 1982 Atmospheric-Ocean dynamics. International geophysics series, vol. 30, Academic Press, New York.
- GREGG, M.C. 1977 Variations in the intensity of small scale mixing in the main thermocline. *J. Phys. Ocean.*, vol. 1, pp. 436-454.
- GRIMSHAW, R. 1972 Nonlinear internal gravity waves in a slowly varying medium. *J. Fluid Mech.*, Vol. 54, part 2, pp. 193-207.
- GRIMSHAW, R. 1984 Wave action and wave-mean flow interaction, with application to stratified shear flows. *Ann. Rev. Fluid Mech.*, Vol. 16, pp. 11-44.
- GRIMSHAW, R. 1984 Evolution equations for long non-linear internal waves in stratified shear flows. *Studies in Applied Mathematics*, Vol. 65, pp. 159-188.
- GRIMSHAW, R. 1988 Resonant wave interactions in a stratified shear flow. *J. Fluid Mech.*, Vol. 190, pp. 357-374.
- HASSELMANN, K. 1968 Weak-interaction theory of ocean waves. *Basic Developments in Fluid Dyn.*, Vol. 2, pp. 117-182.
- HAZEL, P. 1967 The effect of viscosity and heat conduction on internal gravity waves at a critical level. *J. Fluid Mech.*, vol. 30, part 4, pp. 775-783.
- HAZEL, Ph. 1972 Numerical studies of the stability of inviscid stratified shear flows. *J. Fluid Mech.*, Vol. 51, part 1, pp. 39-61.
- HENYEY, F.S. & N. POMPHREY 1983 Eikonal description of internal wave interactions: A non-diffusive picture of "induced diffusion". *Dyn. of Atmospheres and Oceans*, Vol. 7, pp. 189-219.
- HERRING, J.R. & O. METAIS 1989 Numerical experiments in forced stably stratified turbulence. *J. Fluid Mech.*, Vol. 202, pp. 97-115.
- HINZE, J.O. 1975 *Turbulence*. McGraw-Hill Classic Textbook Reissue Series.
- HOLLOWAY, G. 1980 Oceanic waves are not weak waves. *J. Phys. Ocean.*, vol. 10, pp. 906-914.
- HOLT, S.E., J.R. KOSEFF & J.H. FERZIGER 1992 A numerical study of the evolution and structure of homogeneous stably stratified sheared turbulence. *J. Fluid Mech.*, vol. 237, pp. 499-539.
- HOWARD, L.N. 1961 Note on a paper of John W. Miles. *J. Fluid Mech.*, vol. 10, pp. 509-512.
- HUNT, J.C.R. J.C. KAIMAL & J.E. GAYNOR 1985 Some observations of turbulence structure in stable layers. *Quart. J. R. Met. Soc.*, vol. 111, pp. 793-815.
- IMBERGER, J. & B. BOASHASH 1986 Application of the Wigner-Ville distribution to temperature gradient microstructure: A new technique to study small-scale variations. *J. Phys. Oceanogr.*, 16, pp. 1997-2012.
- IMBERGER, J. & G. IVEY 1991 On the nature of turbulence in a stratified fluid. Part II: application to lakes. *J. Phys. Oceanogr.*, vol. 21, no. 5, May, pp. 659-680.
- IMBERGER, J. 1994 Summary of the discussion on small-scale processes in stratified flows. Meeting held at Un. Arizona, Tempe, Aug. 4, J. Fernando (org.).
- ITSWEIRE, E.C. 1984 Measurements of vertical overturns in a stably stratified turbulent flow. *Phys. Fluids*, Vol. 27, No. 4, 764-766.

- ITSWEIRE, E.C., K.N. HELLAND & C.W. VAN ATTA 1986 The evolution of grid-generated turbulence in a stably stratified fluid. *J. Fluid Mech.*, vol. 162, pp. 299-338.
- IVEY, G. & J. IMBERGER 1991 On the nature of turbulence in a stratified fluid. Part I: the energetics of mixing. *J. Phys. Oceanogr.*, vol. 21, no. 5, May, pp. 650-658.
- JACOBSEN, J.P. 1913 Remarks on the determination of the movement of the water and the intermixing of the watersheets in a vertical direction. *Rapports et procès-verbaux des réunions du Conseil Permanent International pour l'Exploration de la Mer*, pp. 61-68.
- KAIMAL, J.C., J.C. WYNGAARD, Y. IZUMI, Y. & R.O. COTE 1972 Spectral characteristics of surface-layer turbulence. *Quart. J. R. Met. Soc.*, Vol. 98, pp. 563-589.
- KAIMAL, J.C., 1973 Turbulence spectra, length scales and structure parameters in the stable surface layer. *Bound. Layer Met.*, Vol. 4, pp. 289-309.
- KAIMAL, J.C. & GAYNOR, J.E. 1985 Some observations of turbulence structure in stable layers. *Quart. J.R. Met. Soc.*, Vol. 111, pp. 793-815.
- KAMPÉ DE FÉRIET, J. 1948 Le tenseur spectral de la turbulence homogène non isotrope dans un fluide incompressible. *Comptes Rendus*, t. 227, pp. 760-761.
- KARELSE, M. 1974 Vertical exchange coefficients in stratified flows. Data and empirical correlations. In: *Momentum and mass transfer in stratified flows, report on literature study. DELFT HYDRAULICS, report R-880, December.*
- KERNKAMP, H.W.J. & Th. VAN DER KAAIJ 1993 Opzet en afregelen TRISULA model RIJMOMA. Report Z-590, DELFT HYDRAULICS, May (in Dutch).
- KOLMOGOROFF, A.N. 1941 Dissipation of energy in the locally isotropic turbulence. *Comptes Rendus (Doklady) de l'Académie des Sciences de l'URSS*, Vol. 32, No. 1, pp. 16-18.
- KOLMOGOROFF, A.N. 1941 The local structure of turbulence in incompressible viscous fluid for very large Reynolds' number, *Comptes Rendus (Doklady) de l'Académie des Sciences de l'URSS*, Vol. 30, No. 4, pp. 301-305.
- KOMORI, S., H. UEDA, F. OGINO, F. & T. Mizushima 1983 Turbulence structure in stably stratified open-channel flow. *J. Fluid Mech.*, Vol. 130, pp. 13-26.
- KONDO, J., O. KANECHIKA & N. YASUDA 1978 Heat and momentum transfers under strong stability in the atmospheric surface layer. *J. of the Atm. Sci.*, Vol. 35, pp. 1012-1021.
- KOOP, C.G. 1981 A preliminary investigation of the interaction of internal gravity waves with a steady shearing motion. *J. Fluid Mech.*, Vol. 113, pp. 347-386.
- KOOP, C.G. & B. McGEE 1986 Measurements of internal gravity waves in a continuously stratified shear flow. *J. Fluid Mech.*, Vol. 172, pp. 453-480.
- KRAICHNAN, R.H. 1959 The structure of isotropic turbulence at very high Reynolds numbers. *J. Fluid Mech.*, Vol. 5, pp. 497-543.
- KRANENBURG, C., J.D. PIETRZAK & G. ABRAHAM 1991 Trapped internal waves over undular topography. *J. Fluid Mech.*, 226, pp. 205-217.
- LALAS, D.P. & F. EINAUDI 1976 On the characteristics of gravity waves generated by atmospheric shear layers. *J. of the Atm. Sc.*, Vol. 33, pp. 1248-1259.



- LALAS, D.P. & F. EINAUDI 1980 Tropospheric gravity waves: their detection by and influence on rawinsonde balloon data. *Quart. J. R. Met. Soc.*, Vol. 106, pp. 855-864.
- LANGE, R.E. 1982 An experimental study of turbulence behind towed biplanar grids in a salt-stratified fluid. *J. of Phys. Ocean.*, Vol. 12, pp. 1506-1513.
- LAUNDER, B.E. & D.B. SPALDING 1974 The numerical computation of turbulent flows. *Comp. Met. in Appl. Mech. and Eng.*, 3, p 269.
- LAUNDER, B.E., G.J. REESE & W. RODI 1975 Progress in the development of a Reynolds-stress turbulence closure. *J. Fluid Mech.*, Vol. 68, Part 3, pp. 537-566.
- LAUNDER, B.E. 1984 Second moment closure methodology and practice. In "Turbulence models and their applications", Vol. 2, Editions Eyrolles, Paris, pp. 1-147.
- LeLONG, M.P., J.J. RILEY & C. STAQUET 1987 A study of wave-vortex interactions in density-stratified fluids. In: 3rd Int. Symp. of Stratified Flows, Pasadena, Vol. 2, pp. 1-10.
- LESIEUR, M., O. METAIS & R. ROGALLO 1989 Etude de la diffusion turbulente par simulation des grandes échelles. *C.R. Acad. Sci. Paris*, Vol. 308, Serie II, pp.1395-1400.
- LIENHARD, J.H. & C.W. ATTA, Van 1990 The decay of turbulence in thermally stratified flow. *J. Fluid Mech.*, Vol. 210, pp. 57-112.
- LIGHTHILL, M.J. 1962 Physical interpretation of the mathematical theory of wave generation by wind., *J. Fluid Mech.*, vol. 14, pp. 385-398.
- LIGHTHILL, M.J. 1965 Group velocity. *J. Inst. Math. Appl.*, vol. 1, pp. 1-28.
- LINDEN, P.F. 1979 Mixing in stratified fluids. *Geophys. Astrophys. Fluid. Dyn.*, Vol. 13, 3-23.
- LUMLEY, J.L. 1964 The spectrum of nearly inertial turbulence in a stably stratified fluid. *J. of the Atm. Sci.*, Vol. 21, 99-102.
- MALATT, K. 1992 Rotterdam data report; experiment 92152. Centre for Water Research, Perth, W. Australia, July.
- MALVERN, L.E. 1969 Introduction to the mechanics of a continuous medium. Prentice- Hall Series.
- MCCOMAS, C.H. & F.P. BRETHERTON 1977 Resonant interaction of oceanic internal waves. *J. of Geophys. Research*, Vol. 82, No. 9, 1397-1412.
- MÜLLER, P. 1976 On the diffusion of momentum and mass by internal gravity waves. *J. Fluid Mech.*, Vol. 77, Part 4, pp. 789-823.
- MÜLLER, P. & D.J. OLBERS 1975 On the dynamics of internal waves in the deep ocean. *J. Geophys. Res.*, vol. 80, no. 27, Sept., pp. 3848-3860.
- METAIS, O. & J.R. HERRING 1989 Numerical simulations of freely evolving turbulence in stably stratified fluids. *J. Fluid Mech.*, Vol. 202, pp. 117-148.
- MOBBS, S.D. & J.M. REES 1989 Cross-spectral properties of large eddies in the stably stratified atmospheric boundary layer. In: *Proc. Advances in Turbulence 2*, Springer-Verlag Berlin, Heidelberg, pp. 180-1185.
- MONIN, A.S. & A.M. OBUKHOV 1953 Dimensionless characteristics of turbulence in the surface layer of the atmosphere. *Poc. (Dokl.) Acad. Sci. USSR*, vol. 93, no. 2.
- MONIN, A.S. & R.V. OZMIDOV 1985 Turbulence in the ocean. D. Reidel Publ. Comp., The Netherlands.
- NEW, A.L. & K.R. DYER 1988 Predictions of the generation and propagation of internal waves and mixing in a partially stratified estuary. In: *Proc. Estuarine Coastal & Shelf Science*. pp. 1-36.

- NEZU, I. & W. RODI 1986 Open-channel flow measurements with a Laser Doppler Anemometer. *J. Hydr. Eng.*, Vol. 112, no. 5, May, pp. 335-355.
- ORLANSKI, I. 1972 On the breaking of standing internal gravity waves. *J. Fluid Mech.*, Vol. 54, Part 4, pp. 577-598.
- OBUKHOV, A.M. 1959 On the influence of the buoyancy force on the structure of the temperature field in a turbulent flow. *Proc. (Dokl.) Acad. Sci. USSR*, vol. 125, no. 6.
- OZMIDOV, R.V. 1965 On the turbulence exchange in a stably stratified ocean. *Izv., Atmospheric and ocean Physics Series*, vol. 1, no. 8, pp. 853-860.
- PALMER T.N., G.J. SHUTTS & R. SWINBANK 1986 Alleviation of a systematic westerly bias in general circulation and numerical weather prediction models through an orographic gravity wave drag parametrization. *Quart. J.R. Met. Soc.*, vol. 112, pp. 1001-1039.
- PAO, Y. 1973 Measurements of internal waves and turbulence in two-dimensional stratified shear flows. *Boundary-Layer Meteorology*, Vol. 5, pp. 177-193.
- PAPOULIS, A. 1965 Probability, random variables and stochastic processes. McGraw-Hill Kogakusha Ltd.
- PEDLOSKY, J. 1979 Geophysical fluid dynamics. Springer-Verlag, New York.
- PHILLIPS, O.M. 1980 The dynamics of the upper ocean. paperback ed., Cambridge Un. Press.
- PIETRZAK, J.D., G. ABRAHAM & C. KRANENBURG 1989 Field observations of internal waves in the Rotterdam Waterway. *Stratified Flows Rep. 6*. Rijkswaterstaat, DELT HYDRAULICS, Delft University of Technology.
- PRANDTL, L. 1925 Über die ausgebildete Turbulenz. *ZAMM*, Vol. 5, p. 136
- REYNOLDS, O. 1894 On the dynamical theory of incompressible viscous fluids and the determination of the criterion. *Roy. Soc. of London*, Vol. 186, pp. 123-163.
- RICHARDSON, L.F. 1920 The supply of energy from and to atmospheric eddies. *Proc. R. Soc. Lond.*, A97, pp. 345-373.
- RILEY, J.J. R.W. METCALFE & M.A. WEISSMAN 1981 Direct numerical simulations of homogeneous turbulence in density-stratified fluids. In: *Proc. AIP Conference No. 76*, Am. Inst. of Physics, N.Y., pp. 79-112.
- RIPA, P. 1981 On the theory of nonlinear wave-wave interactions among geophysical waves. *J. Fluid Mech.*, Vol. 103, pp. 87-115.
- RODI, W. 1984 Turbulence models and their application in hydraulics. IAHR publ., Delft.
- RODI, W. & N.N. MANSOUR 1993 Low Reynolds  $k-\epsilon$  modelling with the aid of direct numerical simulation data. *J. Fluid Mech.*, vol. 250, pp. 509-529.
- ROHR, J.J., HELLAND, K.N., ITSWEIRE, E.C. & ATTA, C.W. van 1985 Turbulence in a stably stratified shear flow: A progress report. In: *Proc. 5th Symp. on Turbulent Shear Flows*. Cornell Univ., Ithaco, N.Y. 22.1 - 22.6.
- ROHR, J.J., E.C. ITSWEIRE & C.W. ATTA van 1984 Mixing efficiency in stably stratified decaying turbulence. *Geophys. Astrophys. Fluid Dyn.*, Vol. 29, pp. 221-236.
- SCHUMANN, U. 1987 The countergradient heat flux in turbulent stratified flows. *Nuclear Eng. and Design*, Vol. 100, pp. 255-262.
- SIMONIN, O., R.E. UITTENBOGAARD, F. BARON & P.L. VIOLLET 1989 Possibilities and limitations to simulate turbulence fluxes of mass and momentum, measured in a steady stratified mixing layer. In *Proc.*



- XXIII IAHR Congress, Ottawa, August 21-25, published by National Research Council Canada, A55-A62.
- STAQUET, Ch. & Ch. STAQUET & J.J. RILEY 1987 A numerical study of a stably-stratified mixing layer. In: Proc. 6th T.S.F., Toulouse, 20-3-1 - 20-3-6.
- STEWART, R.W. 1969 Turbulence and waves in a stratified atmosphere. *Radio Sci.*, Vol. 4, No. 12, pp. 1269-1278.
- STILLINGER, D.C., M.J. HEAD, K.N. HELLAND & C.W. VAN ATTA 1983 A closed-loop gravity-driven water channel for density-stratified shear flows. *J. Fluid Mech.*, vol. 131, pp. 73-89.
- STILLINGER, D.C., K.N. HELLAND & C.W. VAN ATTA 1983 Experiments on the transition of homogeneous turbulence to internal waves in a stratified fluid. *J. Fluid Mech.*, vol. 131, pp. 91-122.
- TAYLOR, G.I. 1915 Eddy motion in the atmosphere. *Phil. Trans. A*, **215**, 1-26. Also *Scientific Papers*, **2**, pp. 1-23, Cambridge University Press.
- TAYLOR, G.I. 1921 Diffusion by continuous movements. *Proc. London Math. Soc.*, ser. 2, vol. XX, pp. 196-212, reprinted in *The scientific papers of Sir Geoffrey Ingram Taylor*, Vol. II Meteorology, oceanography and turbulent flows, G.K. Batchelor (ed.), Cambridge University Press, 1960.
- TAYLOR, G.I. 1931 Effect of variation in density on the stability of superposed streams of fluid. *Proc. Camb. Phil. Soc.*, **23**, pp. 730-731; *Scientific Papers*, **2**, pp. 219-239.
- TAYLOR, G.I. 1954 The dispersion of matter in turbulent flow through a pipe. *Proc. Roy. Soc. London, Ser. A. Math. and Phys. Sci.*, Vol. A223, pp. 446-468.
- TENNEKES, H. & J. LUMLEY 1972 A first course in turbulence. MIT Press.
- THORPE, S.A. 1973 Turbulence in stably stratified fluids: A review of laboratory experiments. *Boundary Layer Meteorology*, Vol. 5, pp. 95-119.
- THORPE, S.A. 1981 An experimental study of critical layers. *J. Fluid Mech.*, Vol. 103, 321-344.
- THORPE, S.A. & J.M.I. BRUHAKER 1983 *Land and Ocean*, 28(1), pp. 601-613.
- TOLSTOY, I. 1973 Wave propagation. McGraw-Hill.
- TOWNSEND, A.A. 1965 Excitation of internal waves by a turbulent boundary layer. *J. Fluid Mech.*, Vol. 22, Part 2, pp. 241-252.
- TOWNSEND, A.A. 1966 Internal waves produced by a convective layer. *J. Fluid Mech.*, Vol. 24, Part 2, pp. 307-319.
- TOWNSEND, A.A. 1968 Excitation of internal waves in a stably-stratified atmosphere with considerable wind-shear. *J. Fluid Mech.*, Vol. 32, Part 1, pp. 145-171.
- TURNER, J.S. 1979 Buoyancy effects in fluids. Cambridge University Press.
- UITTENBOGAARD, R.E. 1986 Turbulentie en Menging in Inhomogene Stromingen, Middellang Termijn Plan 1986-1991. DELFT HYDRAULICS, note Z78, Febr.
- UITTENBOGAARD, R.E. 1988 Measurement of turbulence fluxes in a steady stratified mixing layer. In: Proc. 3rd Int. Symp. Refined Flow Modelling and Turbulence Measurements, Tokyo, 26-28 July, paper T11-3.
- UITTENBOGAARD, R.E. & F. BARON 1989 A proposal: extension of the  $k-\epsilon$  model for stably stratified flows with transport of Internal Wave Energy. Paper 18.4 in 7th Turbulent Shear Flows Symp., Stanford, August pp. 21-23.
- UITTENBOGAARD, R.E. 1991 Theory of quadrature spectra of turbulence and internal waves. DELFT HYDRAULICS, note Z162.

- UITTENBOGAARD, R.E., J.A.Th.M. van KESTER & G.S. STELLING 1992 Implementation of an Algebraic eddy-viscosity, a k-L and the k-e turbulence model in TRISULA for rectangular horizontal grids. Including 2DV-testcases, DELFT HYDRAULICS, report Z78, May.
- UITTENBOGAARD, R.E. 1993 Measurement of turbulent kinetic energy and of internal wave energy in the Rotterdam Waterway Estuary. DELFT HYDRAULICS, report Z-162, July.
- WEINSTOCK, J. 1978 On the theory of turbulence in the buoyancy subrange of stably stratified flows. *J. of Atm. Sc.*, Vol. 35, 634-649.
- YOON, K. & Z. WARHARFT 1990 The evolution of grid-generated turbulence under conditions of stable thermal stratification. *J. Fluid Mech.*, vol. 215, pp. 601-638.
- WEST, J.R. & K. SHIONO 1988 The structure of turbulence in partially mixed estuaries. In: *Physical Processes in Estuaries*, J. Dronkers & W. van Leussen (ed.), Springer-Verlag, pp. 196-210.
- ZIC, K. & J. IMBERGER 1994 Energy leakage from a surface mixing layer. Submitted to *J. Geophys. Res.*





## Appendix A

### Some details concerning limits of energy spectra

#### A.1 Gibson's criterion for maximal $L_c$

Gibson (1981) based an estimator for the largest wave length of the part of the inertial subrange of isotropic turbulence which is practically unaffected by buoyancy on the criterion

$$\langle \tilde{Ri} \rangle = \frac{N^2}{\left\langle \left( \frac{\partial \tilde{u}}{\partial z} \right)^2 \right\rangle} \leq 1/4 . \quad (A.1.1)$$

He estimated the variance  $\langle (\partial \tilde{u} / \partial z)^2 \rangle$  of the transverse shear from a given rate of viscous energy dissipation  $\epsilon$  in isotropic turbulence:

$$\epsilon = \nu \langle \tilde{\gamma}^2 \rangle ; \quad \langle \tilde{\gamma}^2 \rangle = \frac{15}{2} \left\langle \left( \frac{\partial \tilde{u}}{\partial z} \right)^2 \right\rangle . \quad (A.1.2)$$

To satisfy (A.1.1) the total variance of turbulence strain rate  $\langle \tilde{\gamma}^2 \rangle$ , defined in (A.1.2), requires the lower limit:

$$\langle \tilde{\gamma}^2 \rangle \geq 30 N^2 . \quad (A.1.3)$$

Hence, the minimal value for the small-scale Froude number, defined by (Imberger and Boashash, 1986), reads:

$$Fr_\gamma = \frac{|\tilde{\gamma}|}{N} \geq 5.5 . \quad (A.1.4)$$

In addition, substitution of (A.1.2) into (A.1.1) yields

$$\langle \tilde{Ri} \rangle = \frac{15}{2} \frac{\nu N^2}{\epsilon} = \frac{15}{2} \left( \frac{L_K}{L_R} \right)^{4/3} \leq 1/4 ; \quad L_R \geq 30^{3/4} L_K . \quad (A.1.5)$$

From the arguments of Ozmidov and of Abraham (Section 3.3) follow that the largest length scale of isotropic turbulence in the inertial subrange is related to  $L_R$ , say  $C_1 L_R$

The inertial subrange of isotropic turbulence vanishes when the maximal length scale  $C_1 L_R$  approaches the smallest wavelength of turbulence which Gibson estimates as  $15 L_K$ . Hence, from (A.1.5) follows:

$$15 L_K < \lambda < C_1 L_R ; \quad C_1 = \frac{15}{30^{3/4}} \approx 1.2 . \quad (A.1.6)$$

The definition of  $\langle \tilde{Ri} \rangle$  and its upper limit of  $1/4$  for isotropic turbulence deserve the following comments. Firstly, Abarbanel (1983) found the critical Ri-number for nonlinear waves to be unity and thus  $1/4$  is a safe lower limit for the present purpose. Secondly, if  $1/4$  in (A.1.1) was meant as the linear upper limit of the Kelvin- Helmholtz instability then

$$\langle \tilde{Ri} \rangle = \frac{N^2}{\left\langle \left( \frac{\partial \tilde{u}}{\partial z} \right)^2 \right\rangle + \left\langle \left( \frac{\partial \tilde{v}}{\partial z} \right)^2 \right\rangle}$$



would have been preferable to our opinion. Accordingly, the lower limit in (A.1.3) is reduced to  $\langle \tilde{\gamma}^2 \rangle \geq 15 N^2$  while  $C_1 = 15^{1/4} \approx 2.0$ .

We conclude, not entirely unexpected, that there is some tolerance in the lower limit for  $Fr_\gamma$  and of  $C_1$ . However, their order of magnitude and sometimes even better than that have been confirmed by experiments summarized in (Ivey and Imberger, 1990) and (Abraham, 1986).

Hence, the equivalent Richardson number criterion (A.1.1) or

$$\langle \tilde{R} \rangle = \frac{N^2}{\left\langle \left( \frac{\partial \tilde{u}}{\partial z} \right)^2 \right\rangle + \left\langle \left( \frac{\partial \tilde{v}}{\partial z} \right)^2 \right\rangle} \leq 1/4$$

correspond with experimental observations of grid-generated stratified turbulence.

## A.2 Gibson's criterion for saturated IWE spectrum

In view of Section A.1 we will investigate whether Gibson's upper limit of 3D saturated internal waves provides an equivalent Richardson number similar to (A.1.1) that has  $1/4$  as *lower* limit. Actually, we will show by his own arguments and his procedure that there is an inconsistency in his derivation of the upper limit of (saturated) internal wave spectra. The inconsistency is that the minimal Richardson number related to saturated wave spectra lies well below the maximal Richardson number of inertia dominated turbulence. Hence, we conclude Gibson overestimates the energy of saturated waves by at least one order of magnitude.

Gibson (1986) proposed the observed transverse shear spectrum of internal waves in the ocean:

$$\tilde{\Phi}_{\partial u / \partial z} = Gi N^2 m^{-1}, \quad (A.2.1)$$

with constant  $Gi$ . He estimates  $Gi=6.7$  (Gibson, 1986, eq. 5) which appears to be much larger than our estimate based on (2.6.9). Below we will follow Gibson's derivation which is based in matching the shear rate spectrum of internal waves to the shear rate spectrum of turbulence.

As a consequence of (A.2.1) the variance of transverse strain rate reads:

$$\left\langle \left( \frac{\partial \tilde{u}}{\partial z} \right)^2 \right\rangle = \int_M^{m_+} \tilde{\Phi}_{\partial u / \partial z}(\mu) d\mu = Gi N^2 \ln(b_z). \quad (A.2.2)$$

In (A.2.2) we integrate between the minimal vertical wavenumber  $M$  and maximal vertical wavenumber  $m_+$  and their ratio is the bandwidth  $b_z$ . Gibson defines the maximal value for  $Gi$  in (A.2.1) to represent a saturated 3D internal wave (shear) spectrum if  $\tilde{\Phi}_{\partial u / \partial z}$  matches the turbulence shear spectrum  $\tilde{\Phi}_{\partial u / \partial z}^*$  at wavelength  $\lambda_+$  in the inertial subrange of isotropic turbulence. For the inertial subrange of isotropic turbulence holds (Hinze, 1975, p. 205) the

Kolmogorov spectrum:

$$\hat{E}(|\mathbf{k}|) = A \epsilon^{2/3} |\mathbf{k}|^{-5/3}, \quad (\text{A.2.3})$$

with wavenumber magnitude  $|\mathbf{k}|$  and  $A \approx 1.7$ .

The turbulent kinetic energy associated with the inertial subrange follows from the integral of (A.2.3) over the inertial subrange of wavenumbers:

$$\frac{3}{2} \langle \hat{u}^2 \rangle_{\text{sub}} = \int_{\text{sub}} \hat{E}(|\mathbf{k}|) d|\mathbf{k}|. \quad (\text{A.2.4})$$

According to Hinze (1975, p. 209) the power spectrum  $\hat{E}_u(\mathbf{m})$  of the horizontal turbulent velocity component  $\hat{u}$  as a function of the vertical wavenumber  $\mathbf{m}$  follows from:

$$\hat{E}_u(\mathbf{m}) = \frac{1}{2} \int_{\text{sub}} \hat{E}(|\mathbf{k}|) \left[ 1 - \left( \frac{\mathbf{m}}{|\mathbf{k}|} \right)^2 \right] d|\mathbf{k}| = \frac{24}{55} A \epsilon^{2/3} \mathbf{m}^{-5/3}.$$

and thus the turbulence shear spectrum  $\hat{\Phi}_{\partial u / \partial z}$  in the inertial subrange reads

$$\hat{\Phi}_{\partial u / \partial z} = \mathbf{m}^2 \hat{E}(\mathbf{m}) = \frac{24}{55} A \epsilon^{2/3} \mathbf{m}^{1/3}. \quad (\text{A.2.5})$$

For saturated internal wave spectra Gibson (1986) matches (A.2.1) to (A.2.5) at the transitional vertical wavelength  $\lambda = \lambda_+$  between buoyancy subrange and inertial subrange. Consequently, the maximal value  $G_{i_{\text{sat}}}$  of the unknown constant  $G_i$  in (A.2.1) reads:

$$G_{i_{\text{sat}}} = \frac{24}{55} A \left( \frac{2\pi L_R}{\lambda_+} \right)^{4/3}; \quad G_{i_{\text{sat}}} \approx 6.7 \text{ for } \lambda_+ = 1.2 L_R \text{ and } A = 1.7. \quad (\text{A.2.6})$$

Substitution of (A.2.6) into (A.2.2) yields for the equivalent Richardson number (A.1.1) now related to wave-induced shear:

$$\langle \tilde{R}_{i_{\text{sat}}} \rangle = \frac{N^2}{\left\langle \left( \frac{\partial \hat{u}}{\partial z} \right)^2 \right\rangle} \geq \frac{0.14}{\ln(b_z)}, \quad (\text{A.2.7})$$

for  $G_i \leq G_{i_{\text{sat}}}$  and  $0.14 \approx 1/G_{i_{\text{sat}}}$ .

The lower limit of  $\langle \tilde{R}_{i_{\text{sat}}} \rangle$  according to (A.2.7) is smaller than the upper limit of  $\langle \tilde{R}_i \rangle$  used by Gibson (Section A.1) to estimate the bandwidth of the inertial subrange of isotropic turbulence. Hence, the lower limit (A.2.7) is underestimated by at least the factor  $\{G_{i_{\text{sat}}} \ln(b_z)\}$  apart from the discussion of the definition of  $\langle \tilde{R}_i \rangle$  at the end of Section B.1. Hence, to our opinion there is an inconsistency in Gibson's derivation for the upper limit of internal wave spectra.

One possible inconsistency may be that in (A.1.6) and consequently in (A.2.6) the typical wave length instead of typical length scale is used. This ambiguity is discussed in Section 3.4. There we concluded that for the present case we must put  $\mathbf{m}_+ = (C_1 L_R)^{-1}$ . This reduces  $G_{i_{\text{sat}}}$  significantly by a factor 11.58 to  $G_{i_{\text{sat}}} = 0.58$ . Before the lower limit in (A.2.7) reaches  $1/4$  the bandwidth  $b_z$  must exceed  $O(1000)$ . Consequently, the inconsistency is removed: the Richardson number for internal waves remains beyond  $1/4$  for an internal wave bandwidth not exceeding 3 decades.





**main office**  
Rotterdamseweg 185  
p.o. box 177  
2600 MH Delft  
The Netherlands  
telephone (31) 15 - 56 93 53  
telefax (31) 15 - 61 96 74  
telex 38176 hydel-nl

**location 'De Voorst'**  
Voorsterweg 28, Marknesse  
p.o. box 152  
8300 AD Emmeloord  
The Netherlands  
telephone (31) 5274 - 29 22  
telefax (31) 5274 - 35 73  
telex 42290 hylvo-nl

